Theoretical and Experimental Study into the Dynamics and Control of a Flexible Beam with a DC-Servo Motor Actuator

by

John M. Juston

Thesis submitted to the Faculty of the Virginia Polytechnic Institute and State University in partial fulfillment of the requirements for the Degree of

Master of Science

in

Mechanical Engineering

Approved:

Dr. H. H. Robertshaw

Dr. S. Hendricks

Dr. A. Myklebust

October, 1985

Blacksburg, Virginia

ACKNOWLEDGEMENTS

I would like to use this first bit of space to thank all the people that helped make things happen while this research was being conducted. Thanks go out to and the computer people, to and Mr. Sittler the department people, to the typing person and to all the machine shop and instrumentation room people. I see no way this could have happened without your help.

Thanks also go to Dr. Hendricks for serving on my committee and to Dr. Myklebust for serving on my committee and also for the motor and amplifier. Time constraints prevented Dr. J. L. Junkins from serving as a committee memeber, but it is very appropriate to thank him for his helpful tutorial sessions while I was sub-optimally iterating on the depths of some of his work.

I would like to use this last bit of space for those special thanks. Thank you for everything from the opportunity, to the support, to a great friendship. Thank you to all my friends for putting up with me while I worked on this. Thank you Mom and Dad for being so understanding and supportive of me and my ways. And thank you for always being there.

TABLE OF CONTENTS

LIST OF FIGURES

LIST OF TABLES

List of Symbols

Symbol	
LSS	large space structure
PI	performance index
$\underline{b}$	body-fixed coordinate system on beam
$\underline{n}$	newtonian reference coordinate system
L	length of beam
EI	product of modulus of elasticity and beam inertia
m	mass per unit length of beam
t	time in seconds
x	position along beam length
$\theta(t)$	angular displacement of beam and motor
$y(x,t)$	continuous displacement field of beam
$\theta_i(x)$	chosen shape functions for beam
$q_i(t)$	shape function amplitudes
$\underline{q}$	vector of generalized coordinates of system model
V	potential energy
T	kinetic energy
F_i	force in direction of ith generalized coordinate
$\underline{R}_p$	position vector of point on beam
I	rotational inertia of beam/motor system
m_i	equivalent mass in vibration mode
a_i	beam/motor cross-coupling terms
k_i	equivalent stiffness in vibration mode
T_a	applied torque to beam

$\underline{M}$	mass matrix
$\underline{C}$	damping matrix
$\underline{K}$	stiffness matrix
$\underline{F}$	applied force matrix
R	armature resistance
L_a	armature inductance
K_b	back EMF constant
K_T	torque constant
G_A	amplifier gain
J_a	motor inertia
B_m	motor damping
F_m	average friction torque of motor
V_a	applied voltage to motor circuit
K_a	applied current to motor
$\underline{m}$	vector of measured system output variables (volts)
Thm	output voltage from potentiometer on θ
ST1	output voltage from bridge on strain gage 1
ST2	output voltage from bridge on strain gage 2
ST3	output voltage from bridge on strain gage 3
$\underline{T}$	transformation matrix between outputs and generalized coordinates
G_{sys}	overall system gain
r	position reference input
$\underline{GP}$	vector if displacement gains
$\underline{GV}$	vector of velocity gains
$\underline{\dot{m}}$	vector of velocity measurements
$\underline{\tilde{\dot{m}}}$	vector of estimated velocities

g_o	feed forward gain in rate estimators
g_z	feed back gain in rate estimators
$\underline{z}$	vector of state variables in state space notation
$\underline{A}$	matrix used in state space notation
$\underline{D}$	matrix used in state space notation
λ_i	system's ith eigenvalue
$\underline{\phi}_i$	system's left ith eigenvalue
$\underline{\psi}_i$	system's right ith eigenvector
δ_{ij}	Dirac function
$\underline{\gamma}$	vector of eigenvalue positions
$\underline{\Delta\gamma}$	vector of eigenvalue constraint residuals
ε	parameter to entrance convergence in iterations
$\underline{G}$	vector of all system gains
$\underline{\Delta G}$	vector of gain corrections
$\underline{Q}$	matrix of eigenvalue sensitivities
$\underline{W}$	weighting matrix for gain corrections
G_{th}	gain on angular position
G_{ST1}	gain on ST1
G_{ST2}	gain on ST2
G_{ST3}	gain on ST3
$G_{\dot{th}}$	gain on estimated angular velocity
$G_{\dot{ST2}}$	gain on estimated rate of ST2
$G_{\dot{ST3}}$	gain on estimated rate of ST3
G_{01}	gain in estimator for angular velocity
G_{03}	gain in estimator for rate of ST2
G_{02}	gain in estimator for rate of ST3

A_0	amplitude of oscillation
A_1	amplitude of successive oscillation
ξ	damping ratio
D_{eq}	equivalent damping
G_{pot}	gain of angular position potentiometer
J	mass moment of inertia of beam

INTRODUCTION

The ability to control flexible structures in space will be needed in the near future. This has received (1,2,3,4) and is continuing to receive much attention (5). Theory developed for large space structures (LSS) covers a diverse range (6) but it seems only recently that practical, experimentally verified work has begun (7,8,9).

This thesis is the written summary of a theoretical and experimental study into the dynamics and control of a generic flexible structure. The system studied is a flexible beam cantilevered at its base to a dc-servo motor with motion perpendicular to the gravity field. Both position and vibration control are of importance. The control algorithm is implemented on an EAI-20 analog computer.

The results of this study apply to a diversity of LSS research interests such as platform or solar panel manipulation. It could also stand as a preliminary investigation into a higher degree-of-freedom problem (10).

The nature of the problems encountered with large space structures are by now well known (6). These include:

1. distributed parameter systems
2. little or no natural damping
3. low and closely spaced natural frequencies
4. stringent position control and vibration suppression requirements.

This study is confronted with all but the problem of closely spaced natural frequencies.

Flexible beam studies have been considered before. Montgomery (7) Horner (8), and Schaechter and Eldred (11) have successfully applied a variety of control laws to flexible beam systems. However, the strength of their results is hindered by actuator and/or sensor apparatus that is external to the actual beam system. Mills (12) compares the merits of two types of tip-mounted actuators for vibration control in a rigidly supported cantilevered beam. Vibration control is achieved through direct velocity feedback, however no position control is possible with this system. Alberts and Hastings (13) apply a hybrid active and passive control scheme to a model similar to the one used in this thesis. A constrained viscoelastic layer coats the beam thus enhancing system stability by increasing system damping. Good control is then achieved via a classic linear quadratic regulator approach. As they point out though, problems are anticipated in actual space applications due to varying viscoelastic material properties.

The control approach taken here is to generate the motor's input signal based on a full output feedback law. This is an extension of experimental work done by Robertshaw (14). Robertshaw successfully implemented a partial output feedback law which demonstrated position control and vibration suppression. While the system responded swiftly and stably, complete freedom in eigenvalue placement is limited by implementing only partial output feedback (15). The author hoped to increase the system's performance by implementing a full output feedback control law allowing for complete freedom in eigenvalue placement and also optimization of a performance index (PI).

Feedback gains are selected with an algorithm presented by Junkins and Bodden (16,17). Iterations are performed on system gains to sequentially meet imposed eigenvalue constraints and then give a constrained optimized solution. Gain changes are based on eigenvalue sensitivities. To help insure convergence in the iterations, gain changes are forced to minimize a gain correction norm. In addition, constraints are met by stepping through a series of closer, intermediate constraints.

The optimality criteria treated here is minimization of a normalized eigenvalue sensitivity norm to small variations in system gains. The motivation for this is as follows. The control law is actually implemented on an analog computer. Feedback gains are set by adjusting potentiometers that are accurate to only three significant digits. In addition, it was anticipated that iterations based on a minimum gain correction norm would yield a "sensitive" set of gains. Hence, it was anticipated that best experimental results would be achieved with a minimum sensitivity gain set.

The algorithm used here has successfully treated various other performance criteria including minimum gain norm (16) and "optimized" LQR design (18). However, it is also very well suited for sensitivity minimizations. Lim and Junkins (19) have applied a related algorithm to minimize a sensitivity norm, however its applications were on a much simpler system. The novelty of the sensitivity work presented in this thesis is twofold: the sensitivity norm is normalized giving it a much stronger tie to actual system performance and it is the first such application on a complex theoretical and experimental model.

Presentation of this work begins in Chapter 2 with system modeling. Throughout this thesis, two distinct motor types are considered and compared as actuators. Hence, two system models are developed here. The first model has a voltage-controlled motor and the second model has a torque-controlled motor. The primary difference in these motors is related to back EMF. The influence of back EMF on system response is studied throughout this thesis via these two different systems. All other beam and instrumentation parameters are identical in the two models giving a good basis for comparison. The torque-controlled system models the actual experimental hardware. The voltage-controlled system does not have an actual physical counterpart here however it is the motor type used in previous experimental work (14). For clarity throughout this thesis, the voltage-controlled system is called the "example system" and the torque-controlled system is called the "experimental system."

In Chapter 3, an augmented full output-feedback control law is developed for these models. The control law and system models are included in a unified closed-loop state variable representation. In Chapter 4, an overview is presented of a gain iteration algorithm that calculates gains to meet eigenvalue constraints and minimize the PI.

In Chapter 5, open-loop characteristics are discussed for the two systems. It is shown that the different motor models change considerably. In addition, system sensitivity to motor characteristics in general, is clearly shown in a root locus plot with respect to varying motor parameters. By extending these results, the importance of good knowledge of system damping characteristics is pointed out.

In Chapter 6, model accuracy is improved by adding previously unmodeled system damping. Experimental data is considered and compared to simulated response data. An accurate system model results and is verified.

Chapter 7 presents full analytical results for the closed-loop systems. Results are presented first for the example system and then for the experimental system. Minimum gain norm and minimum sensitivity norm solutions are calculated for both systems. Simulation results, sensitivity studies and torque requirements are considered and compared for both gain solutions. All results are developed in parallel for the example and experimental systems for a good basis of comparison. Results are summarized at the end of the chapter.

In Chapter 8, experimental implementation is discussed. The intentions here were to experimentally verify the results of Chapter 7. However, unmodeled system characteristics presented unanticipated obstacles. New gain solutions that focused on these problems were calculated with the iteration algorithm. Motivations and results are fully documented with experimental data. While improvements are made, desired system response is still not achieved. Results are summarized at the end of the chapter.

Chapter 9 wraps up this thesis with a summary of conclusions. Brief recommendations for promising future research based on the results of this work are also discussed.

Chapter 2

SYSTEM MODELLING

The physical model used throughout this thesis is a flexible beam cantilevered at its base by a DC motor. Figure 2.1 shows a schematic representation of this system along with its instrumentation. The motor is equipped with a potentiometer for angular position measurement and the beam is equipped with 3 strain gages for vibration measurement.

For mathematical modelling, the beam and motor subsystems were considered separately. The resulting sets of equations were then coupled to yield the complete system model. The beam was treated as a rotating cantilever and modeled with energy methods (20). Both a voltage-controlled and torque-controlled motor are discussed throughout this thesis, so models are developed for each and combined with the beam model. Finally, the beam's instrumentation is related to the beam/motor model yielding a complete system description.

It is important to state here the features of the experimental system that are not modeled in this chapter. However, in

1. inherit damping in structure
2. 4.5 oz-in torque deadband due to Coulomb friction in motor
3. 5 kHz switching frequency of servo amplifier that drives motor.

The first unmodeled characteristic, inherent damping, is very difficult to predict mathematically. In Chapter 6, viscous damping terms are added to the model with good accuracy by consideration of experimental data. The second and third unmodeled characteristics are non-linear and must remain unmodeled. It will be seen in Chapter 9, that the torque deadband has a prominent effect on system response and presents imple-

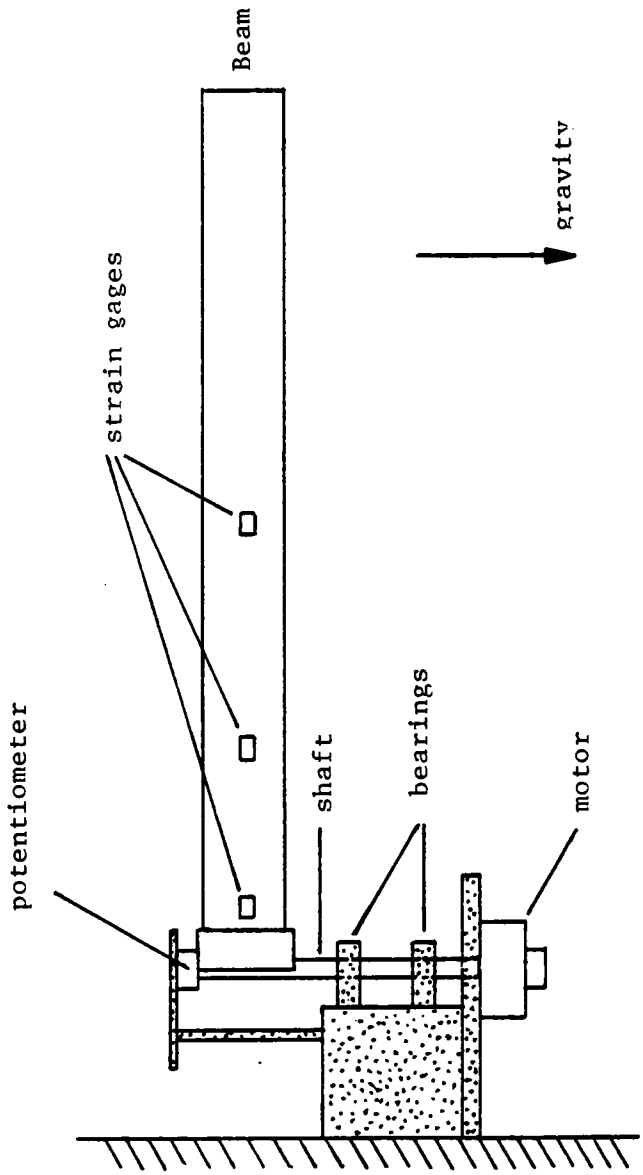

Fig. 2.1 Schematic Representation of System with Instrumentation

mentation problems. Attempts are ongoing for overcoming the deadband with compensation circuits, however the results are preliminary and are not reported here.

BEAM MODEL

Figure 2.2 shows the beam model and its coordinate system. The coordinate vector $\underline{b}$ is body-fixed while $\underline{n}$ is the Newtonian reference.

Important beam parameters are

$$\begin{aligned} L &= 44.5 \text{ in} \\ EI &= 246 \text{ lb} - \text{in}^2 \\ m &= 6.9 \times 10^{-5} \frac{\text{lb} - \text{sec}^2}{\text{in}^2} \end{aligned} \tag{2.1}$$

The generalized coordinates $\theta(t)$ and $y(x,t)$ completely describe the motion of the beam system. However $y(x,t)$ represents a continuous displacement field which is not suited for linear system theory. Hence, the continuous displacement field of the beam is modeled with the three-term Ritz approximation:

$$y(x,t) = \sum_{i=1}^{3} q_i(t)\phi_i(x) \tag{2.2}$$

where $\phi_i(x)$ are chosen shape functions and $q_i(t)$ are their amplitudes. The shape functions used here are the equations for the first three natural vibrating modes of a clamped-free beam. Appendix A.1 shows these equations and briefly discusses their derivation.

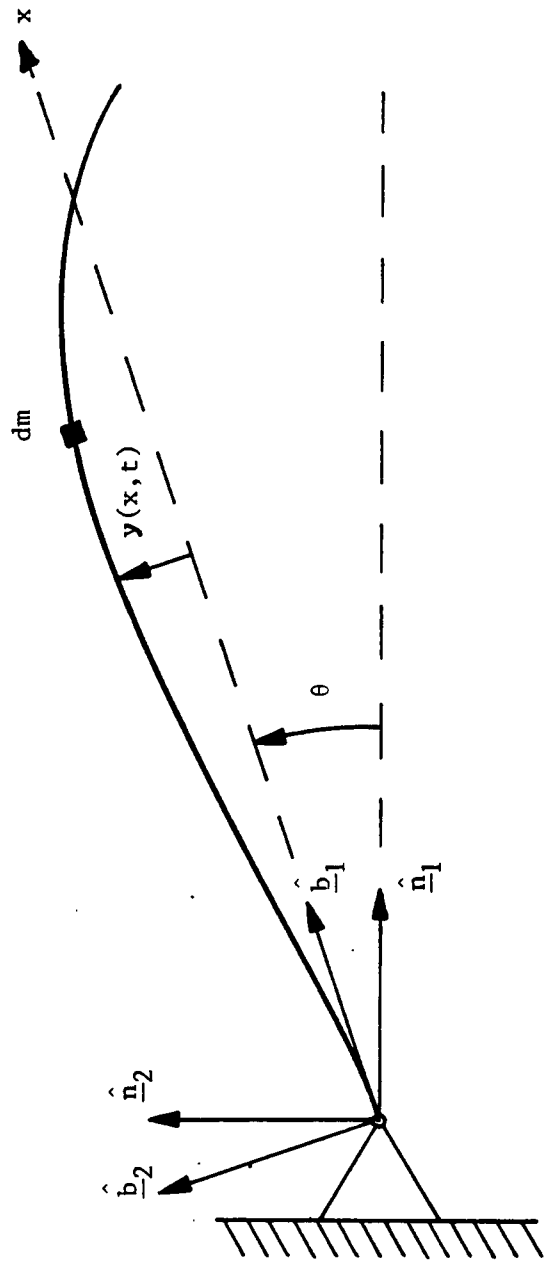

Fig. 2.2 Beam Model with Coordinate System

It can be seen now that the system's dynamic characteristic is completely mathematically represented in terms of the state variables (generalized coordinates):

$$\underline{q} = \begin{bmatrix} \theta \\ q_1 \\ q_2 \\ q_3 \end{bmatrix} \tag{2.3}$$

To arrive at the describing equations of motion, the potential energy, V, and kinetic energy, T, of the beam are written in terms of the generalized coordinates and used in Lagrange's equations. For our model, Lagrange's equations take a standard form:

$$\frac{d}{dt}\left(\frac{\partial T}{\partial \dot{q}_i}\right) - \frac{\partial T}{\partial q_i} + \frac{\partial V}{\partial q_i} = F_i \tag{2.4}$$

The kinetic energy of the beam is formulated as follows. Refering to Fig. 2.2, the position vector, $\underline{R}_p$, of any incremental mass, dm, on the beam is written as

$$\underline{R}_p = x\ \hat{\underline{b}}_1 + y(x,t)\ \hat{\underline{b}}_2 \tag{2.5}$$

It should be noted that beam elongation is neglected and y(x,t) is representing Eq. 2.2. Applying the Transport Theorem yields the velocity of this particle, $\dot{\underline{R}}_p$, with respect to the Newtonian reference frame:

$$\dot{\underline{R}}_p = -\ y(x,t)\ \dot{\theta}\ \hat{\underline{b}}_1 + (y(x,t) + x\ \dot{\theta})\ \hat{\underline{b}}_2 \tag{2.6}$$

The kinetic energy for the whole beam can now be expressed as:

$$T = \tfrac{1}{2} \int_{x=0}^{L} (m(x)\, \dot{\underline{R}} \cdot \dot{\underline{R}})\, dx \tag{2.7}$$

The potential energy of the beam is contained solely in the internal strain energy due to the beam's bending. This can be expressed as

$$V = \tfrac{1}{2} \int_{x=0}^{L} EI \left(\frac{d^2y}{dx^2}\right)^2 dx \tag{2.8}$$

Substituting the kinetic and potential energies into Lagrange's Equations yields four non-linear second order differential equations in terms of the system's generalized coordinates q. After linearizing, the set of coupled linear differential equations looks like (See App. A.2 for details.)

$$\begin{bmatrix} I & a_1 & a_2 & a_3 \\ a_1 & m_1 & 0 & 0 \\ a_2 & 0 & m_2 & 0 \\ a_3 & 0 & 0 & m_3 \end{bmatrix} \begin{bmatrix} \ddot{\theta} \\ \ddot{q}_1 \\ \ddot{q}_2 \\ \ddot{q}_3 \end{bmatrix} + \begin{bmatrix} 0 & 0 & 0 & 0 \\ 0 & k_1 & 0 & 0 \\ 0 & 0 & k_2 & 0 \\ 0 & 0 & 0 & k_3 \end{bmatrix} \begin{bmatrix} \theta \\ q_1 \\ q_2 \\ q_3 \end{bmatrix} = \begin{bmatrix} T_a \\ 0 \\ 0 \\ 0 \end{bmatrix} \tag{2.9}$$

or

$$\underline{M}\ddot{q} + \underline{K}q = \underline{F} \tag{2.9}$$

where $\underline{M}$ is the mass matrix for the beam, $\underline{K}$ is the stiffness matrix and $\underline{F}$ is the input matrix.

Note that no attempt is made here to experimentally model any system damping. However, when it is added later in Chapter 6 the system model will look like

$$\underline{M}\,\ddot{\underline{q}} + \underline{C}\,\dot{\underline{q}} + \underline{K}\,\underline{q} = \underline{F} \tag{2.10}$$

MOTOR AND SYSTEM MODELS

The motor system used in the experiment is a PMI U9M4T dc-servo motor driven by a PMI SSA-54 dc-servo-switching amplifier. Relevant parameters for this equipment are as follows:

$$K_T = 6.1 \text{ oz-in/amp}$$

$$K_B = 0.04297 \text{ volt-sec/rad}$$

$$R_a = 1.025 \text{ ohms}$$

$$L_a = 100.0 \ \mu\text{-henries}$$

$$J_a = .008 \ \frac{\text{oz-in-sec}^2}{\text{rad}}$$

$$B_m = 0.01146 \ \frac{\text{oz-in-sec}}{\text{rad}}$$

$$f_m = 4.5 \text{ oz-in}$$

$$G_A = 2.0 \text{ amps/volt}$$

The second-to-last parameter is the average friction torque in the motor assembly which must be overcome. As mentioned earlier, this nonlinear-torque deadband is unmodeled; hence this parameter has no influence on any analytical results however it will affect experimental results.

Applying Kirchoff's voltage law around the standard armature circuit-motor model shown in Fig. 2.3 yields

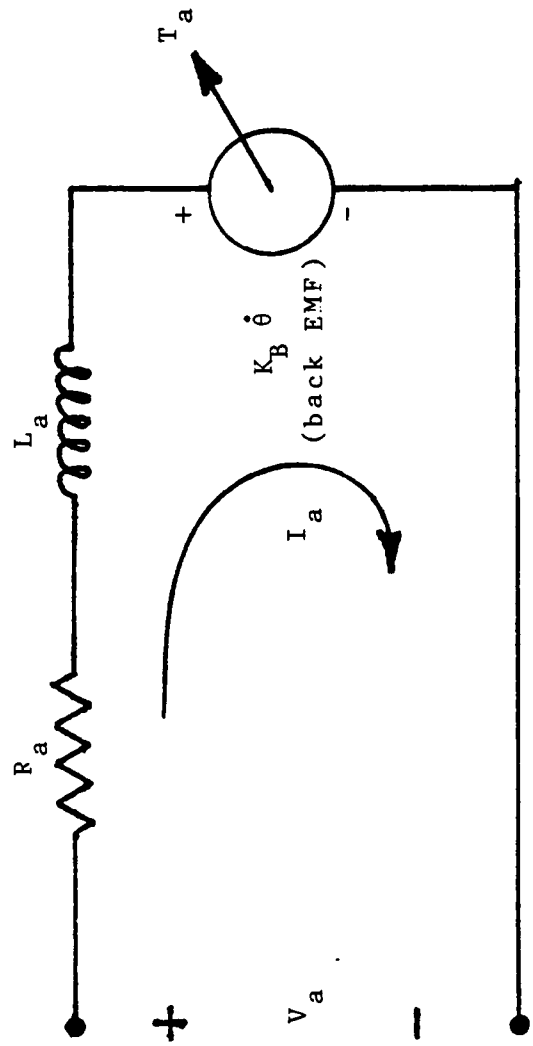

Fig. 2.3 Schematic Diagram of Standard Motor Model

$$V_a = R \cdot I_a + K_b \dot{\theta} \tag{2.12}$$

assuming as usual that the effect of motor winding inductance is small. This is validated since the time constant of the inductor R_a/L_a is several orders of magnitude larger than all others in the system. The motor output torque, $T_a(t)$, can be expressed as

$$T_a = K_T \cdot I_a \tag{2.13}$$

assuming small motor inertia and damping. Solving Eq. 2.12 and Eq. 2.13 for output torque, T_a, results in

$$T_a = \frac{K_T}{R_A} V_a - \frac{K_T K_B}{R_A} \theta \tag{2.14}$$

This is a standard voltage-controlled motor model.

Torque-Controlled Motor/Experimental System

Modifications were made on the PMI switching amplifier according to factory specifications so that the motor/amplifier system performed as a pure current driven-torque source. Therefore internal motor characteristics such as winding resistance or inductance do not effect the input/output (voltage/torque) relationship. Including the gain on the switching amplifier, the model for this system is simply

$$T_a = G_A K_T V_a \tag{2.15}$$

Combining Eq. 2.15 into Eq. 2.11 gives

$$\underline{M}\,\ddot{\underline{q}} + \underline{C}\,\dot{\underline{q}} + \underline{K}\,\underline{q} = \underline{B}\,V_a \tag{2.16}$$

where the element B_1 $\underline{B}$ is given by $B_1 = K_T G_A$. This is the mathematical model of the experimental system.

Voltage-Controlled Motor

The model for a voltage-controlled motor was developed earlier and is given by Eq. 2.14. Combining Eq. 2.14 into Eq. 2.10 gives a set of equations that look similar to Eq. 2.16. Here, however, $B_1 = \frac{G_A K_T}{R_A}$ (including the amplifier gain) and $C_{11} = \frac{K_T}{R_A} K_B + C_{th}$ (C_{th} is a viscous damping term determined in Chapter 6 and is present in both system models.) Comparing the values of B_1 for the two systems shows that they are approximately equal since $R_A = 1.02552$ Hence, the voltage-to-torque input relationships of these two systems are also approximately equal.

The term $\frac{K_T}{R_A} K_B$ is related to motor back EMF and adds damping to the system. It appears only in the voltage-controlled model. Note that this term is essentially the only difference between the voltage-controlled and torque-controlled systems. Hence, comparison of results gives direct information about the influence of back EMF on system performance. For the motor parameters of Eq. 2. , $\frac{K_T}{R_A} K_B = 0.250$. In this thesis, the value of $\frac{K_T}{R_A} K_B$ is exaggerated considerably to a value of 100. As will be seen in Chapter 5, this exaggerated value gives a more distinct difference between systems for stronger comparisons.

INSTRUMENTATION

As shown in Fig. 2.1, the beam/motor system is equipped with a potentiometer and three strain gages. These measuring devices are used to generate voltages which are considered to be the system outputs. The

potentiometer has a voltage across it and its output is proportional to the rigid body angle, θ. The strain gages are connected to bridges whose output voltages are proportional to the strains measured. Thus, the system has an output vector $\underline{m}$(volts) where

$$\underline{m} = \begin{bmatrix} \text{Thm} \\ \text{ST1} \\ \text{ST2} \\ \text{ST3} \end{bmatrix} \tag{2.17}$$

A direct, linear relationship exists between the system outputs, $\underline{m}$, and the state variables, $\underline{q}$:

$$\underline{m} = \underline{T}\,\underline{q} \tag{2.18}$$

where $\underline{T}$ is a matrix of instrumentation gains. This is demonstrated below.

Strain at a point, p, on the beam can be calculated as a function of the modal amplitudes, q_i, by substituting the mode shape equations in Eq. 2.1 into the relationship

$$\text{Strain} = C \cdot \frac{d^2 y(x)}{dx^2}\bigg|_{x=p} \tag{2.18}$$

where C is the half depth of the beam. For example, root strain as a function of modal amplitudes was calculated as

$$\text{Strain}_{(\text{gage 1})} = 75.7\, q_1 + 341\, q_2 + 974\, q_3 \tag{2.19}$$

Since output voltage of the strain gage's bridge is directly proportional to strain, strain measurement output and modal amplitudes are linearly related. The row of the transformation matrix $\underline{T}$, corresponding to ST1 contains the coefficients on the right hand side of Eq. 2.19 multiplied by the bridge gain. Similar relationships exist for ST2 and ST3.

So, in summary, the equations describing system dynamics and system output are

$$\begin{aligned} \underline{M}\,\ddot{q} + \underline{C}\,\dot{q} + \underline{K}\,q &= \underline{B}\,V_a \\ \underline{m} &= \underline{T}\,\underline{q} \end{aligned} \tag{2.20}$$

It is noted again for clarity that matrices $\underline{B}$ and $\underline{C}$ differ for the two models developed. The next section uses these equations in designing the control law for the system.

Chapter 3

CONTROLLER DESIGN

The system model (2-20) is rewritten below

$$\underline{M}\,\ddot{\underline{q}} + \underline{C}\,\dot{\underline{q}} + \underline{K}\,\underline{q} = \underline{B}\,V_a \tag{3.1}$$

$$\underline{m} = \underline{T}\,\underline{q} \tag{3.2}$$

where V_a is the input voltage and $\underline{m}$ is the vector of measurement or output variables. The control strategy adopted here is a form of constant-gain, linear, direct-output feedback.

For exact pole placement, the two systems discussed require both position and velocity measurements (15). The desired feedback law is written as

$$V_a = G_{sys}\,(r - \underline{GP}\,\underline{m} - \underline{GV}\,\dot{\underline{m}}) \tag{3.3}$$

where

r = position reference input

$\underline{m}$ = displacement measurement vector

$\dot{\underline{m}}$ = velocity measurement vector

$\underline{GP}$ = displacement gain vector

$\underline{GV}$ = velocity gain vector

G_{sys} = overall system gain

However, the beam's instrumentation gives only displacement measurements. So for exact pole placement, velocity estimators are added to the system to approximate velocity information. The design of the estimators was based on Mounfield (21). A block diagram of the estimator is shown in Fig. 3.1. Mounfield showed successful implementation on an analog computer in an adaptive control scheme. Its transfer function is written as

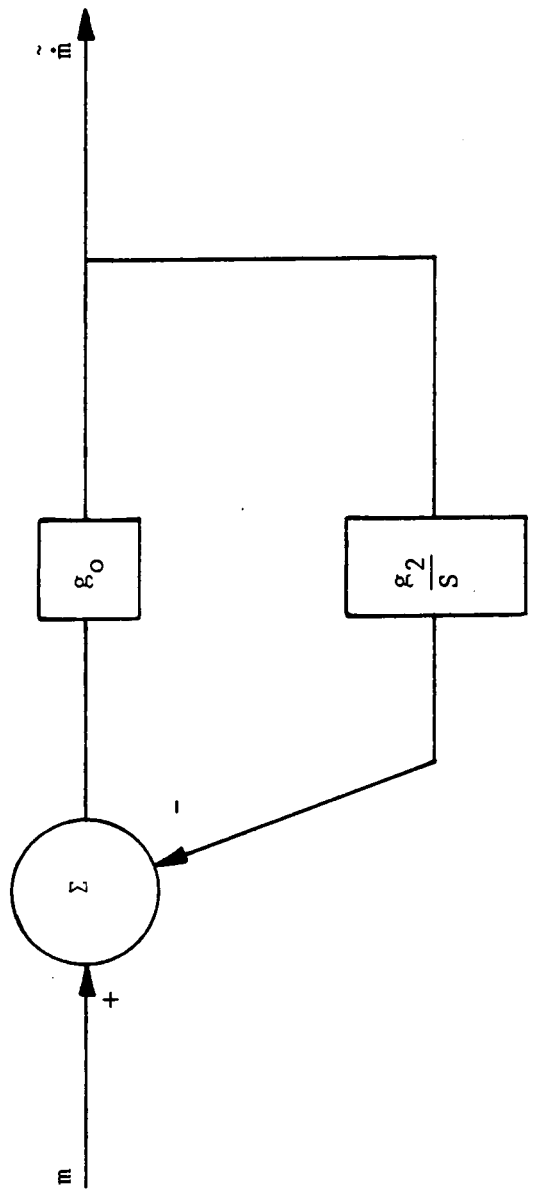

Fig. 3.1 Block Diagram of Velocity Estimator

$$\frac{\tilde{\dot{m}}}{\dot{m}}(s) = \frac{\frac{s}{g_2}}{\frac{s}{g_o g_2} + 1} \tag{3.4}$$

Here $\tilde{\dot{m}}$ represents the estimated velocity of the input m; g_o and g_2 are feedforward and feedback gains respectively. It can be shown (21) that when the system is made fast (i.e. $g_o g_2$ made large) that

$$\frac{\tilde{\dot{m}}}{\dot{m}}(s) \simeq \frac{s}{g_2} \tag{3.5}$$

which when written in the time domain is

$$\tilde{\dot{m}} \simeq \frac{1}{g_2}\dot{m} \tag{3.6}$$

From Eq. 3.4 the differential equation describing the estimators is

$$\dot{\tilde{m}} = g_o m - g_o g_2 \tilde{\dot{m}} \tag{3.7}$$

The frequency response from Eq. 3.4 is shown in the Bode plot in Fig. 3.2. It can be seen that the break frequency of the differentiator is also set by the gain product, $g_o g_2$. Here, the feedback gain in the estimators are held constant at $g_2 = 10$. This specifies the approximate relationship in (3.6). The feed forward gain, g_o, is kept variable but maintained close to a value that sets the differentiator breakpoint frequency near the system's highest modelled frequency (third vibration mode frequency). Thus, filtering in addition to estimation is achieved with this design.

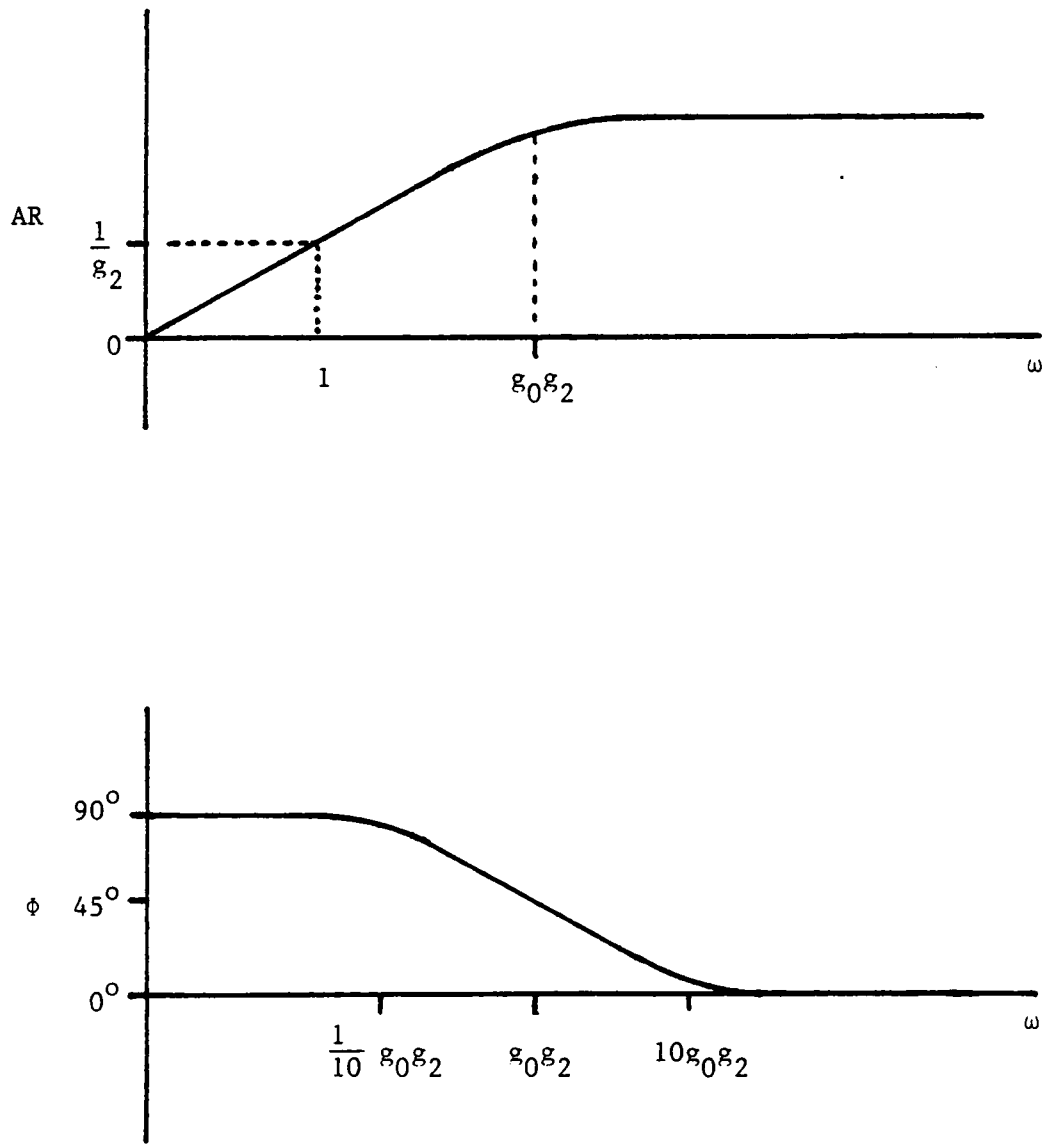

Fig. 3.2 Bode Diagram for Rate Estimators (eq. 3.4)

The velocity of each output variable is now approximated with an estimator. The ideal control law of Eq. 3.2 is rewritten for the real system as

$$Va = GS(r - \underline{GP}\ \underline{m} - \underline{GV}\ \tilde{\dot{\underline{m}}}) \tag{3.8}$$

The complete closed loop system is now described by the set of equations (3.1), (3.2) (3.7) and (3.8).

For clarity, Fig. 3.3 shows a closed-loop block diagram of the model with the designed control law. Here, the equations of the system model (3.1) are represented in block diagram form from standard state-space notation

$$\dot{\underline{z}} = \underline{A}\ \underline{z} \tag{3.9}$$

where

$$\underline{A} = \begin{matrix} 0 & I \\ -\underline{M}^{-1}\underline{K} & -\underline{M}^{-1}\underline{C} \end{matrix} \tag{3.10}$$

It can be seen in the figure and also in equations (3.7) and 3.8) that the system has 13 variable gains: 4 on displacement measurements, 4 on velocity estimates, 4 in state estimators and 1 overall system gain.

In selecting the gains for eigenvalue placement, a unified state space model is the most appropriate system representation. Substituting (3.2) into (3.6) and subsequently substituting this into (3.1) gives

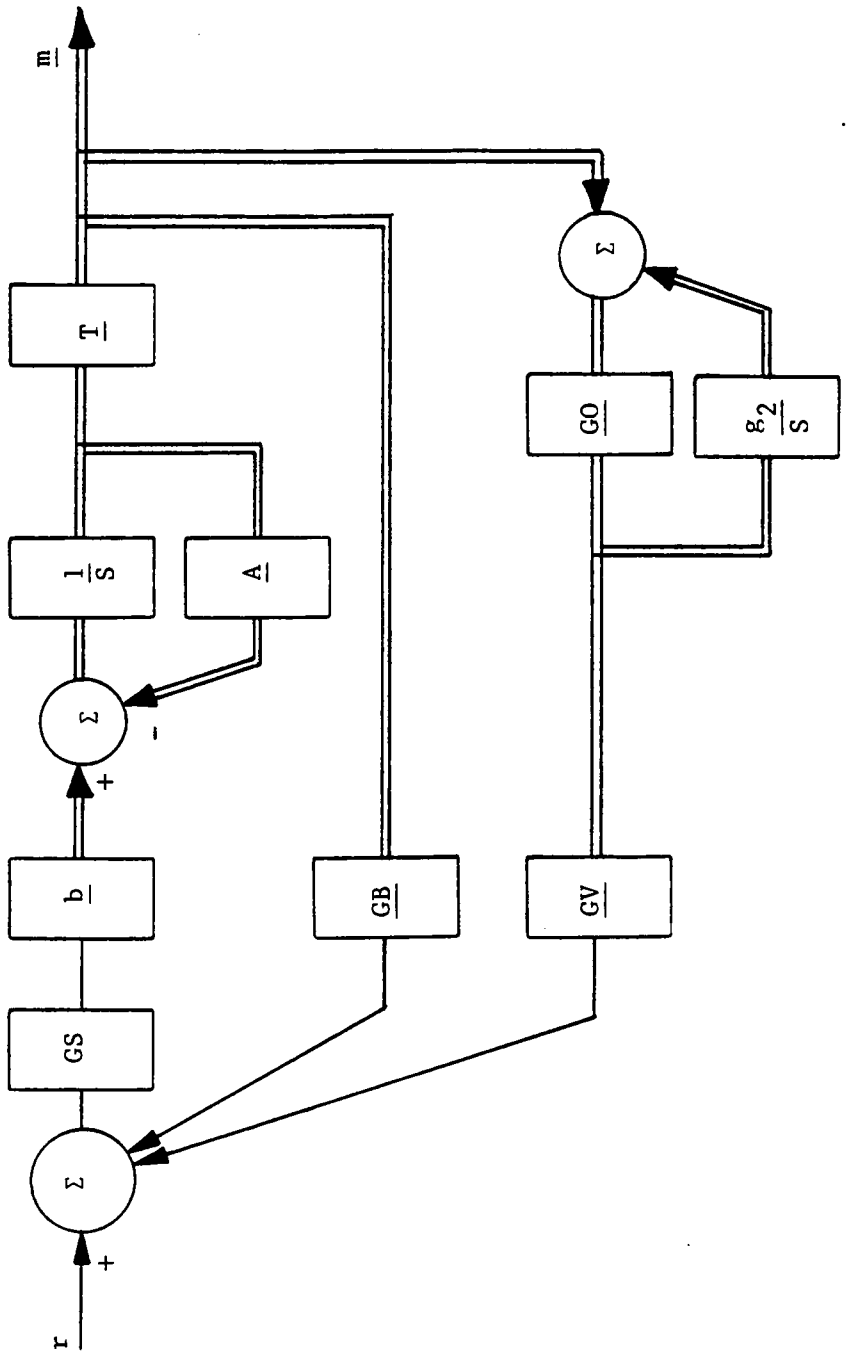

Fig. 3.3 Closed-Loop Block Diagram

$$\underline{M}\,\ddot{\underline{q}} + \underline{C}\,\dot{\underline{q}} + GS\ \underline{B}\ \underline{GV}\ \dot{\tilde{\underline{m}}} + (\underline{K} + GS\ \underline{B}\ \underline{GP}\ \underline{T})\underline{q} = GS\ B\ r \qquad (3.11)$$

Taking the derivative of (3.2) and substituting it into (3.7) gives (written in matrix form)

$$\dot{\tilde{\underline{m}}} = \underline{G_0 T}\ \dot{\underline{q}} - \underline{g_2 G_0}\ \dot{\tilde{\underline{m}}} \qquad (3.11)$$

The four second order equations in (3.9) are combined with the four first order equations in (3.10) into a single twelfth-order homogeneous matrix representation shown below

$$\begin{bmatrix} \underline{I} & 0 & 0 \\ 0 & \underline{M} & 0 \\ 0 & 0 & 0 \end{bmatrix} \begin{bmatrix} \dot{\underline{q}} \\ \ddot{\underline{q}} \\ \dot{\tilde{\underline{m}}} \end{bmatrix} = \begin{bmatrix} 0 & \underline{I} & 0 \\ -\tilde{\underline{K}} & -\underline{C} & -\tilde{\underline{C}} \\ 0 & \underline{G_0 T} & -\underline{G_2 G_0} \end{bmatrix} \begin{bmatrix} \underline{q} \\ \dot{\underline{q}} \\ \tilde{\underline{m}} \end{bmatrix} \qquad (3.12)$$

where $\tilde{\underline{K}} = (\underline{K} + GS\ \underline{B}\ \underline{GP}\ \underline{T})$

$\tilde{\underline{C}} = GS\ \underline{B}\ \underline{GV}$

Rewriting Eq. 3.12,

$$\underline{A}\,\dot{\underline{z}} = \underline{D}\,\underline{z} \qquad (3.13)$$

This state space representation could be made similar to Eq. 3.7 by multiplying both sides of the equation by the inverse of the left hand side. However, this representation shown was maintained for computational reasons.

The gain design procedure outlined in the next section uses this state-space representation. The procedure is an efficient and methodical approach to controller design that produces optimized eigenvalue placement solutions.

Chapter 4

SATISFYING EIGENVALUE CONSTRAINTS AND MINIMIZING SYSTEM SENSITIVITY

This section presents a brief and simplified overview of an iterative procedure that calculates system gains. The algorithm has the flexibility to sequentially meet eigenvalue placement contraints and then minimize an optimality criteria. This procedure has been well developed and documented by Junkins, who refers the reader to any of several publications (16, 17, 18). Most helpful in the successful implementation of this algorithm was Bodden (22, 23) and direct conversation with Dr. Junkins.

The algorithm is driven by eigenvalue sensitivity to variable parameter (gain) changes. To help insure convergence of the interactions, two built-in characteristics maintain a "local linearity" condition. The constraint set is made "portable;" that is, the desired constraint is met by marching through and meeting a series of stepped constraints from the initial set of eigenvalue positions to the final desired set. In addition, the stepped solutions are always kept in the same "neighborhood" by forcing the gain changes to minimize a correction norm.

The constraints considered in this thesis are inequality constraints on the real part of the system eigenvalues. That is, all system eigenvalues are forced to the left of some line in the left half of the s-plane. This is written as

$$\text{Real}\ (\lambda_i) < -b_i \tag{4.1}$$

The real part of an eigenvalue describes decay characteristics; that is if Real $(\lambda_i) = b_i$, then the time response decays according to $e^{-b_i t}$. By constraining all beam related eigenvalues to the left of the same line, all system dynamics will decay within the envelope of $e^{-b_i t}$. Hence, by moving the constraint b_i to the left, the system can be made "faster." Since dynamic estimators are also included in the state model, their eigenvalues are forced to a vicinity that gives the desired cutoff frequency discussed in Chapter 3. In addition, a constraint is placed on the imaginary part of the lowest frequency eigenvalue to help stabilize the algorithm by preventing bifurcations. (Such as complex roots moving to the real axis and bifurcating along that axis.)

Once the eigenvalue constraints are met, the algorithm allows for minimization of a performance index while still maintaining the "hard" eigenvalue constraints. The performance index minimized here is a normalized eigenvalue sensitivity function to small gain perturbations.

The state space formulation of Eq. 3.13 is rewritten below

$$\underline{A}\,\dot{\underline{z}} = \underline{B}\,\underline{z} \tag{4.1}$$

The left and right eigenvalue problems for this equation are

$$\text{right:}\quad \lambda_i \underline{A}\,\underline{\phi}_i = \underline{B}^T \underline{\phi}_i \qquad \text{left:}\quad \lambda_i\,\underline{A}\,\underline{\psi}_i = \underline{B}^T \underline{\psi}_i \tag{4.2}$$

where

λ_i = i^{th} eigenvalue

ϕ_i = i^{th} right eigenvector

ψ_i = i^{th} left eigenvector

The eigenvalues are normalized according to

$$\underline{\psi}_j^T \underline{A}\, \underline{\phi}_i = \delta_{ij} \qquad \underline{\psi}_j^T \underline{B}\, \underline{\phi}_i = \delta_{ij}\lambda_i \tag{4.3}$$

The matrix $\underline{B}$ in Eq. 4.1 is parametrized in terms of the gain vector $\underline{G}$, so $\underline{B} = \underline{B}(\underline{G})$. Clearly then, the following statements are also true,

$$\lambda_i = \lambda_i(\underline{G}) \;,\; \underline{\psi}_i = \underline{\psi}_i(\underline{G}) \;,\; \underline{\phi}_i = \underline{\phi}_i(\underline{G}) \tag{4.4}$$

The first and second partial derivatives of the eigenvalues are derived from Eqs. 4.3-4.5 and are essential to the development of this algorithm. Their derivation and results are well documented (16, 24). As they pertain to this problem, the first and second partial derivatives of the eigenvalues with respect to gains are

$$\frac{\partial \lambda_i}{\partial G_j} = \underline{\psi}_i^T \left[\frac{\partial \underline{B}}{\partial G_j}\right] \underline{\phi}_i \tag{4.5}$$

$$\frac{\partial^2 \lambda_i}{\partial G_k\, \partial G_j} = \psi_i^T \left[\frac{\partial^2 \underline{B}}{\partial G_k\, \partial G_j}\right] \phi_i + \sum_{m=1}^{n} \left[\frac{\psi_i^T G_{ij} \phi_m \psi_i^T G_{ik} \phi_i + \psi_m^T G_{ij} \phi_i \psi_i^T G_{ik} \phi_m}{(\lambda_i - \lambda_k)} \right] \tag{4.6}$$

A constraint violation vector is defined as

$$\underline{\Delta\gamma} = \underline{\gamma}_D - \underline{\gamma}(\underline{G}) \tag{4.7}$$

where

$\underline{\gamma}_D$ = vector of desired eigenvalue positions (constraints)

$\underline{\gamma}(\underline{G})$ = vector of current eigenvalue positions

$\Delta\underline{\gamma}$ = vector of constraint residuals.

The vector $\underline{\gamma}_D$ includes all eigenvalue constraints imposed on the system. Since these are inequality relationships given by Eq. 4.1, only violated constraints are penalized. Therefore if a particular constraint is not violated, its residual is set equal to zero.

If large eigenvalue movements are demanded by the constraint vector, convergence to a solution may be unreliable. Therefore, a parameterized family of intermediate constraint vectors is defined as

$$\underline{\gamma}(\varepsilon) = \varepsilon\, \underline{\gamma}_D + (1-\varepsilon)\underline{\gamma}(\underline{G}_o) \tag{4.9}$$

where

$\underline{\gamma}(G_o)$ = vector of initial eigenvalue positions.

By sweeping the parameter ε from 0 to 1, it can be seen that $\gamma(\varepsilon)$ marches from the initial eigenvalue positions to the desired positions in the constraint set.

Replacing $\underline{\gamma}_D$ in Eq. 4.8 with $\gamma(\varepsilon)$ in Eq. 4.9 gives

$$\Delta\, \underline{\gamma} = \underline{\gamma}\,(\varepsilon) - \underline{\gamma}\,(\underline{G}) \tag{4.10}$$

The adjustable step size in ε dictates the magnitude of the constraint violations and thus the rate of convergence.

The iteration procedure seeks the gain correction vector $\underline{\Delta G}$ in

$$\underline{G} = \underline{G}_c + \underline{\Delta G} \tag{4.11}$$

where

$\underline{G}_c$ = vector of current gains

$\underline{G}$ = vector of gains necessary to meet constraint $\Gamma(\varepsilon)$

The gain correction vector, $\underline{\Delta G}$ is related to the constraint violation vector $\Delta \underline{\gamma}$ through the first-order Taylor Series approximation

$$\Delta \underline{\gamma} = \left[\frac{\partial \underline{\gamma}}{\partial \underline{G}} \right] \underline{\Delta G} \tag{4.12}$$

In the original applications of this algorithm (16), large vectors (>50) of variable feedback gains and structural parameters were used to meet a much smaller vector (<20) of eigenvalue constraints. This created an infinity of solutions for $\underline{\Delta G}$ in Eq. 4.12. Consequently a minimum gain correction vector was sought that solved Eq. 4.12 and minimized

$$||\partial \underline{G}|| = \underline{\Delta G}^T \underline{W} \underline{\Delta G} \tag{4.13}$$

The resulting gain correction equation is

$$\underline{\Delta G} = \underline{W}^{-1} \underline{Q}^T \left[\underline{Q} \underline{W}^{-1} \underline{Q}^T \right]^{-1} \Delta \underline{\gamma} \tag{4.14}$$

Q is a matrix of constraint (eigenvalue) sensitivities. For constraints on the real parts of eigenvalues, matrix elements are given by the real parts of values calculated with Eq. 4.6.

Recursive iterations with Eq. 4.14 on marching constraints defined by Eq. 4.10 will yield a gain vector that will make the system meet its desired eigenvalue constraints.

It is interesting to note that the algorithm can be used to generate minimum gain norm solutions. If the initial, starting gain set is given very small or zero values, the continuously minimized gain correction norm implies an approximate minimum gain norm solution. This design solution is used throughout this thesis.

Notice also that the gain correction equation (Eq. 4.14) is derived from the condition of more design variables (gains) than constraints. In some applications in this thesis, this relationship changes from an inherent algorithm characteristics to an actual restriction on the use of this algorithm. This will be seen while focusing on experimental implementation in Chapter 8.

The performance index used in this thesis is a normalized measure of eigenvalue sensitivity

$$PI = \sum_{j} \sum_{i} \left(\frac{G_i}{Re(\lambda_j)} \cdot \frac{\partial(Re(\lambda_j))}{\partial G_i} \right) \tag{4.15}$$

Each term in this sum expresses a percent change in the real part of an eigenvalue for a unit percent change in a gain. The value of the PI is therefore the sum of the square of all constraint sensitivities to all design gains. Thus, the smaller the number, the more robust in general the system is to small perturbations in the calculated gain values.

It is desired to minimize this performance index while maintaining the desired eigenvalue constraints. The procedure is relatively straight-forward and involves supplementary calculations in which the constraint vectors and the sensitivity matrix are augmented with an additional row for PI. Gains are first calculated to satisfy eigenvalue constraints; these are then used as starting gains in the supplimentary calculations. The sensitivity matrix, $\underline{Q}$ is augmented with a row of the first partial derivatives of the sensitivity norm with respect to gains

$$\frac{\partial PI}{\partial G_k} = \sum_i \sum_j 2\left(\frac{G_i}{\lambda_j} \cdot \frac{\partial \lambda_j}{\partial G_i}\right)\left(\delta_{ik} \frac{1}{\lambda_i} \cdot \frac{\partial \lambda_i}{\partial G_i} + \frac{G_i}{\lambda_j} \cdot \frac{\partial^2 \lambda_j}{\partial G_k \, \partial G_i}\right) \qquad (4.16)$$

where δ_{ik} = dirac function

Note that $\frac{\partial \gamma_j}{\partial G_i}$ is calculated from the real part of Eq. 4.5 and $\frac{\partial^2 \gamma_j}{\partial G_k \, \partial G_i}$ is calculated from the real part of Eq. 4.6. The constraint vector $\underline{\gamma}$ is augmented with a term that marches through a series of incrementally smaller desired PI numbers. All other vector elements remain set at the original desired eigenvalue constraints. Thus, by recursively iterating with Eq. 4.14, gains are changing to lower the performance index while still enforcing "hard" eigenvalue constraints. When the algorithm can no longer iterate, the performance index is said to be minimized.

Thus in two sequential steps this algorithm can yield a minimum gain norm solution and a minimum sensitivity norm solution. Each of these solutions is obviously important in its own right. FORTRAN code was written for the algorithm and was successfully applied. Results and valuable comparisons of solutions types and system types are in Chapter

7. The next chapter discusses uncontrolled, open-loop characteristics of the systems.

Chapter 5

OPEN-LOOP RESPONSES

This section discusses the natural responses of the two open-loop systems as related to motor models. Setting u = 0 in Eq. 2.20, the equations for both models can be written as:

$$\begin{aligned} \underline{M}\,\ddot{\underline{q}} + \underline{C}\,\dot{\underline{q}} + \underline{K}\,\underline{q} &= 0 \\ \underline{m} &= \underline{T}\,\underline{q} \end{aligned} \tag{5.1}$$

Recalling from system modeling the only differences in the two models arise solely from the different motor models in each. In Eq. 5.1, the only term related to motor parameters is $C(1,1) = \frac{K_T}{R_A} K_B$. Hence, motor characteristics interact with the open-loop system primarily by introducing angular damping through the motor's back EMF.

The torque-controlled motor model is a special case of this. The switching amplifier has its own feedback loops which essentially isolate all motor characteristics including back EMF from the system. In other words, $\frac{K_T}{R_A} K_B = 0$ and $\underline{C} = \underline{0}$ in Eq. 4.1. The motor acts as a pure torque source hence there is no interaction between motor and beam dynamics.

Fig. 5.1a shows the positions of the open-loop eigenvalues for the torque-controlled system. As can be seen there is no damping in any of the system modes. The frequencies of the vibration modes are $\omega_1 = 13.9$, $\omega_2 = 37.5$ $\omega_3 = 68.4$ (units in rad/sec). The rigid body mode has a pair of poles at the origin. If oscillations were introduced into this model, they would continue forever.

In comparison to this model, the voltage controlled motor model has a strong back EMF. The motor and system dynamics are strongly

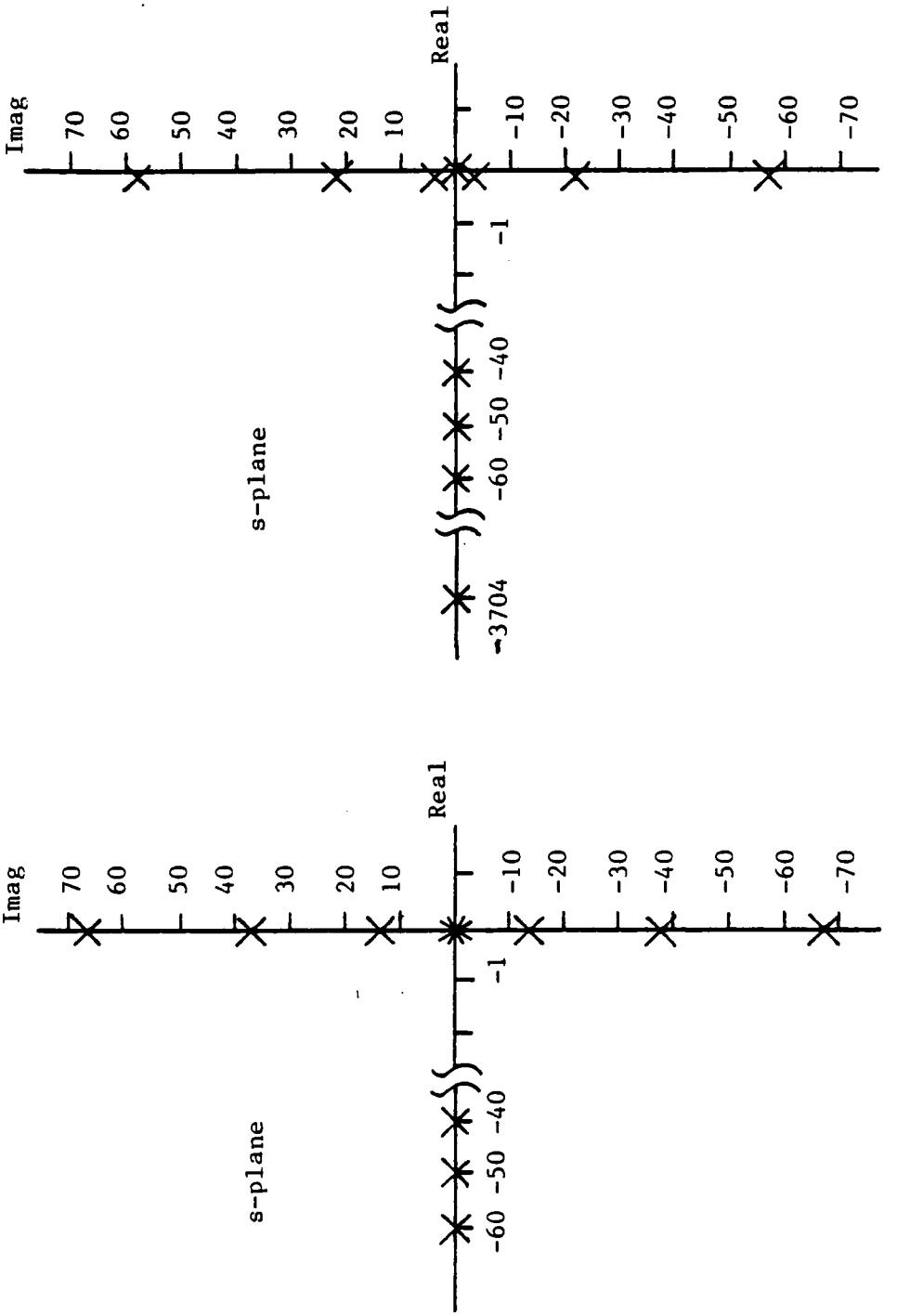

(a) Experimental Model

(b) Example System

Fig. 5.1 Open-Loop Eigenvalues of System Models

coupled. Figure 5.1b shows the eigenvalue positions of this system model. The light damping in the vibration modes is caused by this inherent coupling of motor and beam dynamics through the motor's back EMF. This system's vibration frequencies are $\omega_1 = 3.35$, $\omega_2 = 21.0$, $\omega_3 = 58.8$ (units are in rad/sec); the system is not as stiff as for the torque controlled case. If oscillations were introduced into this system they would decay, but very slowly.

As an aside, note that these natural vibration frequencies are very close to those of a clamped-free beam with similar parameters. This is expected since a strong back EMF essentially inhibits angular motion; hence the beam would vibrate with little influence on angular position. While not nearly as accurate, the natural vibration frequencies of the torque-controlled motor are close to those of a pinned-free beam. This too is as expected since the lack of back EMF allows for free, undamped angular motion. Table 5.1 shows comparisons of the vibrating frequencies for the two systems.

Fig. 5.1 suggests that the more back EMF there is in the motor, the more damping there is in the system. This, however, is not the case. It was found that system response characteristics are highly sensitive to damping introduced through back EMF. Fig. 5.2 shows a root locus of eigenvalues of Eq. 5.1 as $\frac{K_T}{R_A} K_B$ is varied from 0 to ∞. As seen, as this parameter increases some poles move further into the left side of the s-plane but then reverse on themselves and return to the imaginary axis. Other poles move deep into the left side but then "crash" the real axis and separate. Note that the damping characteristics of the two motors considered here places their system eigenvalues at the extreme, not-so-sensitive, opposite ends of this unusual relationship.

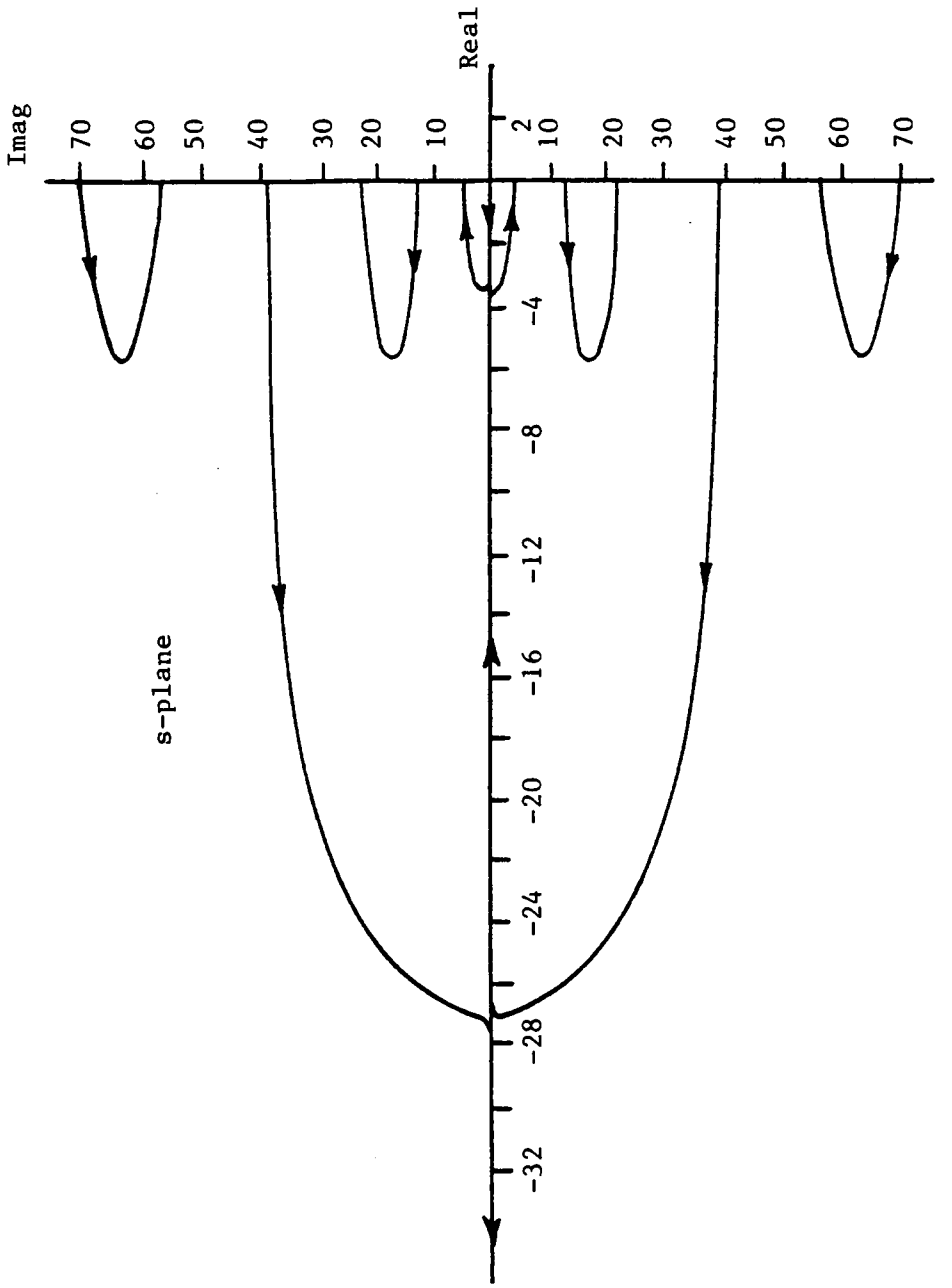

Fig. 5.2 Root Locus of System Eigenvalues as $\frac{K_T}{R_A} K_B$ varies from 0 to ∞.

Table 5.1 Comparison of Vibrating Frequencies between Beam/Motor Systems and other classic (textbook) Systems (units in rad/sec)

	beam in example system	clamped-free beam
1st mode	3.35	3.36
2nd mode	21.0	21.0
3rd mode	58.8	58.8

	beam in experimental system	pinned-free beam
1st mode	13.8	14.7
2nd mode	37.7	47.6
3rd mode	68.9	99.4

This relationship becomes even more significant when taken out of the context of open-loop sensitivity to back EMF. Any angular damping present in the system will move eigenvalues along the locus of Fig. 5.2. Sources of this damping include back EMF, inherent angular friction, and perhaps most importantly, angular rate feedback.

Adding angular rate feedback without a good estimate of inherent system damping characteristics may not improve system performance. As seen, excessive damping actually degrades response. Hence, knowledge of system damping characteristics and perhaps even a feel for system's sensitivity to damping is critical. Therfore, the next chapter uses experimental data to arrive at estimates of inherent system damping for the beam/rotor model.

Chapter 6

SYSTEM DAMPING AND MODEL ACCURACY

The system model developed in Chapter 2 did not include structural damping primarily since it is difficult to predict mathematically. Here, by analyzing experimental data, damping in the system is estimated and included in the model. These estimates are arrived at primarily though logarithmic decrement concepts.

Damping is assumed to originate from two sources: internal structural damping in the beam and friction effects in the motor and bearings. These effects, particularly those due to friction, are a combination of viscous (linear) and coulomb (non-linear) damping. The linear system theory developed in Chapters 2-4 requires that the damping be estimated with linear terms for it to be useful. Therefore, structural damping in the beam is modeled with terms directly proportional to the rates of three modal amplitude state variables and damping in the motor and bearings is modeled as proportional to angular rate. Cross-coupled damping is not attempted to be modeled.

These two sources of damping are estimated separately. First, the beam is isolated from the motor and its internal damping is determined. Then, angular damping is approximated by considering the beam/motor system's response with position feedback alone.

The beam is removed from the motor and mounted in a heavy vise. It is given an approximate first mode deflection of $q_1 = 2.73$ (6" tip deflection) and allowed to oscillate freely. Beam response is shown for the strain outputs in Fig. 6.1. Note that the oscillations in ST1 and

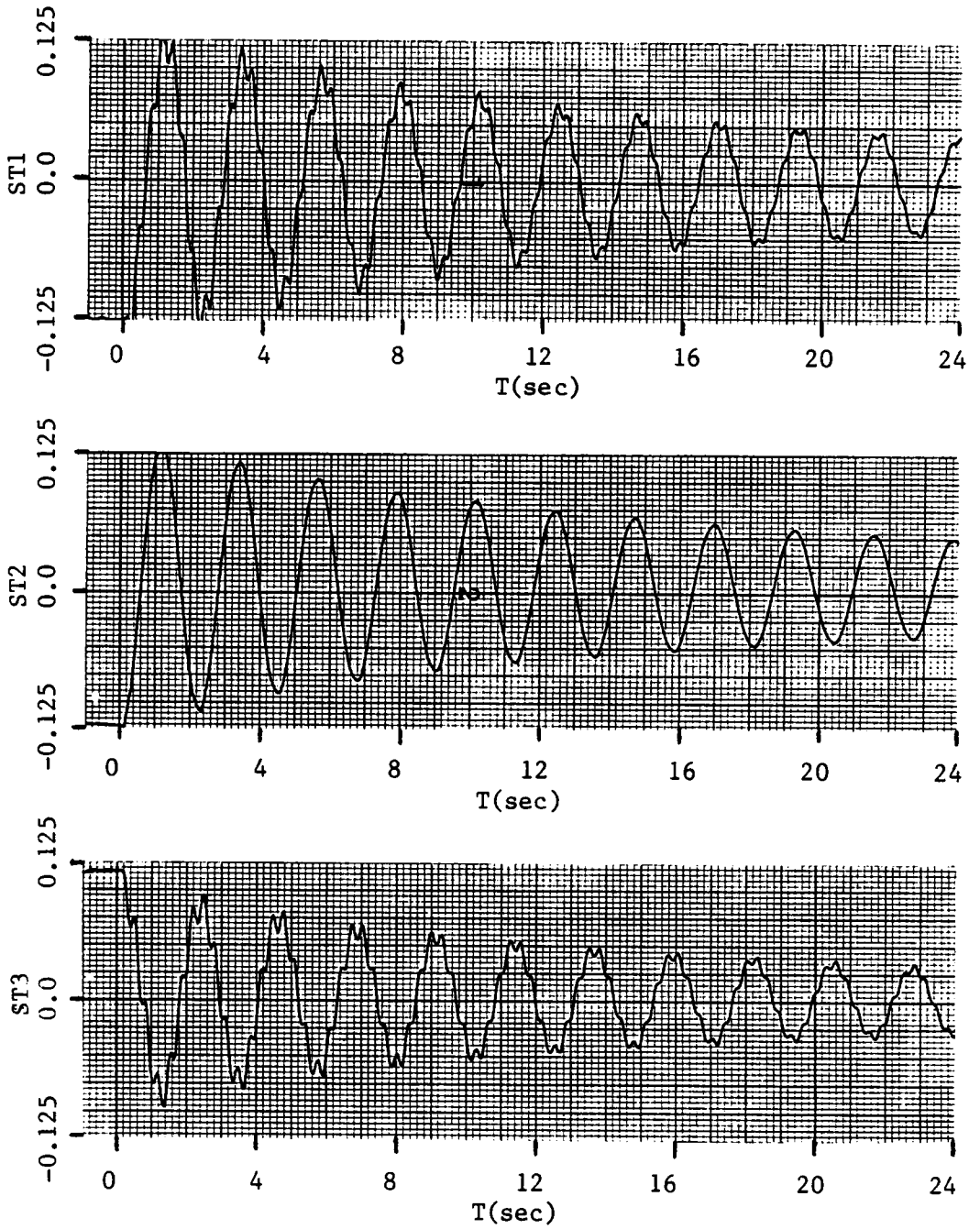

Fig. 6.1 Free Vibration Response of Clamped Beam to an Initial First Mode Deflection (units in volts)

ST3 are slightly "dirty" while ST2 is quite clean. This simply says tha small second mode vibrations were also induced. Since ST2 is the cleanest signal, it will be used to determine the structural damping in the first vibration mode. The logarithmic decrement of this response indicates a damping ratio of 1.02%. With this an equivalent damping term is calculated (see App. B.1).

It would be very hard to excite relatively pure second and third mode vibrations so damping for these modes is estimated using the approximate relationship (25).

$$D_{eq} \alpha \frac{1}{w} \tag{6.1}$$

Fig. 6.2 shows a comparison of experimental data and simulation results for ST2. Fig. 6.3 shows the same comparison for ST1 only over a more complete time history (120 sec). As seen, this technique gives a good approximation of structural damping in the beam.

Next, angular damping is estimated using the complete beam/motor system. By feeding back an angular position signal only, the system would act similarly to an ideal spring/inertia system if there was no damping present. Therefore the rate of decay in the system's response to an initial angular displacement gives information on angular damping. The implemented control law looks like

$$V_a = -1.8\ \theta \tag{6.2}$$

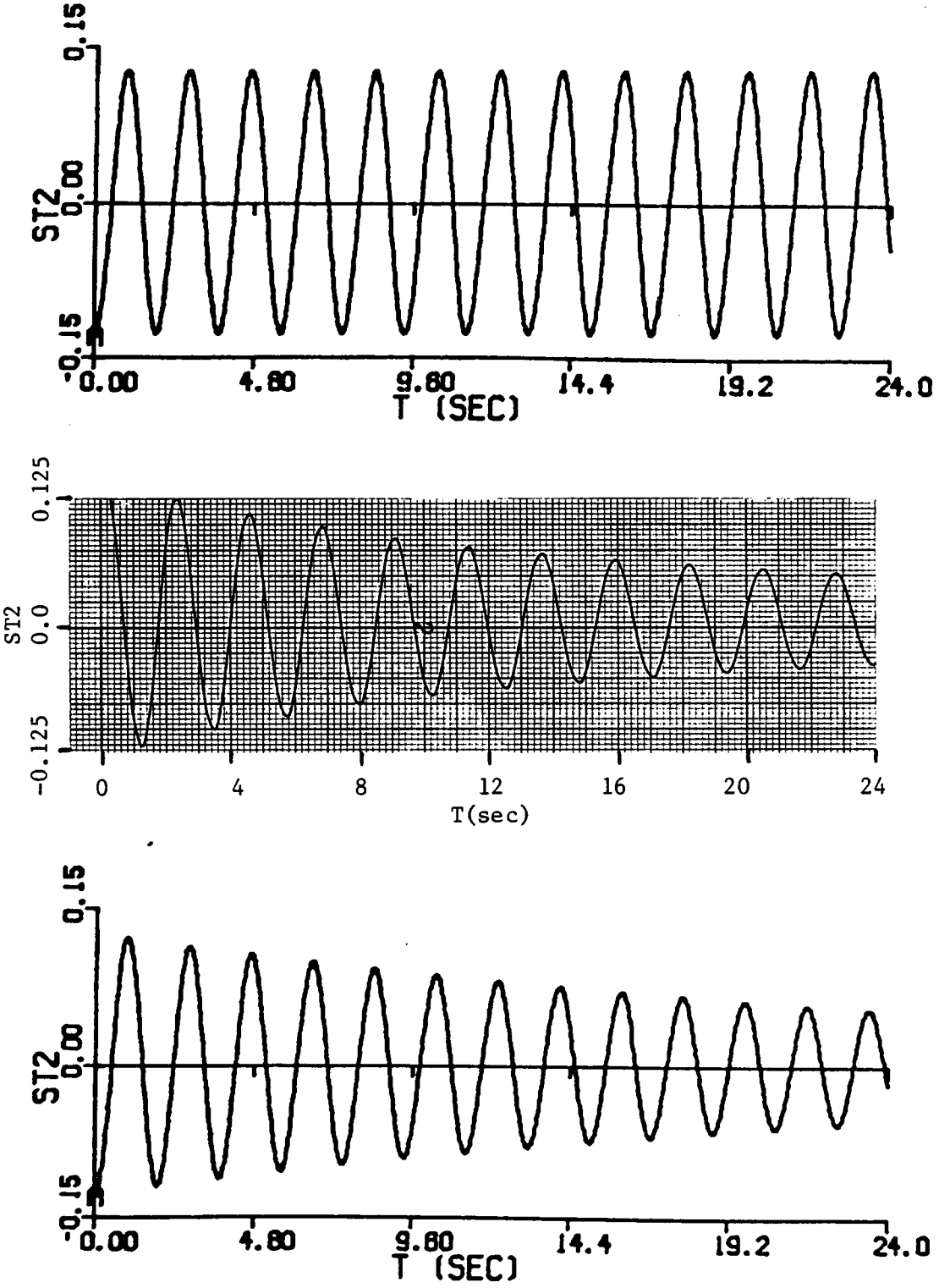

Fig. 6.2 Comparison of Experimental Data and Simulated Data Before and After Damping was Included in Model for Free Vibration of Boom After an Initial 1st Mode Deflection (units in volts)

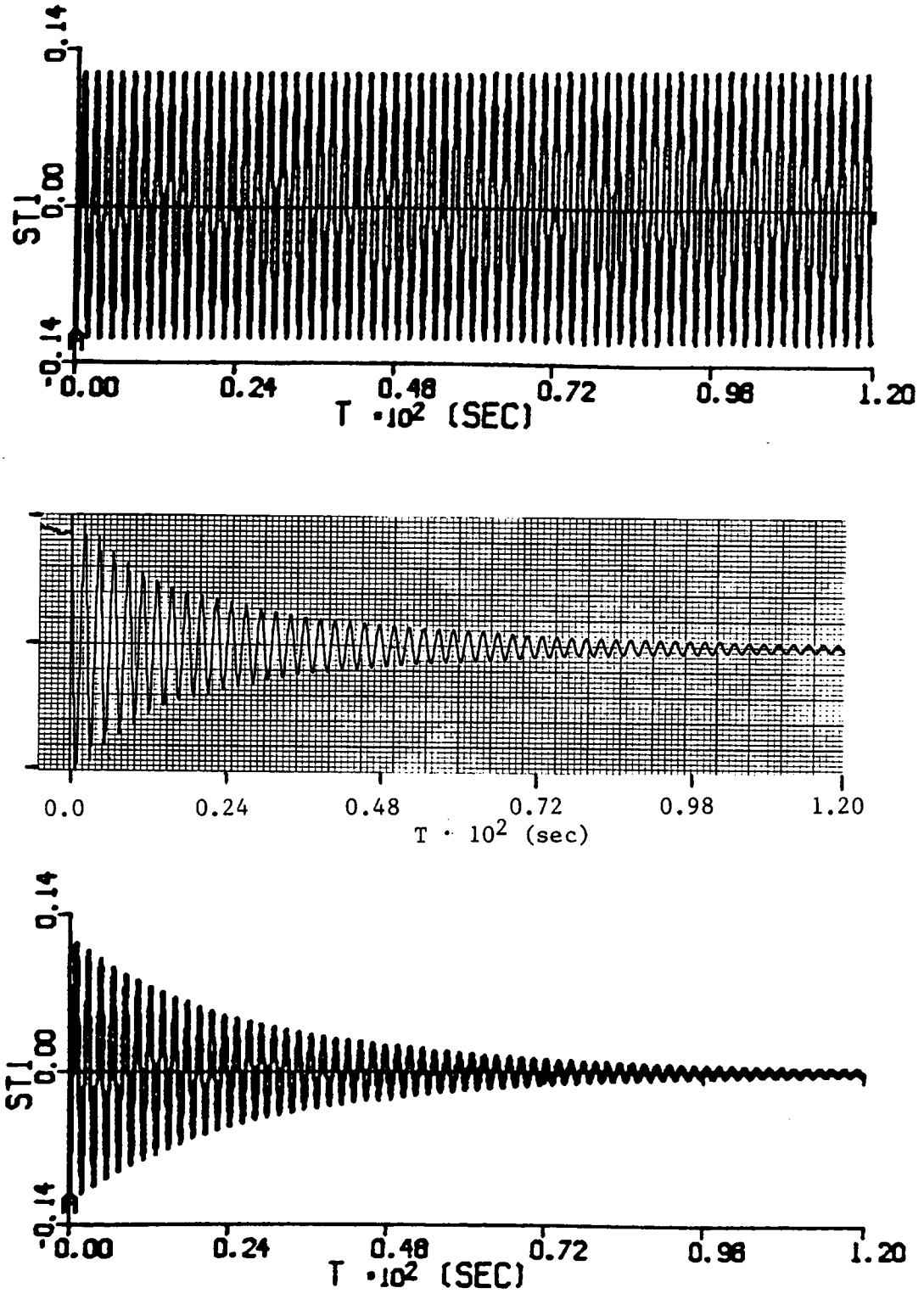

Fig. 6.3 Comparison of Experimental Data with Simulated Data Before and After Damping was Included in Model for Free Vibration of Beam After Initial 1st Mode Deflection (units in volts)

The logarithmic decrement in this system's response indicates a rather large damping ratio of 11.8%; from this equivalent angular damping is calculated (App. B.2) and included in the system model. Fig. 6.4 shows a comparison of experimental and simulated responses of Thm to a 45^{o} initial angular displacemnt. Similar comparisons are shown in Figs. 6.5, 6.6 and 6.7 for the strain signals. As seen, the prominent shape of the responses has been improved. However, representation of high frequency content has been sacrificed. The simulations with no angular damping represent the high frequency content much more accurately, while simulations with angular damping better represent low frequency content. This indicates either the non-linear or the coupled nature of the sources of damping in this system; neither of which could be modeled here. Both beam and angular damping are included in the final model since lower frequencies are the most prevalent (and visible) in the system's repsonse.

For a further check on the accuracy of this model, the control law of Eq. 6.3 was taken one step further to include an estimated velocity signal on θ. The control law now looks like

$$V_a = -1.8\ \theta - 14.6\ \dot{\theta}_{est} \qquad (6.3)$$

Comparisons of experimental and simulation results are shown for Thm, ST1, ST2 and ST3 in Figs. 6.8-6.11, respectively.

Good accuracy is seen in all reponse comparisons. With this confidence in the system model, the control strategies discussed in Chap. 4 are attempted next.

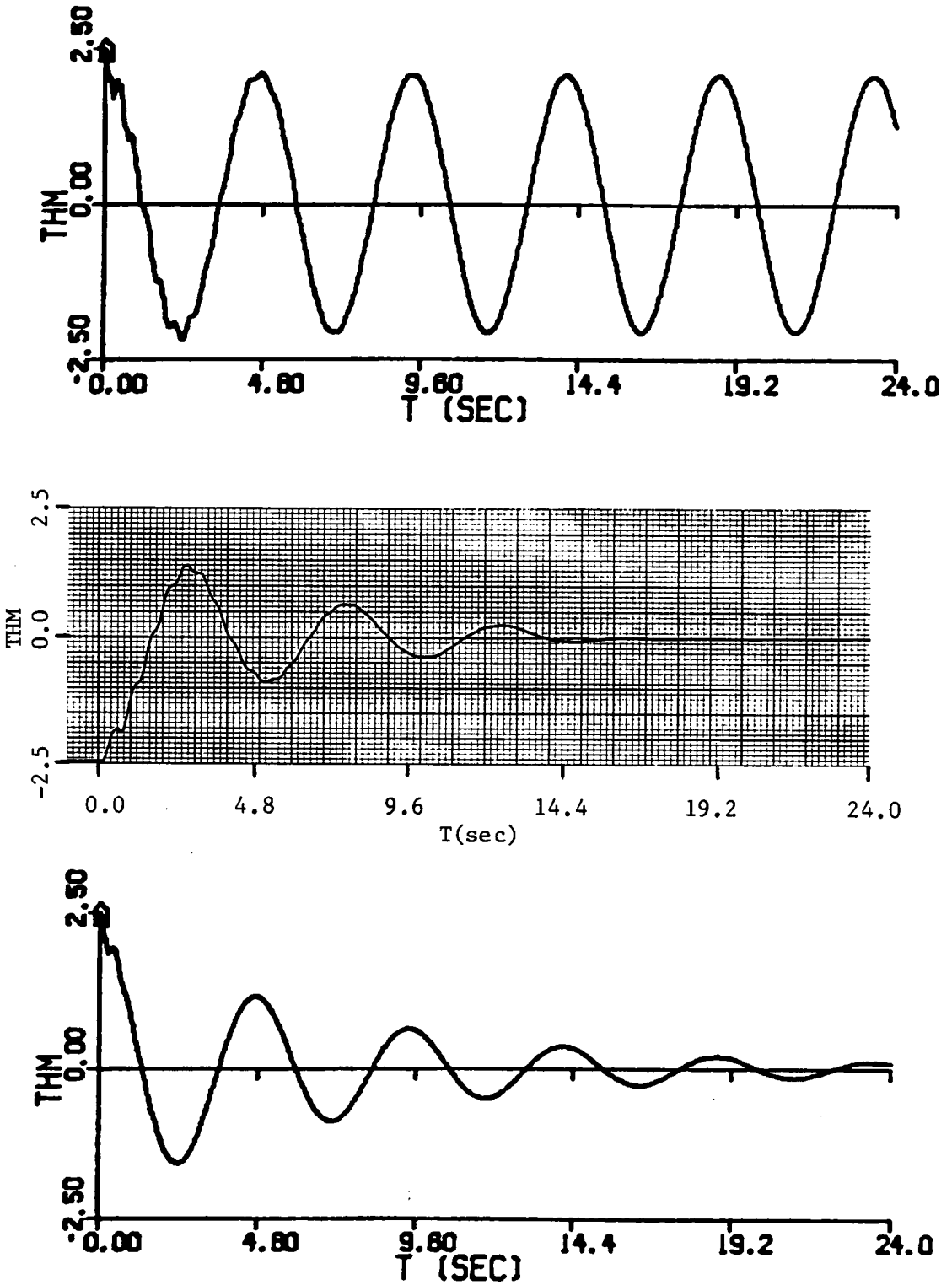

Fig. 6.4 Comparison of Experimental Data and Simulated Data Before and After Damping was Added to Model for System with Angular Position Feedback Subject to 45° Initial Displacement (units in volts)

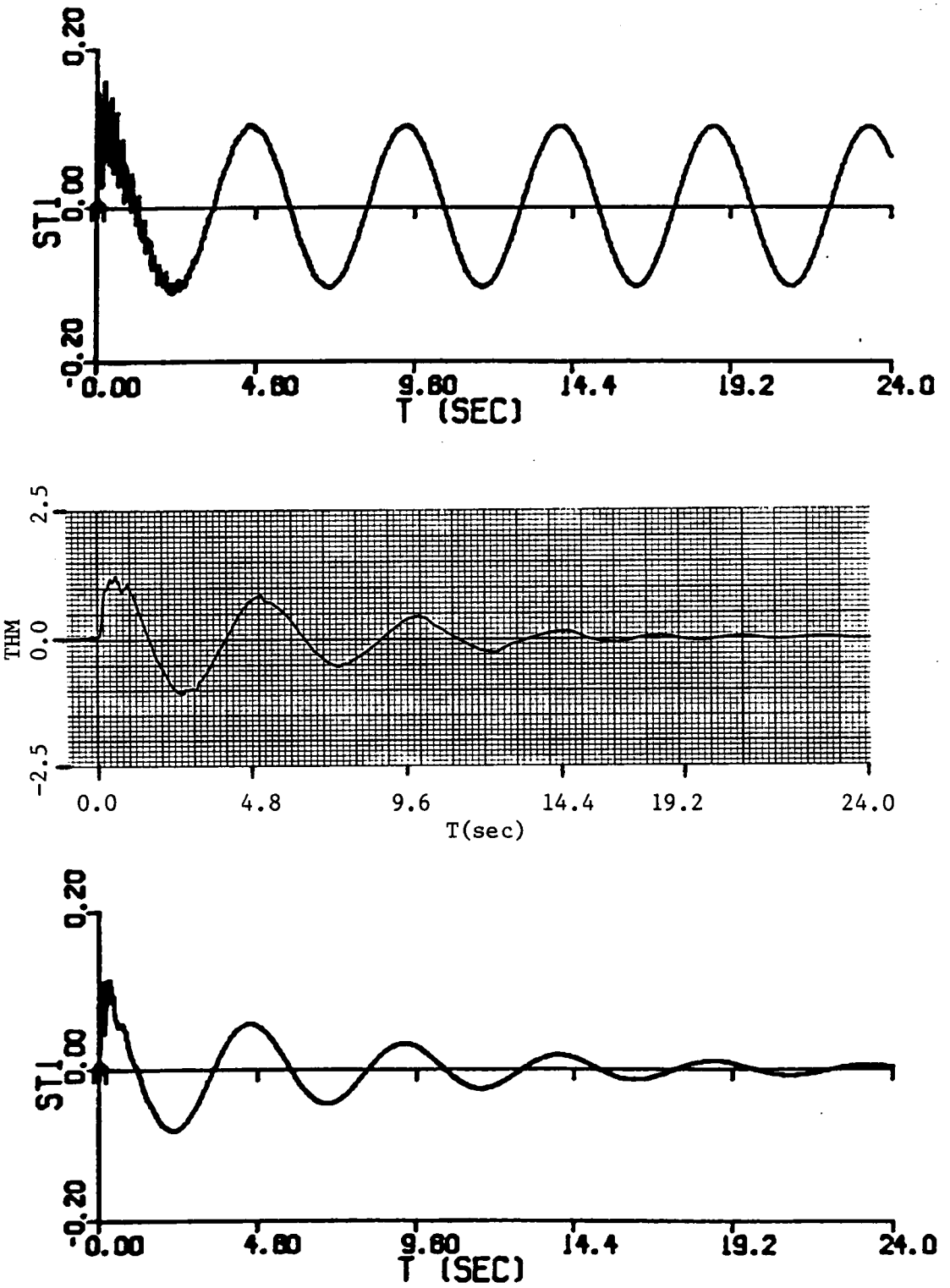

Fig. 6.5 Comparison of Experimental Data and Simulated Data Before and After Damping was Added to Model for System with Angular Positiion Feedback Subject to 45° Initial Displacement (units in volts)

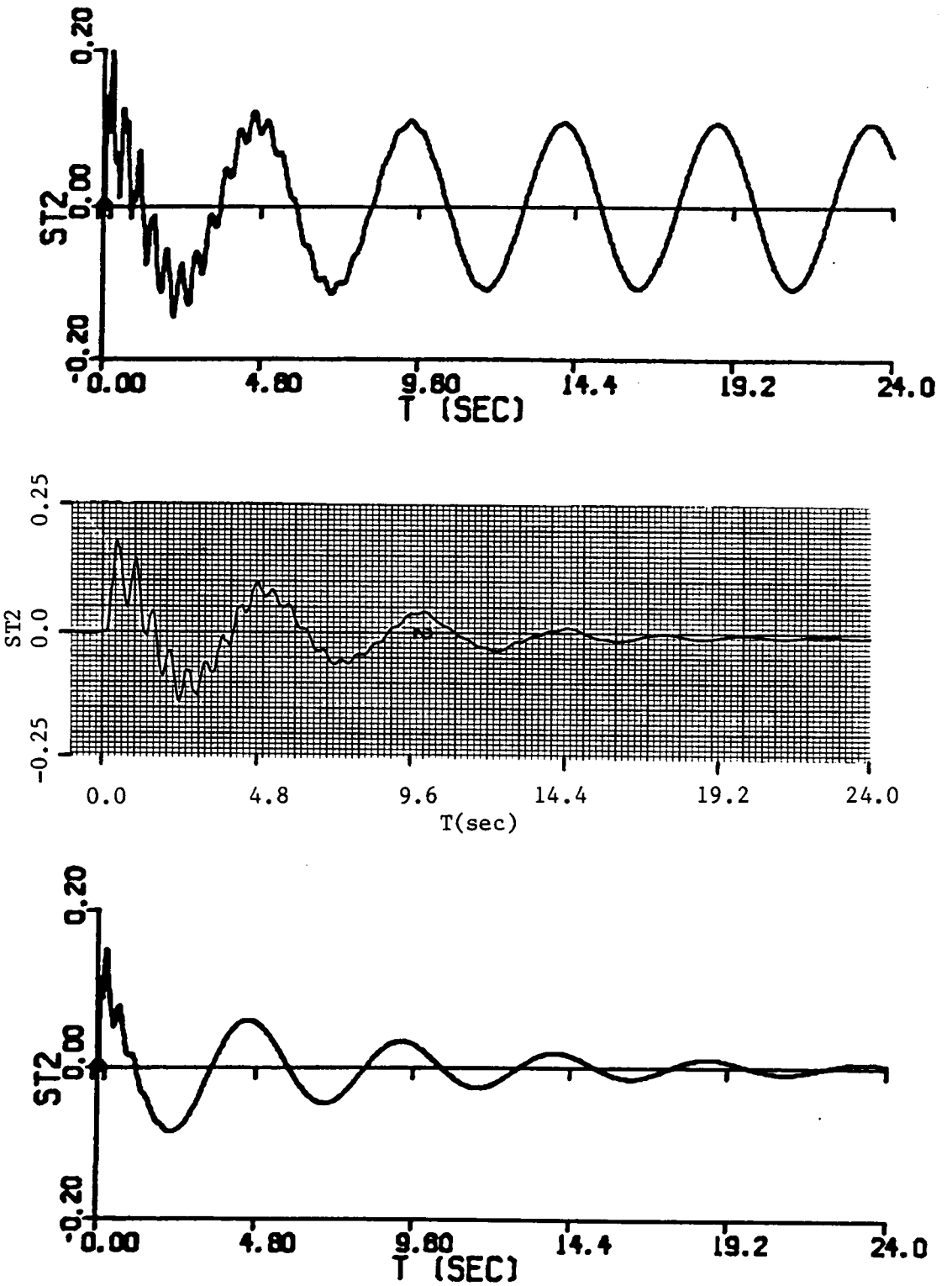

Fig. 6.6 Comparison of Experimental Data and Simulated Data Before and After Damping was Added to Model for System with Angular Position Feedback Subject to 45° Initial Displacement (units in volts)

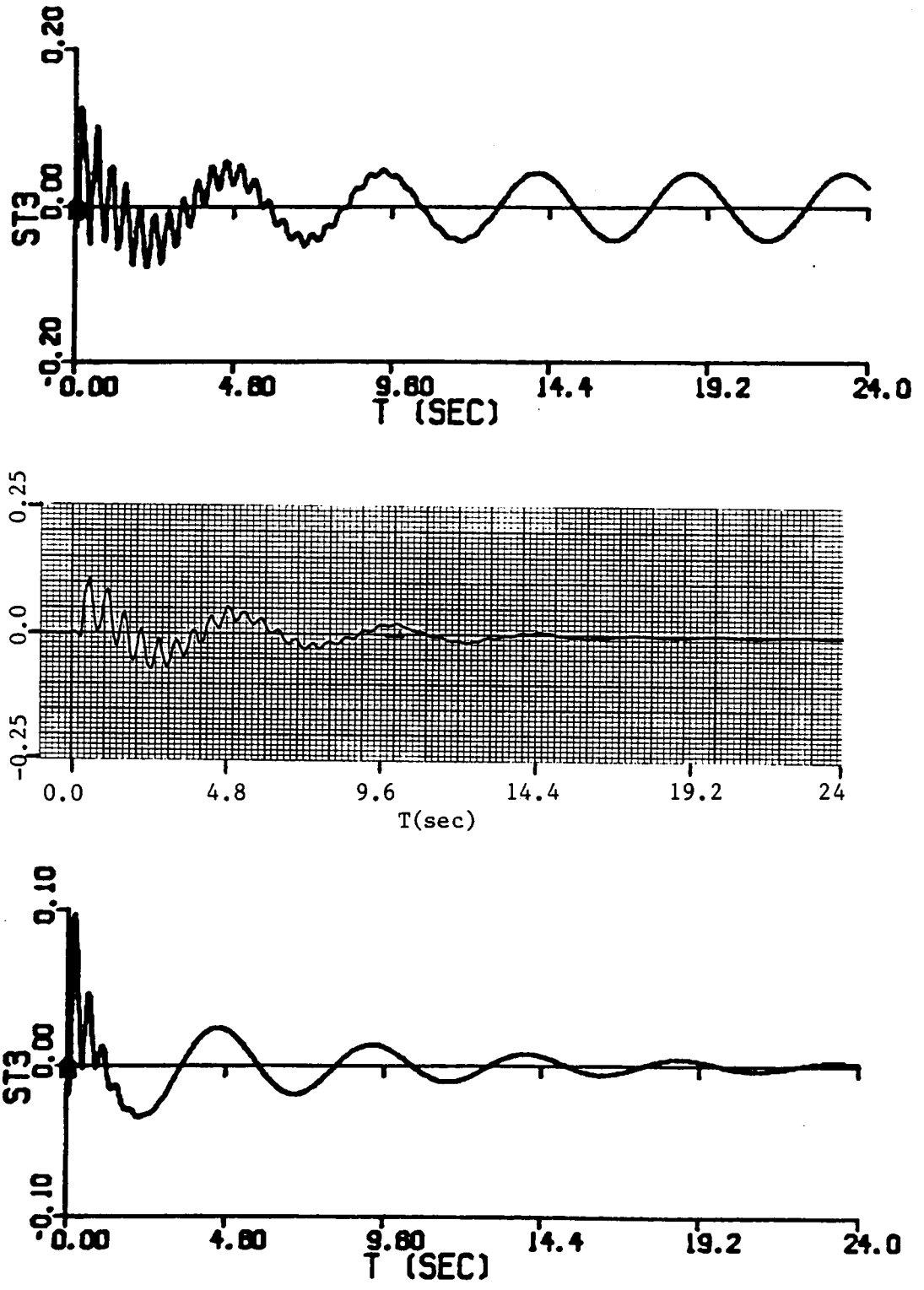

Fig. 6.7 Comparison of Experimental Data and Simulated Data Before and After Damping was Added to Model for System with Angular Position Feedback Subject to 45° Initial Displacement (units in volts)

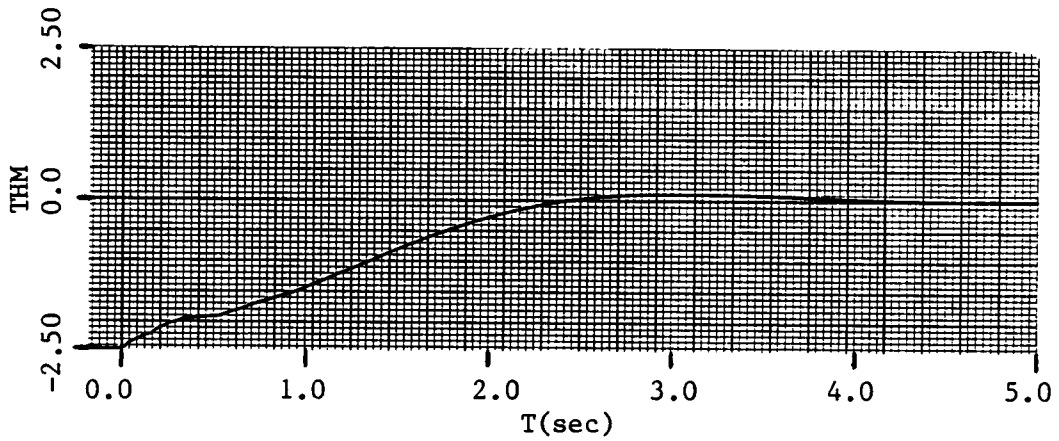

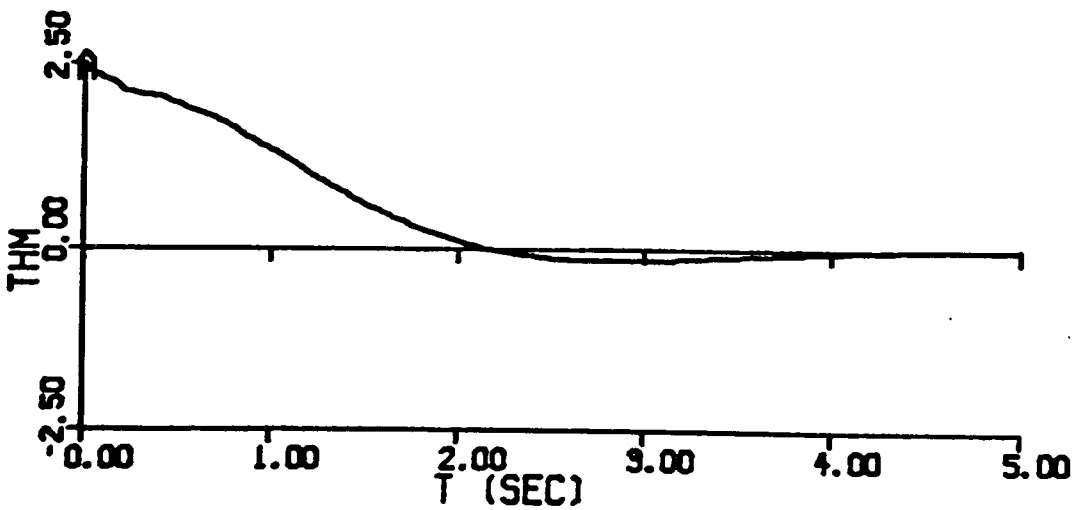

Fig. 6.8 Comparison of Experimental Data & Simulated Data for System with Angular Position and Velocity Feedback Subject to 45° Initial Displacement (units in volts)

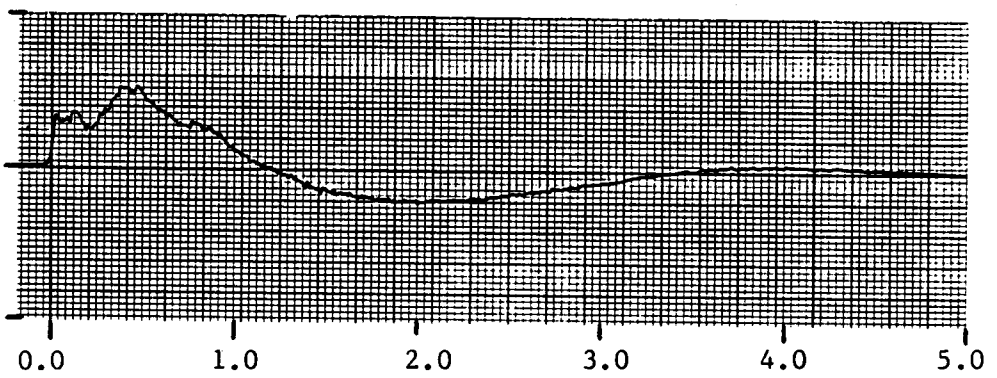

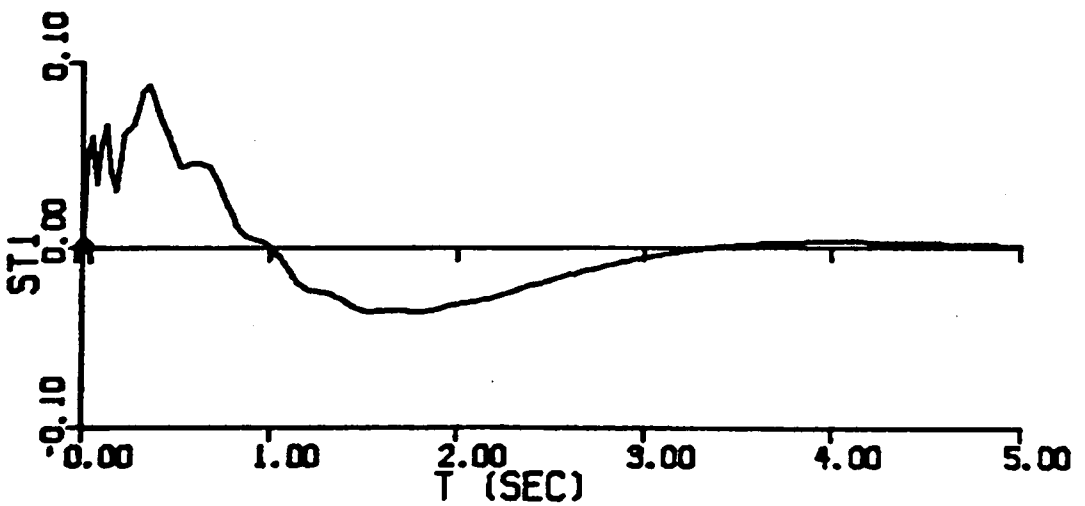

Fig. 6.9 Comparison of Experimental Data & Simulated Data for System with Angular Position and Velocity Feedback Subject to 45^{o} Initial Displacement (units in volts)

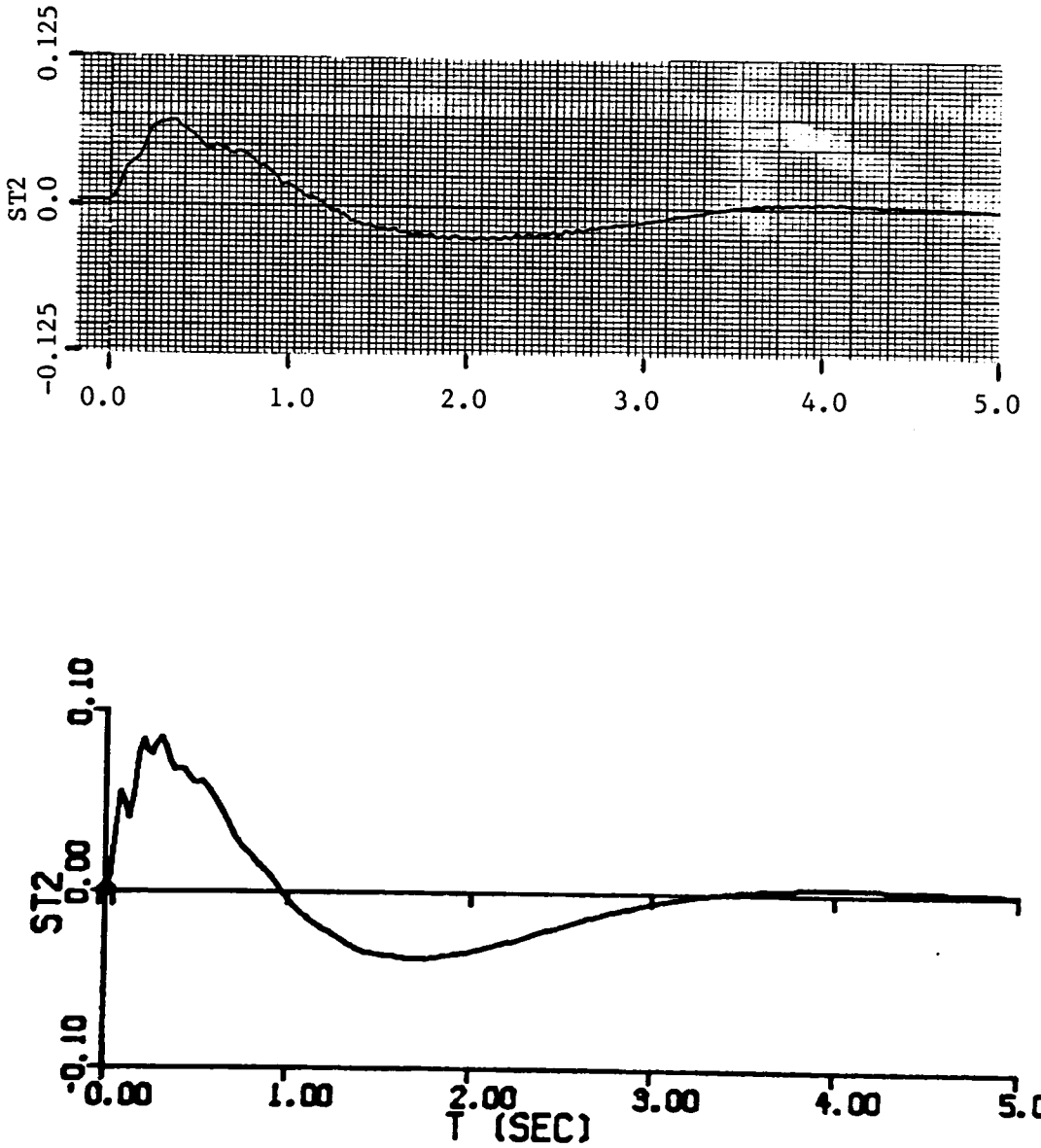

Fig. 6.10 Comparison of Experimental & Simulated Data for System with Angular Position and Velocity Feedback Subject to 45° Initial Displacement (units in volts)

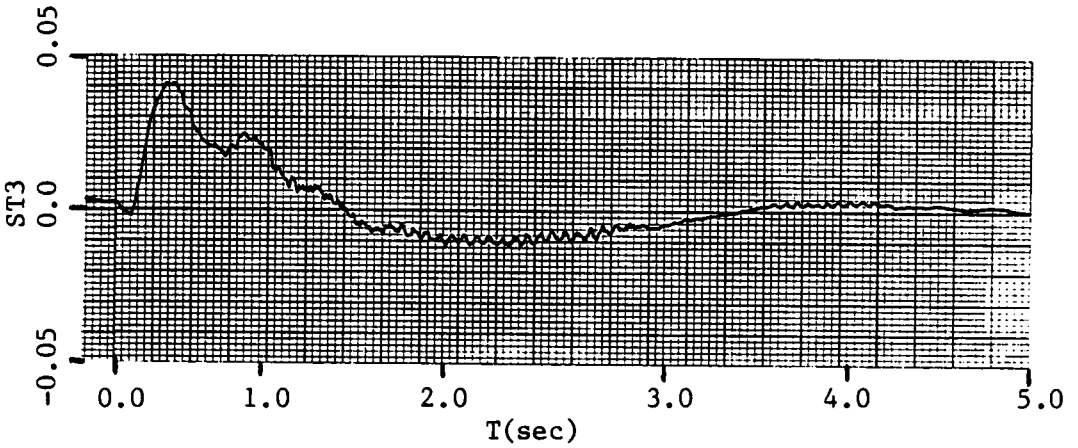

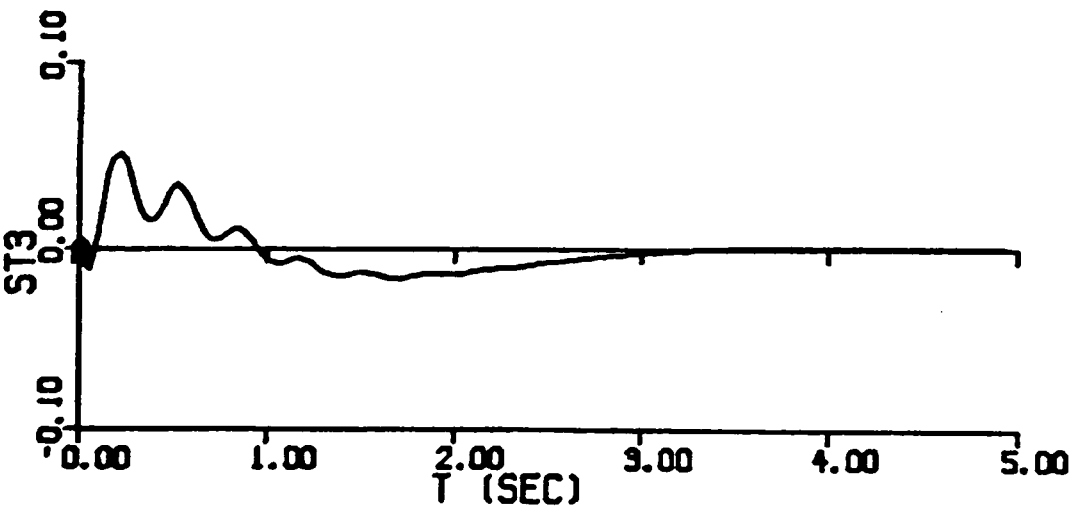

Fig. 6.11 Comparison of Experimental Data & Simulated Data for System with Angular Position and Velocity Feedback Subject to 45° Initial Displacement (units in volts)

Chapter 7

ANALYTICAL RESULTS

In this chapter, results are summarized for the analytical studies of the closed-loop systems. Recall from Chapter 4 that the gain iteration algorithm yields two solutions: a minimum gain norm solution and a minimum sensitivity norm solution. Gain solutions are compared based on sensitivity and torque-requirement considerations. General Sensitivity relationships are also developed. Results are presented separately for the example system and the experimental system to reinforce conclusions. As emphasized throughout this thesis, the two systems are identical in all respects except for motor type. The motor in the example system is voltage-controlled and the motor in the experimental system is torque controlled. As pointed out in Chapter 5, the only difference in system models is the disappearance of a back EMF term in the torque-controlled model. Hence, a comparison of the separate results of the two system models will also give more information on the effects of back EMF on system response.

Example System

Recall from Chapter 4 that the constraints imposed on the system the form

$$\text{Real } (\lambda_i) < -b \tag{7.1}$$

This constraint forces all system dynamics to decay within the envelope e^{-bt}; in other words, it can force the speed of the response to be "fast."

To help gain an understanding of the relationship between gain norms, sensitivity norms and speed of response, several gains sets were calculated for minimum gain norm solutions over the range of eigenvalue constraints

$$0 > \text{Real}\ (\lambda_i) > -3.5 \tag{7.2}$$

For each constraint considered in that range, a gain norm, a sensitivity norm and a sensitivity matrix were calculated.

The gain norm has the form

$$||G|| = \sum_i |G_i| \tag{7.3}$$

and the sensitivity norm is simply the stated system performance index,

$$||PI|| = \sum_i \sum_j \left(\frac{G_i}{\lambda_i} \cdot \frac{\partial \lambda_i}{\partial G_i}\right)^2 \tag{7.4}$$

The sensitivity matrix is constructed so that each element shows the sensitivity of a particular eigenvalue to a particular gain variance. That is

$$[\text{sensitivity}]_{i,j} = \frac{G_i}{\lambda_j} \cdot \frac{\partial \lambda_j}{\partial G_i} \tag{7.5}$$

Clearly, the sum of the square of each matrix element is the same number represented in the PI.

Two graphs show the relationships found between gain norms, sensitivity norms and eigenvalue positions. Figure 7.1 shows a graph of gain norm vs. eigenvalue constraint position. Constraint position is defined

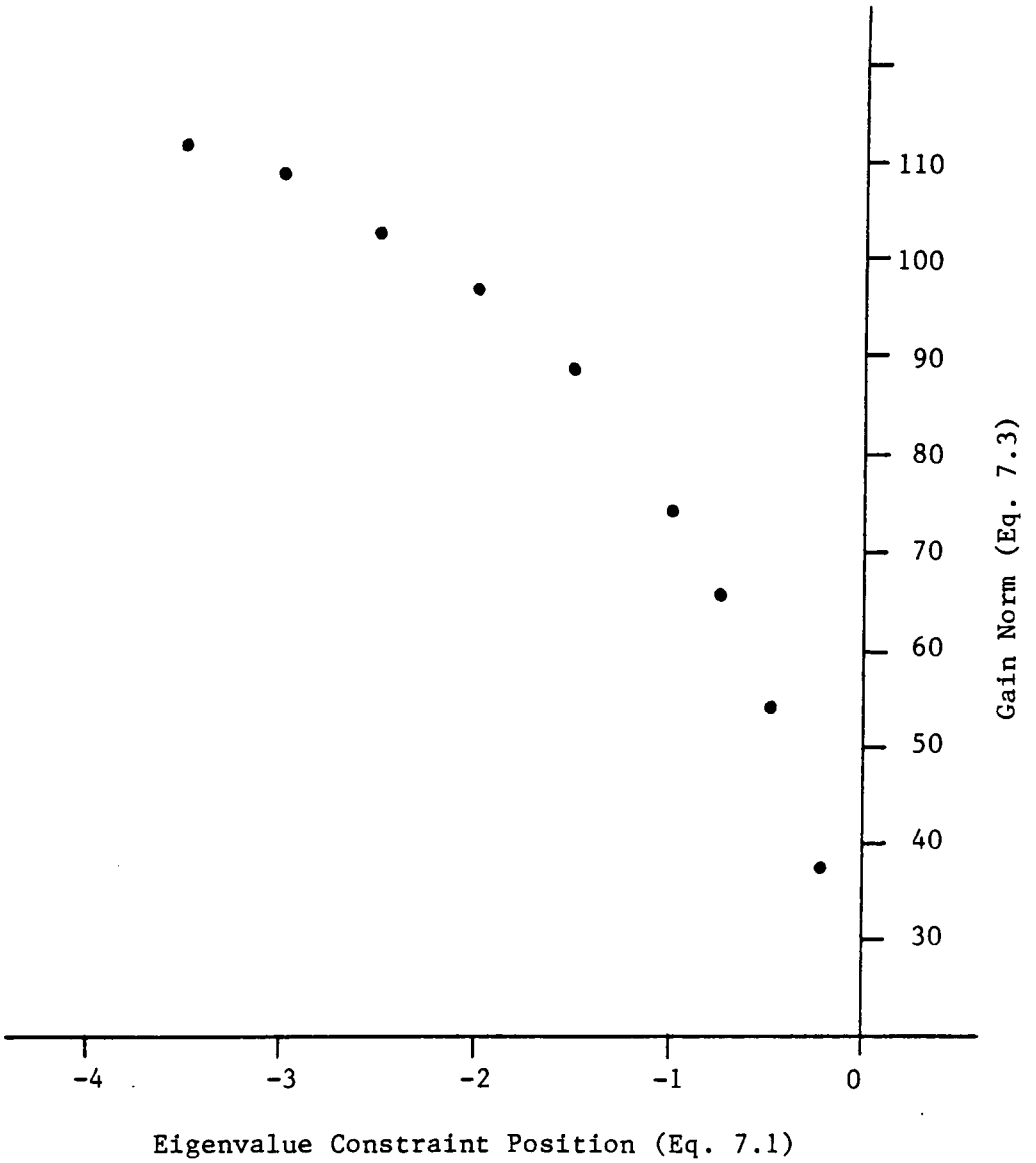

Fig. 7.1 Gain Norm vs Eigenvalue Position for Minimum Gain Solution of Example System

by Eq. 7.1. As seen, gain norm grows convexly (wrong word) as eigenvalues are moved further into the left side of the s-plane. In contrast, Fig. 7.2 shows a graph of sensitivity norm vs. eigenvalue constraint position. Here, system sensitivity grows exponentially as eigenvalues are pushed to the left. Thus arises an important consideration; there appears to be a significant tradeoff in a minimum gain solution between speed of response and system sensitivity.

With this in mind, a minimum sensitivity norm is of obvious interest. Because of lengthy execution time (2-3 hours) and expensive computation time, a minimum sensitivity norm solution is considered for only one constraint set; that is

$$R_e(\lambda_i) < -2.5 \tag{7.6}$$

This was chosen since it represents a relatively fast response that appears physically realizable.

The value of the PI in the minimum gain norm solution is 280. The minimum sensitivity norm algorithm reduces this number a significant 72% to 110. Table 7.1 shows side-by-side listings of the gain sets calculated by the minimum gain norm solution and minimum sensitivity norm for the constraint set of Eq. 7.6. Note the gain norm for the minimum sensitivity solution rose 13% over the minimum gain norm solution.

Table 7.2 shows side-by-side listing of the final eigenvalue positions of the two solutions. Note that since there are no constraints on the imaginary parts of the eigenvalues it is quite possible for them to change dramatically. Here, however, they remain close. Since eigen-

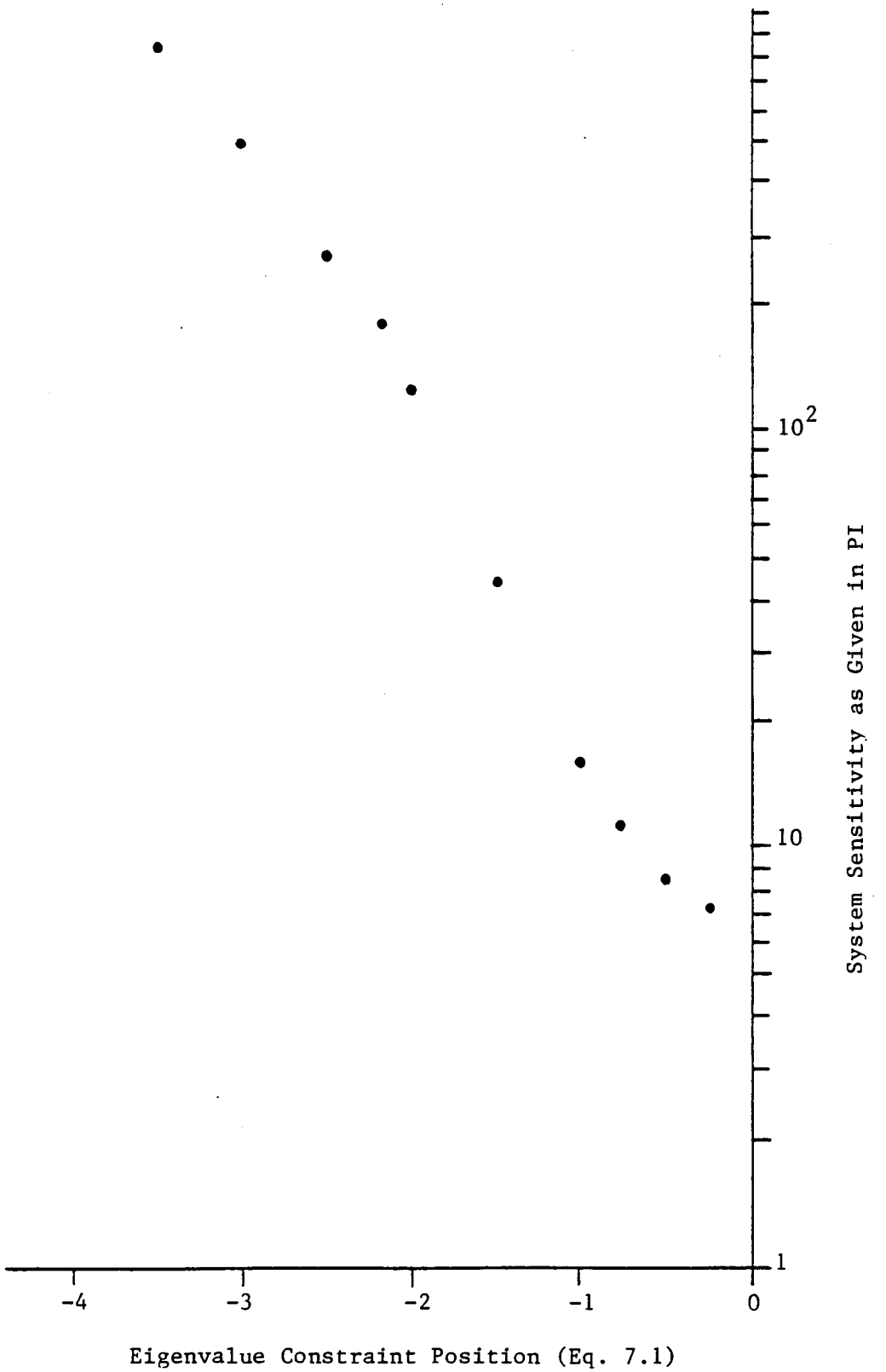

Fig. 7.2 System Sensitivity vs Eigenvalue Positions for Minimum Gain Solution of Example System

Table 7.1 Gain Solutions for Example System

Gain	min. gain norm solution	min. sens. norm solution
G_{sys}	28.31	30.23
G_{th}	1.749	1.805
G_{st1}	-1.634	3.423
G_{st2}	-7.726	-15.30
G_{st3}	7.387	13.67
G_{th}	-2.092	-0.8265
G_{st2}	14.82	18.63
G_{st3}	24.34	17.93
G_{esth}	4.366	4.977
G_{est2}	6.417	5.309
G_{est3}	4.380	4.885

Table 7.2 Eigenvalues for Example System Solutions

	Eigenvalues	
	min. gain norm solution	min. sens. norm solution
Model	-2.50 ± i 55.4	-2.50 ± i 55.1
	-2.50 ± i 14.3	-2.51 ± i 15.5
	-2.50 ± i 3.34	-2.50 ± i 3.37
	-2.50 ± i 0.0	-2.49 ± i 0.0
	-3723. ± i 0.0	-3722. ± i 0.0
Estimators	-40.1 + i 0.0	-38.5 + i 0.0
	-45.1 + i 0.0	-46.3 + i 0.0
	-49.7 + i 0.0	-50.1 + i 0.0

values completely describe response characteristics, there is clearly no appreciative change in system response for these two solutions.

The sensitivity matrices mentioned earlier are shown for the minimum gain norm solution in Table 7.3 and for the minimum sensitivity norm solution in Table 7.4. Recall that each matrix element approximates the anticipated percent change in an eigenvalue for a unit percent variance in a gain. Consider for example a +1% change in G_{SYS} in Table 7.3. The anticipated effect on system eigenvalues is represented by the row of G_{01}. Consider the same +1% change in G_{SYS} in Table 7.4. Note that the anticipated changes are considerably smaller for the minimum sensitivity norm solution. This is demonstrated in Table 7.5 by a side-by-side comparison of the actual change in eigenvalues for a +1% change in G_{01}. As discussed, the minimum sensitivity solution is more robust to this type of perturbation. Upon close inspection, the actual change in eigenvalues is not in exact accord with the anticipated changes. This is expected though since the PI is only a first order approximation to system sensitivity. Clearly, higher order effects are present but the matrix elements (PI) are still good approximations.

The two solutions are now looked at in response simulation. These were conducted with the help of ACSL (Advanced Computer Simulation Language). Two tests are considered: impulse loading (initial velocity conditions) which excites all vibration modes and a large angle (45^{o}) slewing maneuver which starts from rest.

First, the uncontrolled, open-loop beam response to the impulse load is shown for the three strain gage outputs in Fig. 7.3. As an interesting aside, note that no second mode vibration is detected by

Table 7.3 Normalized Eigenvalue (Re(λi)) Sensitivities for Minimum Gain Norm Solution to Example System

	-2.50±i155.42	-2.50±i14.3	-2.50±i3.34	-2.50+i0.0	-3722+i0.0
G_{sys}	0.914	-0.822	2.70	5.34	0.00000
G_{th}	-0.0335	-0.477	-0.399	2.59	-0.00032
G_{ST1}	0.0434	-0.0348	0.122	0.228	-0.00023
G_{ST2}	-0.245	-0.622	0.539	1.10	-0.00013
G_{ST3}	-0.0215	0.562	-0.164	-0.406	-0.00017
$G_{\dot{th}}$	0.168	0.157	0.468	0.821	0.000170
$G_{\dot{ST2}}$	1.31	0.155	1.28	0.551	0.00158
$G_{\dot{ST3}}$	-0.309	-0.561	0.855	0.355	-0.00243
G_{esth}	0.0969	-0.259	-0.0716	-0.0499	0.00172
G_{est2}	-0.240	-0.397	1-0.0657	-0.0223	0.00160
G_{est3}	-0.184	-0.950	-0.0679	-0.0215	-0.00246

	-40.1+i0.0	45.1+i0.0	-49.7+i0.0	
G_{sys}		-0.288	0.0521	-0.360
G_{th}		-0.00876	0.00141	-0.00886
G_{ST1}		-0.00434	0.00073	-0.00474
G_{ST2}		-0.00818	0.00126	-0.00759
G_{ST3}		-0.00268	0.00048	-0.00326
$G_{\dot{th}}$		-0.513	-0.239	0.383
$G_{\dot{ST2}}$		-0.168	0.0366	-0.320
$G_{\dot{ST3}}$		0.417	0.251	-0.398
G_{esth}		5.75	-7.75	3.16
G_{est2}		0.279	-0.0862	1.10
G_{est3}		-4.50	9.02	-3.37

Table 7.4 Normalized Eigenvalue (Re(λi)) Sensitivities for Minimum Sensitivity Norm Solution to Example System

	-2.50±i55.1	-2.51±i15.5	-2.50±i3.37	-2.49+i0.0	-3722+i0.0
G_{sys}	0.954	0.0425	2.53	4.69	-0.00001
G_{th}	-0.0405	-0.405	-0.360	2.56	-0.00035
G_{ST1}	-0.0949	-0.00266	-0.259	-0.457	0.00051
G_{ST2}	-0.532	-1.01	1.09	2.09	-0.00027
G_{ST3}	-0.0469	1.07	-0.315	-0.720	-0.00033
$G_{\dot{th}}$	0.0819	0.0953	0.181	0.308	0.00082
$G_{\dot{ST2}}$	1.87	0.598	1.58	0.665	0.00175
$G_{\dot{ST3}}$	-0.279	-0.296	0.611	0.248	-0.00213
G_{esth}	0.0374	-0.0822	-0.0236	-0.0162	0.00083
G_{est2}	0.0693	-0.525	-0.0934	-0.328	0.00177
G_{est3}	-0.139	-0.731	-0.0426	-0.0133	-0.00216

	-38.5+i0.0	-46.3+i0.0	-50.1+i0.0
G_{sys}	-0.842	0.0680	-0.00096
G_{th}	-0.0294	0.00198	-0.00003
G_{ST1}	0.0291	-0.00209	0.00003
G_{ST2}	-0.0534	0.00335	-0.00004
G_{ST3}	-0.0154	0.00124	-0.00002
$G_{\dot{th}}$	-0.228	0.0603	0.00798
$G_{\dot{ST2}}$	-0.909	0.148	-0.00462
$G_{\dot{ST3}}$	0.365	-0.145	-0.00426
G_{esth}	0.778	-0.806	1.09
G_{est2}	2.39	-1.01	0.0785
G_{est3}	-1.36	2.63	-0.166

Table 7.5 Comparison of Eigenvalue Position Robustness to Small Gain Changes for Minimum Sensitivity Norm and Minimum Gain Norm Solutions (example system)

eigenvalues min. gain norm solution	eigenvalues +1% change in G_{sys}	% change in Re (λ_i)	eigenvalues min. sens. norm solution	eigenvalues +1% change in G_{sys}	% change in Re (λ_i)
-2.50 ± i 55.4	-2.52 ± i 55.4	0.8	-2.50 ± i 55.1	-2.52 ± i 55.0	0.8
-2.50 ± i 14.3	-2.48 ± i 3.34	2.8	-2.51 ± i 15.5	-2.51 ± i 15.3	0.0
-2.50 ± i 3.34	-2.57 ± i 3.24	2.8	-2.50 ± i 3.37	-2.56 ± i 3.28	2.4
-2.50 + i 0.0	-2.64 + i 0.0	5.6	-2.49 + i 0.0	-2.62 + i 0.0	5.2
-3723.+ i 0.0	-3722.+ i 0.0	0.0	-3722.+ i 0.0	-3722.+ i 0.0	0.0
-40.1 + i 0.0	-40.0 + i 0.0	-0.25	-38.5 + i 0.0	-38.2 + i 0.0	-0.78
-45.1 + i 0.0	-45.1 + i 0.0	0.0	-46.3 + i 0.0	-46.3 + i 0.0	0.0
-49.7 + i 0.0	-49.5 + i 0.0	0.4	-50.1 + i 0.0	-50.1 + i 0.0	0.0

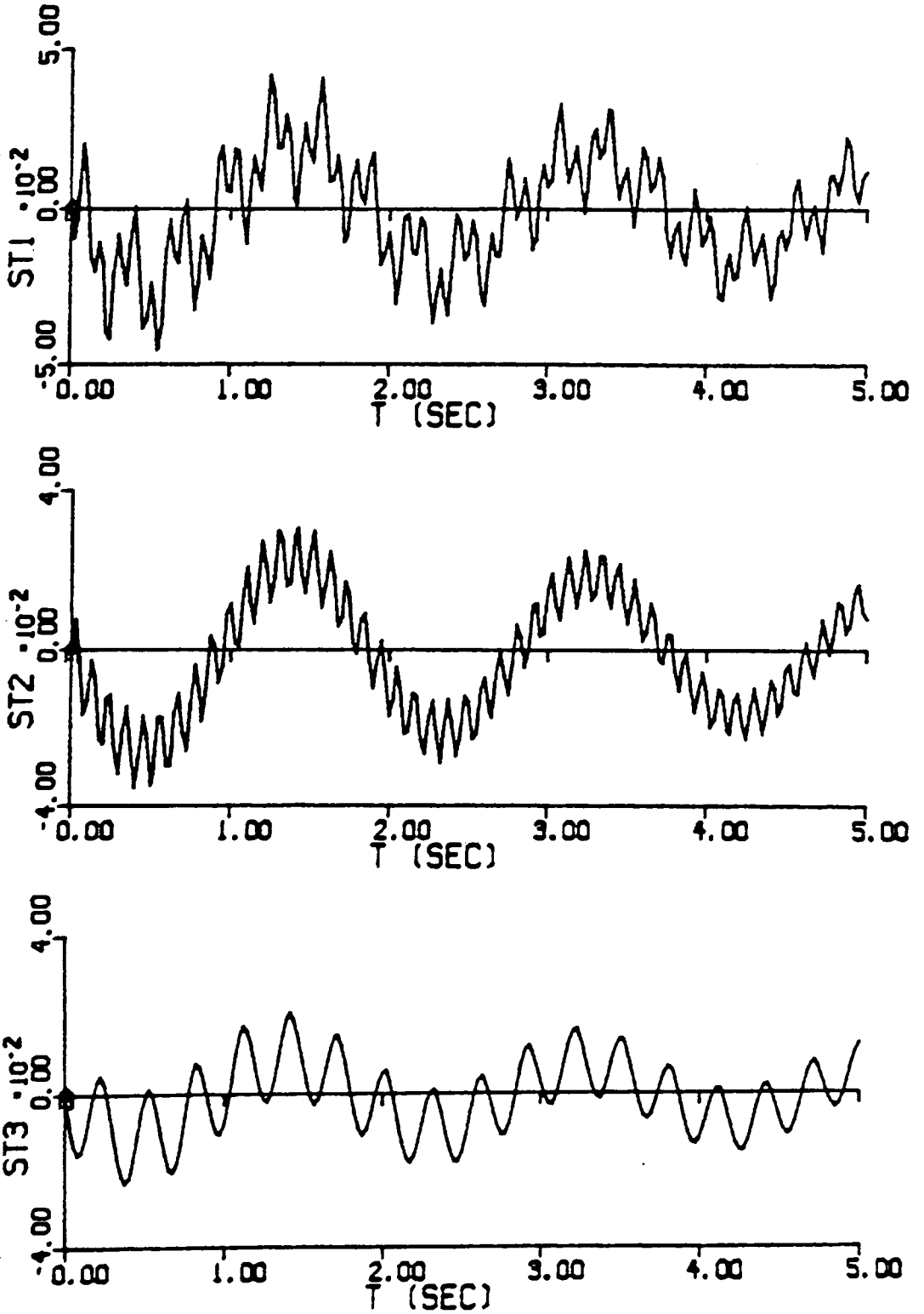

Fig. 7.3 Open-Loop Response of Example System to an Impulse Force (units in volts)

strain gage 2 and that no third mode vibration is detected by strain gage 3. Recalling from Chapter 5, in a system such as the one with a large back EMF, the vibration modes of the beam/motor approach those of a clamped-free beam. Recall also from Chapter 2 that the positions of the second and third strain gages were carefully chosen so that they coincided with nodes in the second and third vibration mode shapes respectively. Since these mode shapes are based on a cantilevered beam, these simulation results show characteristics exactly as expected.

The closed loop response for the minimum gain norm solution to the same impulse is shown in Fig. 7.4 and Fig. 7.5. Strain gage output is shown in Fig. 7.4. Figure 7.5 shows angular position of the beam and input torque requirements. Similar results are shown in Fig. 7.6 and Fig. 7.7 for the minimum sensitivity norm solution. Notice that as anticipated the responses of the two solutions are very similar. It is particularly important to note that there are no significant differences in input torque requirements between the solutions.

Next, the responses of these solutions are simulated for 45^{o} slewing maneuver that starts from the system at rest. The simulations of the minimum gain norm solution are shown in Fig. 7.8 and Fig. 7.9. The simulations of the minimum sensitivity solutions are shown in Fig. 7.10 and Fig. 7.11. Notice as before, the similarity in dynamic responses and in torque requirements. Also notice that in all cases shown, position and vibration control are achieved in the same amount of time. This is caused directly by the uniform eigenvalue constraint of Eq. 7.1.

In summary, a 72% reduction in net system sensitivity has been achieved without altering system response or torque requirements.

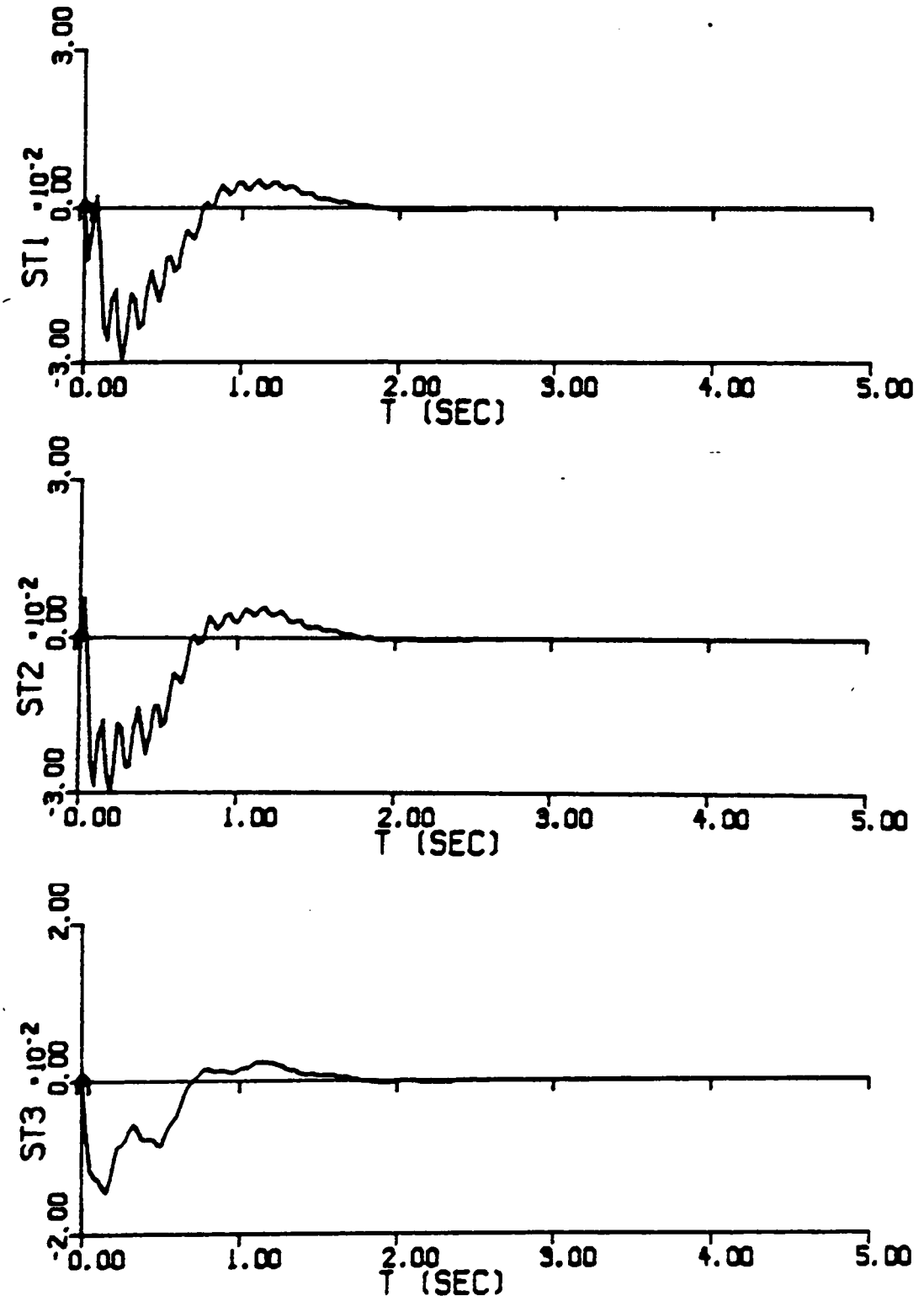

Fig. 7.4 Response to Impulse Force for Minimum Gain Norm Solution of Example System (units in volts)

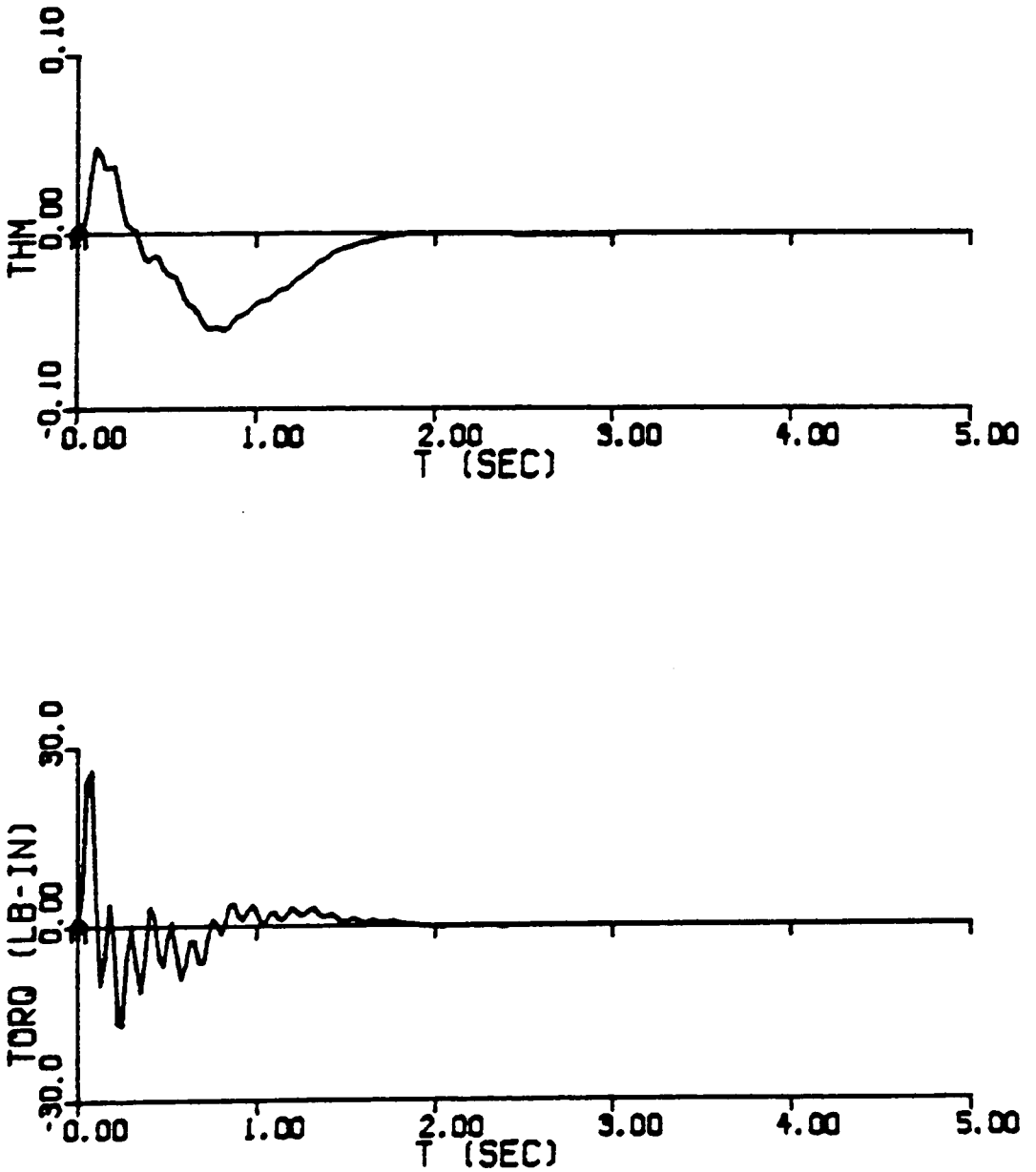

Fig. 7.5 Response to Impulse Force for Minimum Gain Norm Solution of Example System (unspecified units in volts)

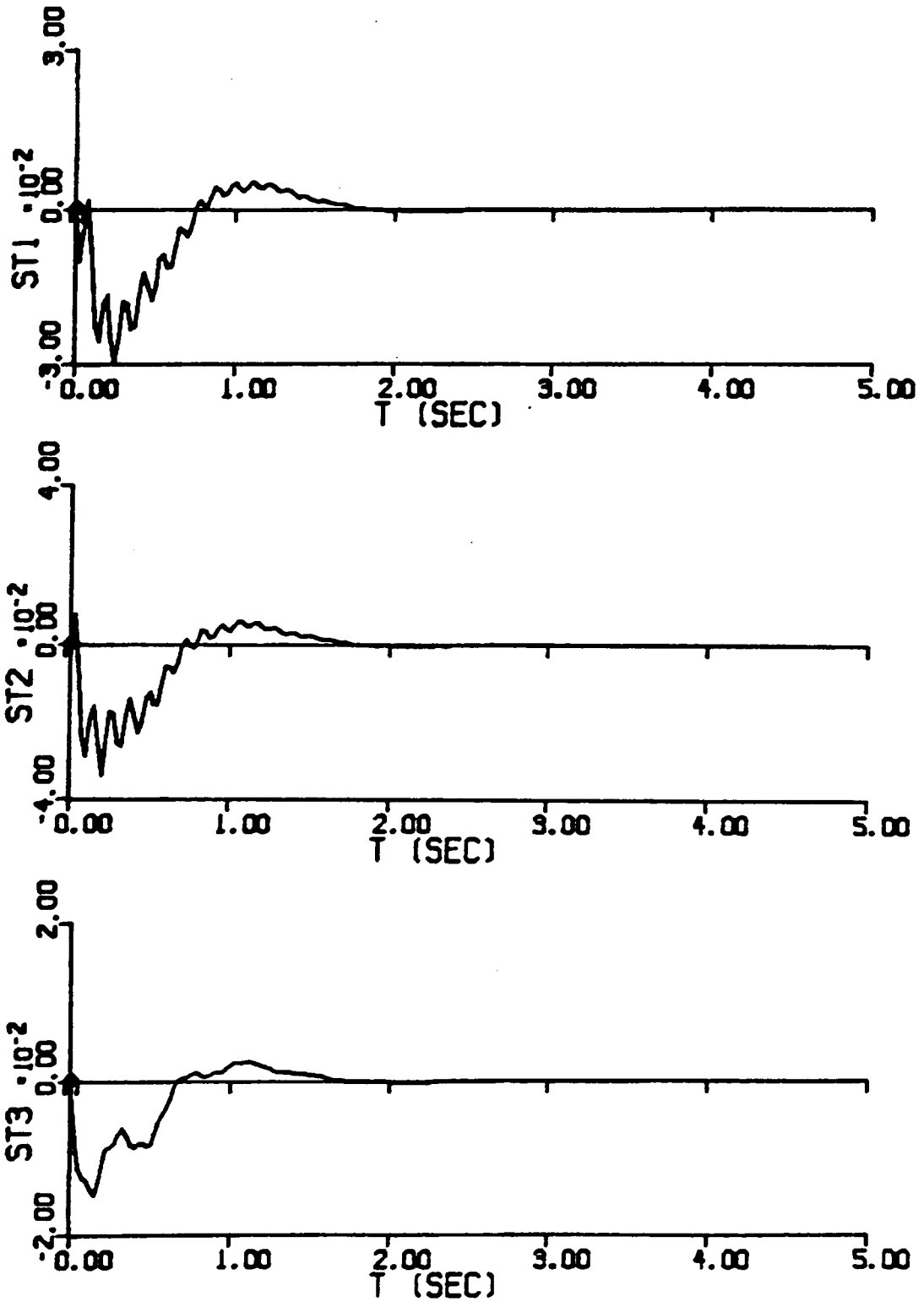

Fig. 7.6 Response to Impulse Force for Minimum Sensitivity Norm Solution of Example System (units in volts)

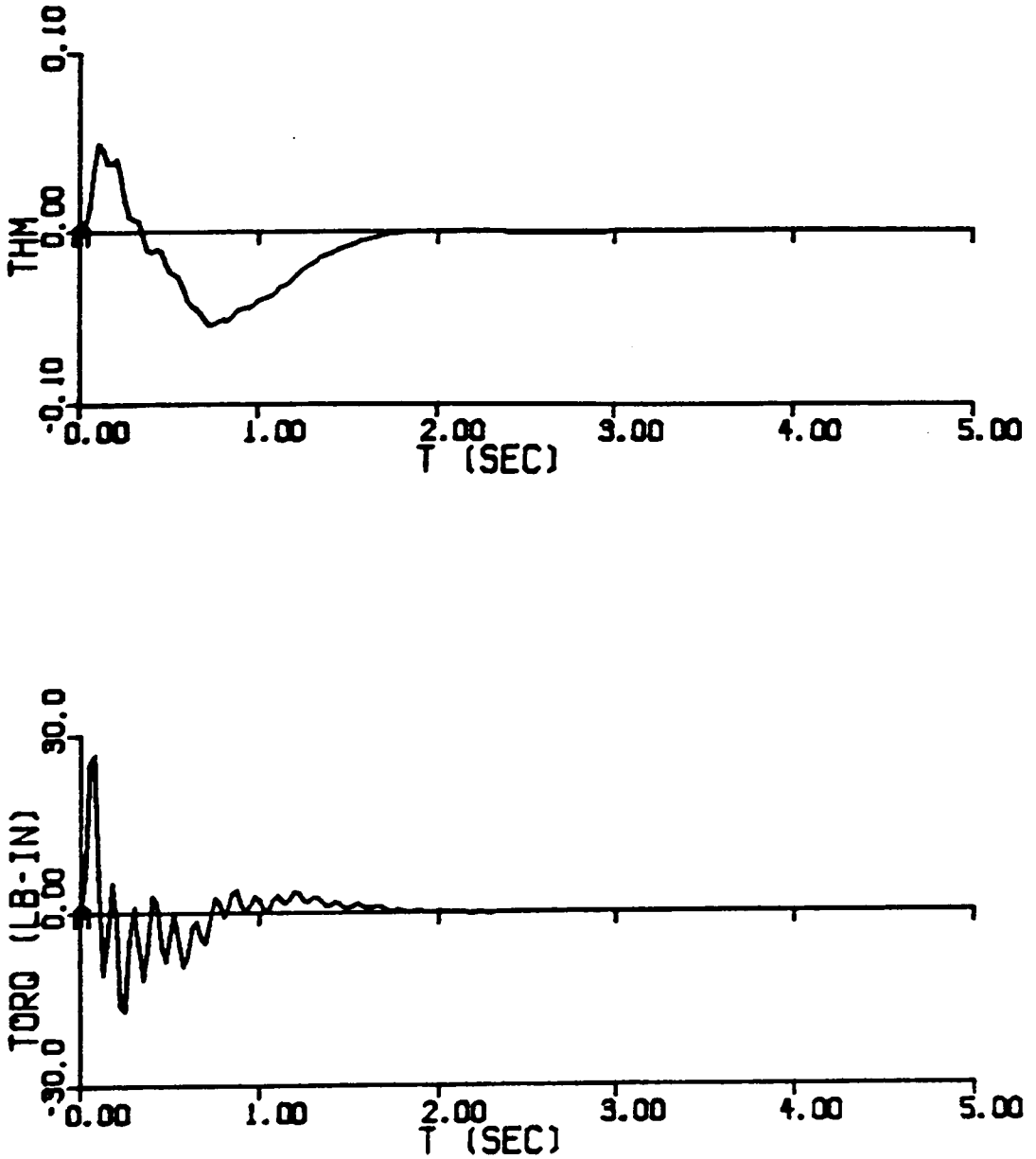

Fig. 7.7 Response to Impulse Force for Minimum Sensitivity Solution of Example System (unspecified units in volts)

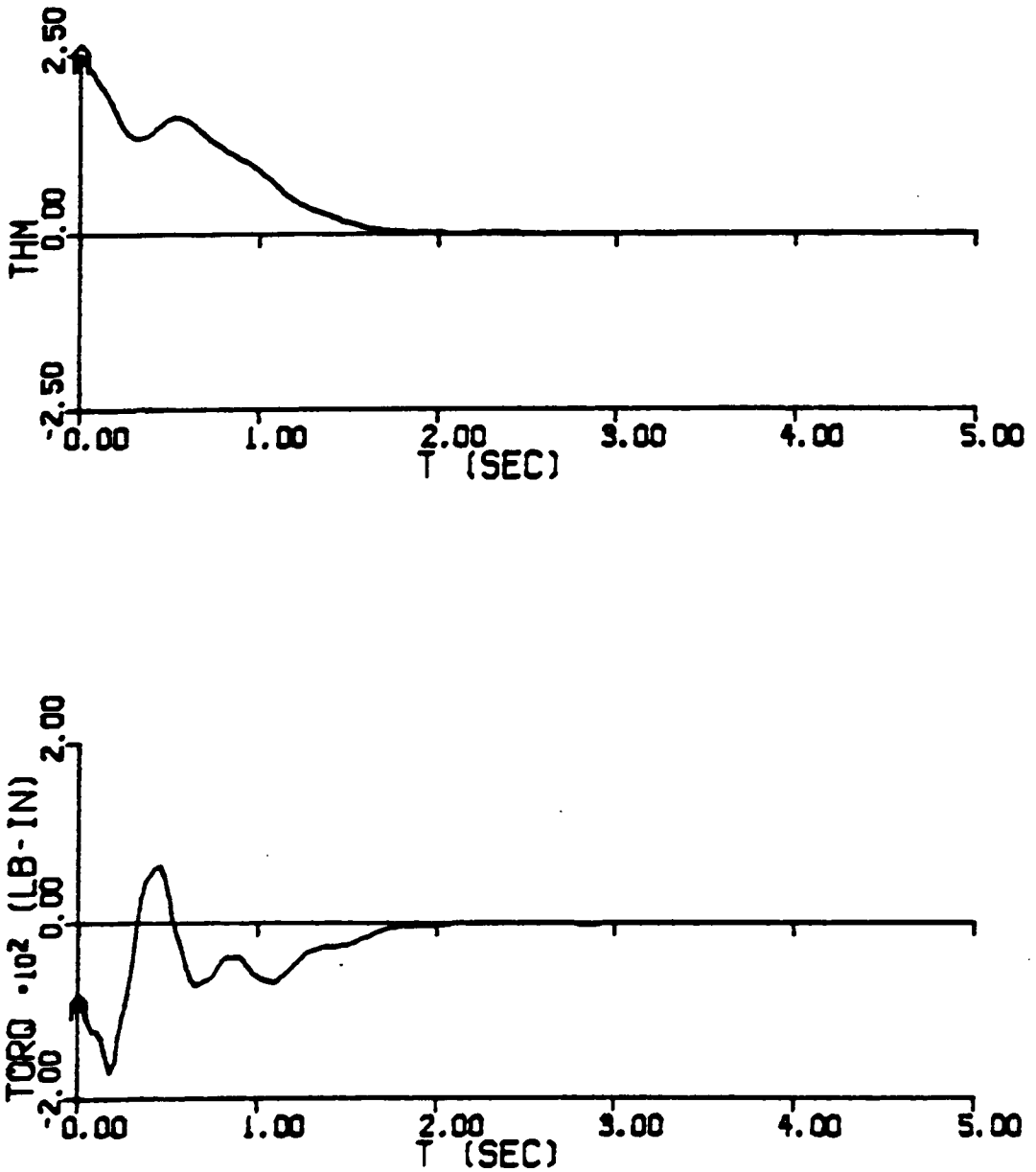

Fig. 7.8 Response to 45° Slewing Maneuver for Minimum Gain Norm Solution of Example System (unspecified units in volts)

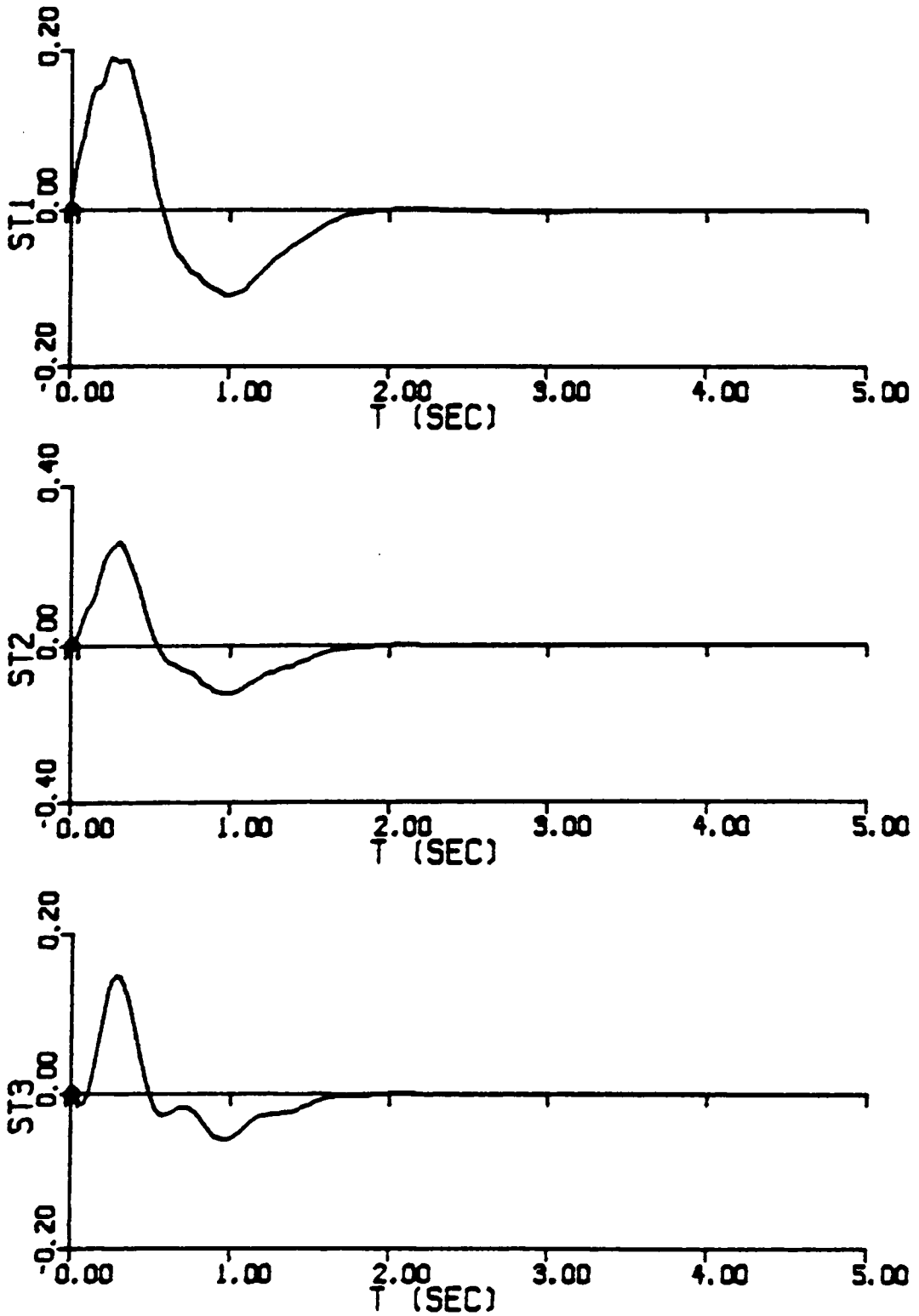

Fig. 7.9 Response to 45° Slewing Maneuver for Minimum Gain Norm Solution of Example System (units in volts)

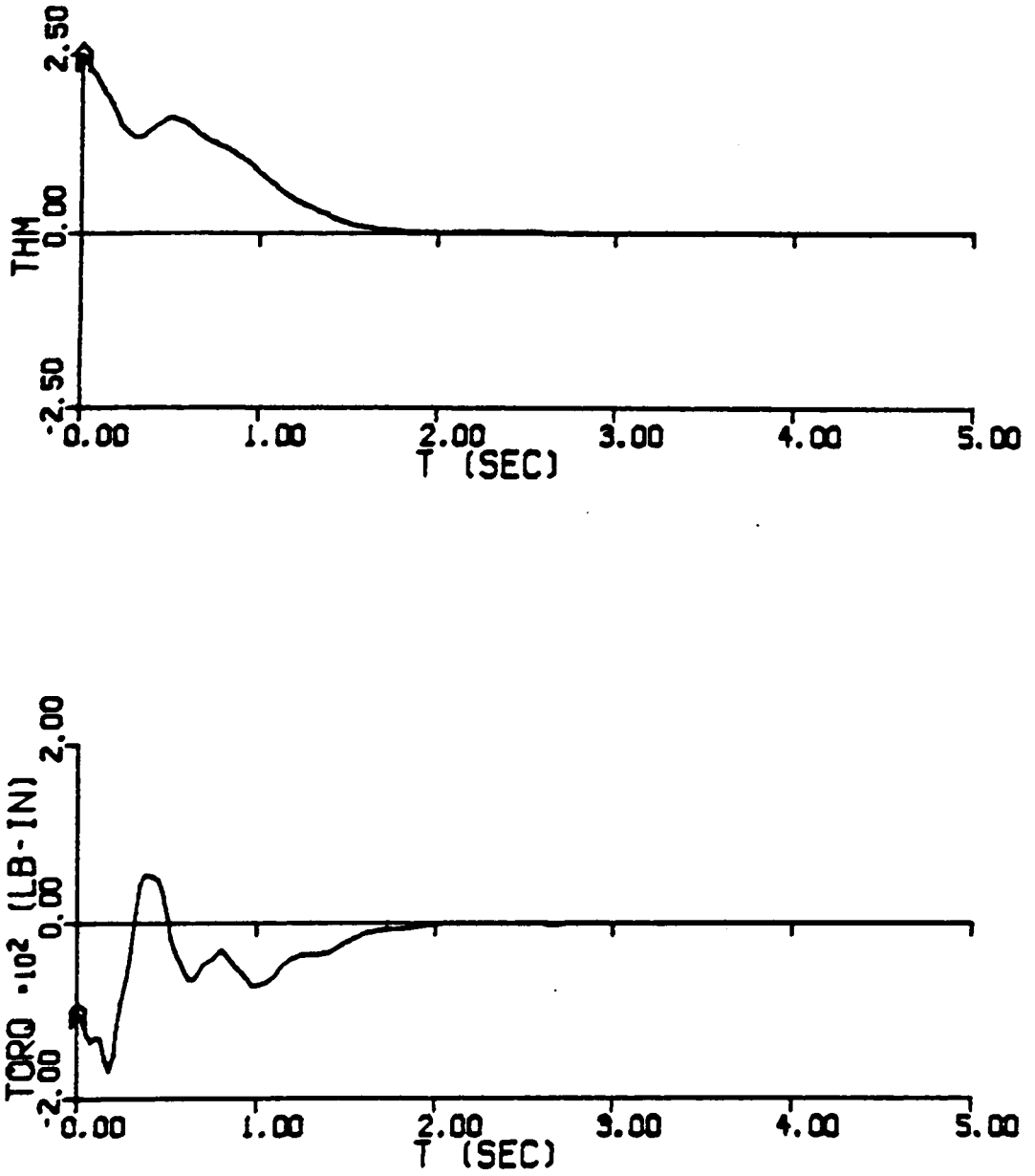

Fig. 7.10 Response to 45° Slewing Maneuver for Minimum Sensitivity Solution of Example System (unspecified units in volts)

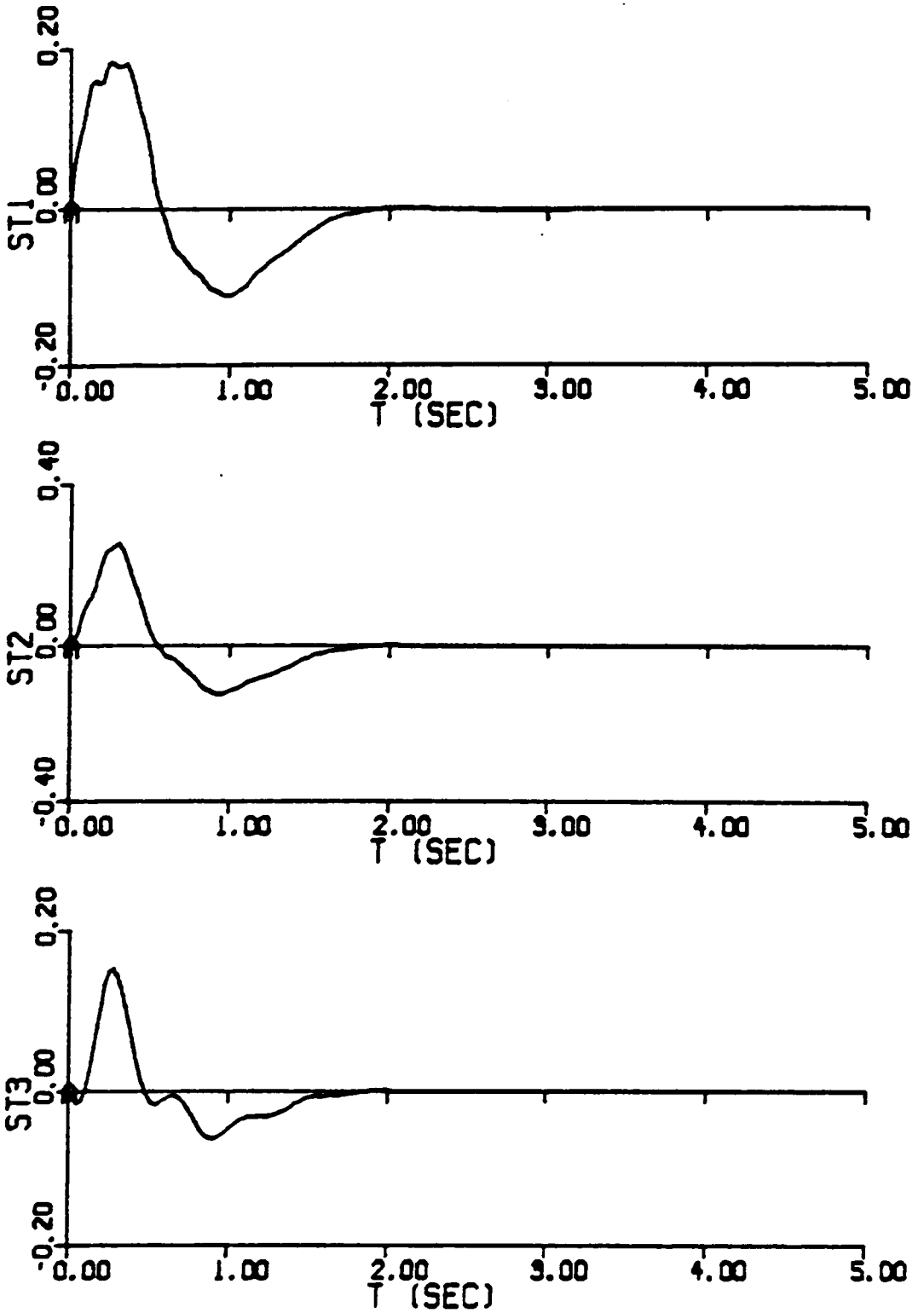

Fig. 7.11 Response to 45° Slewing Maneuver for Minimum Sensitivity Solution of Example System (units in volts)

Clearly, system performance has benefitted from the sensitivity reduction.

Experimental System

Here, the analytical results are presented for the experimental system with the torque-controlled motor. All results are presented in parallel with the discussion of the results for the example system. Comparisons and contrasts are observed between the two systems as well as between the two gain solution types.

As before, minimum gain norm solution sets were calculated over the range of constraints given in Eq. 7.2. Graphs of gain norm vs. eigenvalue placement and of sensitivity vs. eigenvalue placement are shown in Fig. 7.12 and Fig. 7.13 respectively. These graphs are qualitatively similar to those in Fig. 7.1 and Fig. 7.2; convex (wrong word) increase in gain norm and an exponential increase in sensitivity norm are both observed as eigenvalues are moved to the left. Note, however that the magnitude relationships of these norms for the two systems are quite different. The gain norm for the experimental system remains smaller and in a more "dense" range than for the example system. Conversely, the sensitivity norm grows at a steeper rate and is 1-3 orders of magnitude larger in the experimental system. Intuitively, these results make sense: smaller changes in gains would be necessary to meet constraints if the system was more sensitive than the example system.

As before, a minimum sensitivity norm solution is considered for the constraint set given in Eq. 7.6. The value of the system PI with the minimum gain solution is 4210. The minimum sensitivity norm algorithm reduces the PI once again by a significant 72% to 1800.

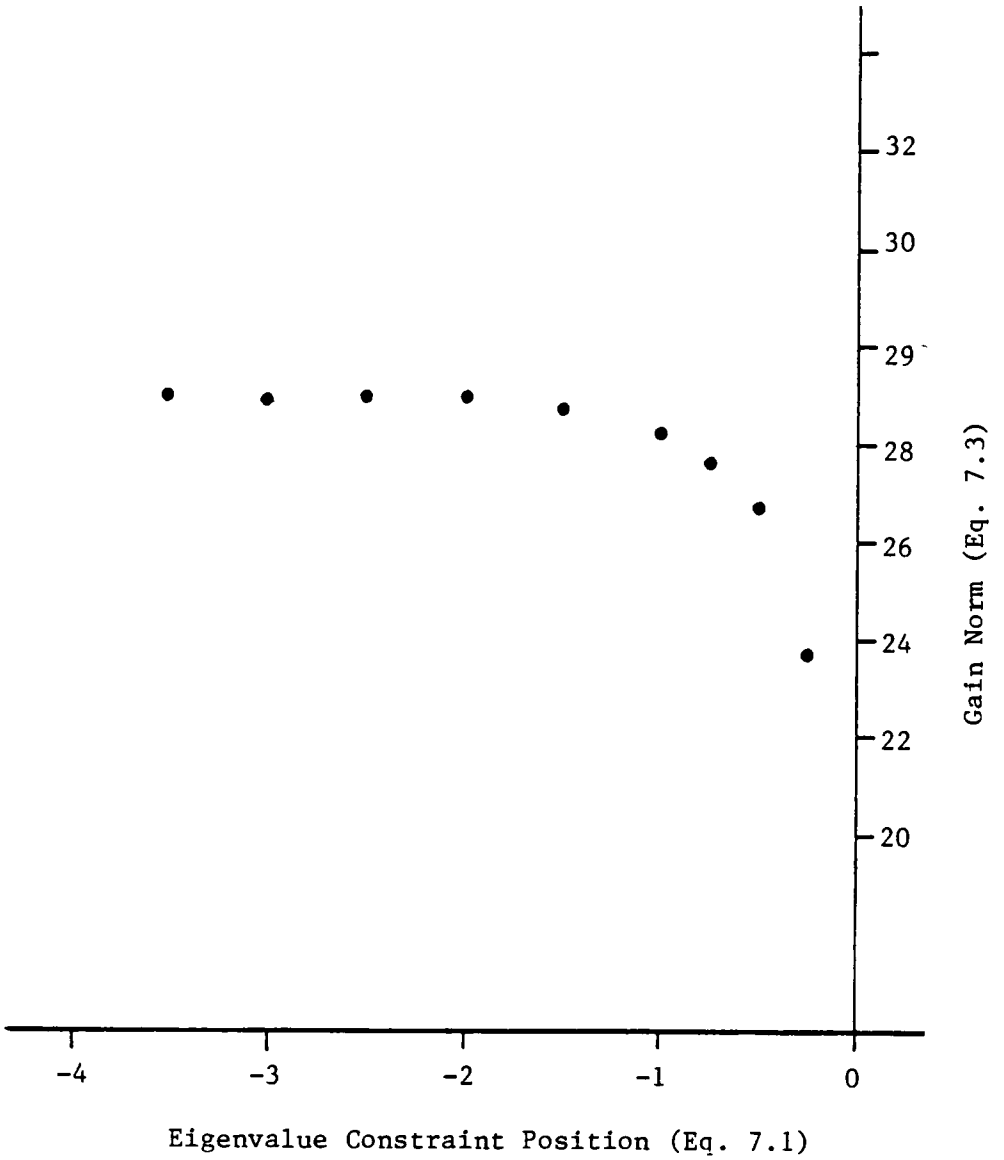

Fig. 7.12 Gain Norm vs Eigenvalue Position for Minimum Gain Solution of Experimental System

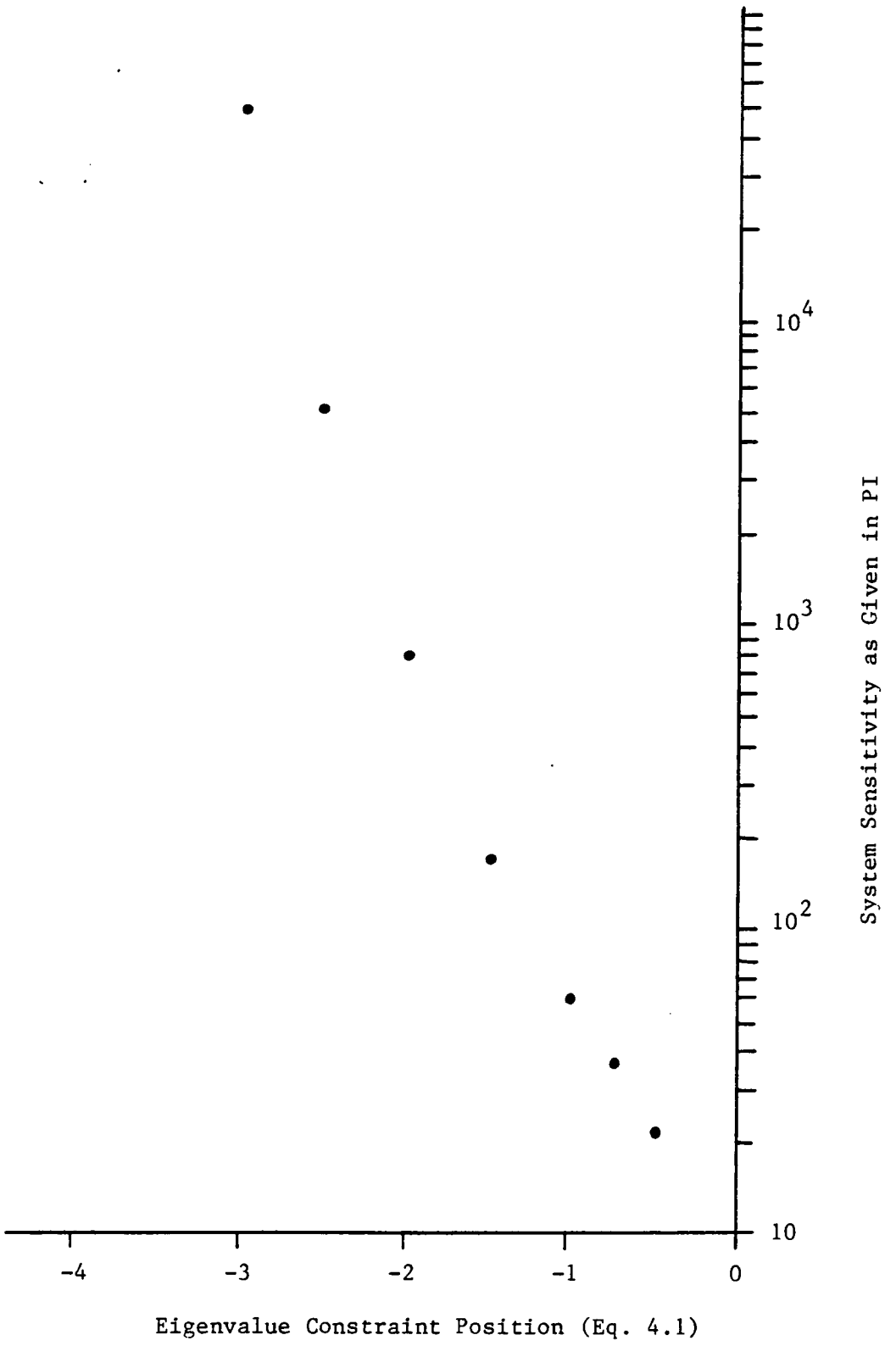

Fig. 7.13 System Sensitivity vs Eigenvalue Positions for Minimum Gain Solution of Experimental System

Table 7.6 shows a side-by-side listing of the calculated gain sets of the two solutions. The sensitivity reduction leads to a 9% increase in gain norm.

Table 7.7 shows the system's eigenvalues. Notice that the imaginary parts of the eigenvalues moved considerably from their original positions. In this case, different system responses can be anticipated for the two solutions.

Sensitivity matrices are shown for the minimum gain solution in Table 7.8 and for the minimum sensitivity solution in Table 7.9. A typical eigenvalue sensitivity is much greater here than in the example system (Tables 7.3 and 7.4). The effectiveness of the sensitivity reduction is still evident though. Table 7.10 compares the robustness of the two solutions to a +1% perturbation in G_{sys}. As seen, with a minimum sensitivity norm-gain set, the system's ability to handle small gain variances is once again improved.

As before, simulations are presented for system response to an impulse load and to a large angle maneuver. The same impulse load is applied to the experimental system. The uncontrolled, open-loop response is shown in Fig. 7.14. Recall from Chapter 5 that the vibration modes of this experimental system are different than those of a clamped-free beam; therefore the significance of the chosen strain locations is lost. As seen, all vibration modes are visible at all strain gage locations.

The closed-loop response for the minimum-gain-norm solution is shown in Fig. 7.15 and Fig. 7.16. In comparison to the results in Fig. 7.6 and Fig. 7.7, system dynamics behave similarity since the enforced

Table 7.6 Gain Solutions for Experimental System

Gain	min. gain norm solution	min. sens. norm solution
G_{sys}	4.075	5.064
G_{th}	0.1048	0.1036
G_{ST1}	4.834	5.846
G_{ST2}	2.636	1.379
G_{ST3}	0.8302	-1.735
$G_{\dot{th}}$	0.4095	0.3819
$G_{\dot{ST2}}$	1.145	1.598
$G_{\dot{ST3}}$	0.7031	1.136
---	---	---
G_{esth}	4.659	4.517
G_{esth}	4.602	4.521
G_{esst3}	4.075	5.325

Table 7.7 Eigenvalues for Experimental System Solutions

	Eigenvalues	
	min. gain norm solution	min. sens. norm solution
Model	-4.16 + i 65.3	-4.16 + i 63.3
	-6.10 + i 28.5	-6.28 + i 18.8
	-2.50 + i 5.14	-2.50 + i 9.03
	-2.50 + i 0.94	-2.49 + i 1.12
Estimators	-37.3 + i 0.00	-37.45 + i 0.00
	-45.23 + i 0.00	-45.47 + i 0.00
	-49.8 + i 0.00	-49.58 + i 0.00

Table 7.8 Normalized Eigenvalue ($Re(\lambda_i)$) Sensitivities for Minimum Gain Solution to Experimental System

	$-4.16\pm i65.3$	$-6.10\pm i28.5$	$-2.50\pm i5.14$	$-2.50\pm i0.94$
G_{sys}	0.142	-0.114	-13.4	17.8
G_{ST1}	0.0126	-0.269	-7.69	11.0
G_{ST2}	0.00861	-0.279	-4.99	6.05
G_{ST3}	0.0145	-0.00641	-0.766	0.719
$G_{\dot{th}}$	0.284	0.679	0.316	2.21
$G_{\dot{ST2}}$	0.292	-0.609	-0.872	-0.987
$G_{\dot{ST3}}$	0.0782	0.341	-0.173	-0.231
G_{esth}	0.222	0.128	-0.263	-0.185
G_{est2}	0.385	-0.0911	0.241	0.0669
G_{est3}	0.0579	0.141	0.0598	0.0143

	$-37.3+i0.0$	$-45.2+i0.0$	$-49.8+i0.0$
G_{sys}	-0.585	0.00599	0.00496
G_{th}	0.00968	-0.00008	0.00006
G_{ST1}	-0.230	0.00200	-0.00150
G_{ST2}	-0.0528	0.00040	-0.00028
G_{ST3}	0.00509	-0.00005	0.00004
$G_{\dot{th}}$	-0.704	0.0474	0.0159
$G_{\dot{ST2}}$	0.449	0.0455	-0.00724
$G_{\dot{ST3}}$	-0.612	0.00182	-0.0119
G_{esth}	2.810	-1.58	0.245
G_{est2}	-1.91	2.61	-0.0947
G_{est3}	0.172	-0.0157	0.848

Table 7.9 Normalized Eigenvalue (Re(λi)) Sensitivities for Minimum Sensitivity Norm Solution to Experimental System

	-4.16±i65.3	-6.28±i18.9	-2.50±i9.03	-2.49±i1.12
G_{sys}	0.116	-2.54	-1.41	13.5
G_{th}	0.0142	0.205	0.250	-0.905
G_{ST1}	-0.773	-3.72	1.54	12.5
G_{ST2}	0.00745	-0.799	-0.660	2.99
G_{ST3}	-0.0352	-.126	1.30	-1.43
$G_{\dot{gh}}$	0.253	0.860	4.91	1.93
$G_{\dot{ST2}}$	0.521	-0.0436	-6.38	-1.25
$G_{\dot{ST3}}$	0.128	1.61	-2.36	-0.346
G_{esth}	0.174	-0.710	-0.321	-0.160
G_{est2}	0.675	0.878	0.327	0.0803
G_{est3}	0.753	0.143	0.230	0.0186

	-37.5+i0.0	-45.5+i0.0	-49.6+i0.0
G_{sys}	-0.709	0.00087	-0.0582
G_{th}	0.0143	-0.00001	0.00082
G_{ST1}	-0.418	0.00043	-0.0266
G_{ST2}	-0.0413	0.00004	-0.00213
G_{ST3}	-0.0160	0.00002	-0.00120
$G_{\dot{th}}$	-1.16	-0.0350	0.154
$G_{\dot{ST2}}$	1.04	0.0350	-0.127
$G_{\dot{ST3}}$	-0.132	0.00038	-0.0566
G_{esth}	5.61	-5.30	1.73
G_{est2}	-5.02	6.29	-1.44
G_{est3}	0.314	-0.00225	0.765

Table 7.10 Comparison of Eigenvalue Position Robustness to Small Gain Perturbations for Minimum Sensitivity Norm and Minimum Gain Norm Solutions (Experimental System)

eigenvalues min. gain norm solution	eigenvalues +1% change in G	% change in Re(λ)	eigenvalues min. sens. norm solution	eigenvalues +1% change in G	% change in Re(λi)
-4.16±i65.3	-4.17±i65.3	0.2	-4.16±i63.3	-4.16±i63.3	0.0
-6.10±i28.5	-6.08±i28.5	-0.33	-6.28±i18.8	-6.23±i8.9	-0.8
-2.50±i5.14	-2.37±i5.02	-5.2	-2.50±i9.03	-2.48±i8.89	-0.8
-2.50±i0.94	-2.66±i0.734	6.4	-2.49±i1.12	-2.57±i1.06	3.2
-37.3+i0.0	-37.2+i0.0	-0.26	-37.5±i0.0	-37.4+i0.0	-0.27
-45.2+i0.0	-45.2+i0.0	0.0	-45.5±i0.0	-45.5+i0.0	0.0
-49.8+i0.0	-49.8+i0.0	0.0	-49.6±i0.0	-49.6+i0.0	0.0

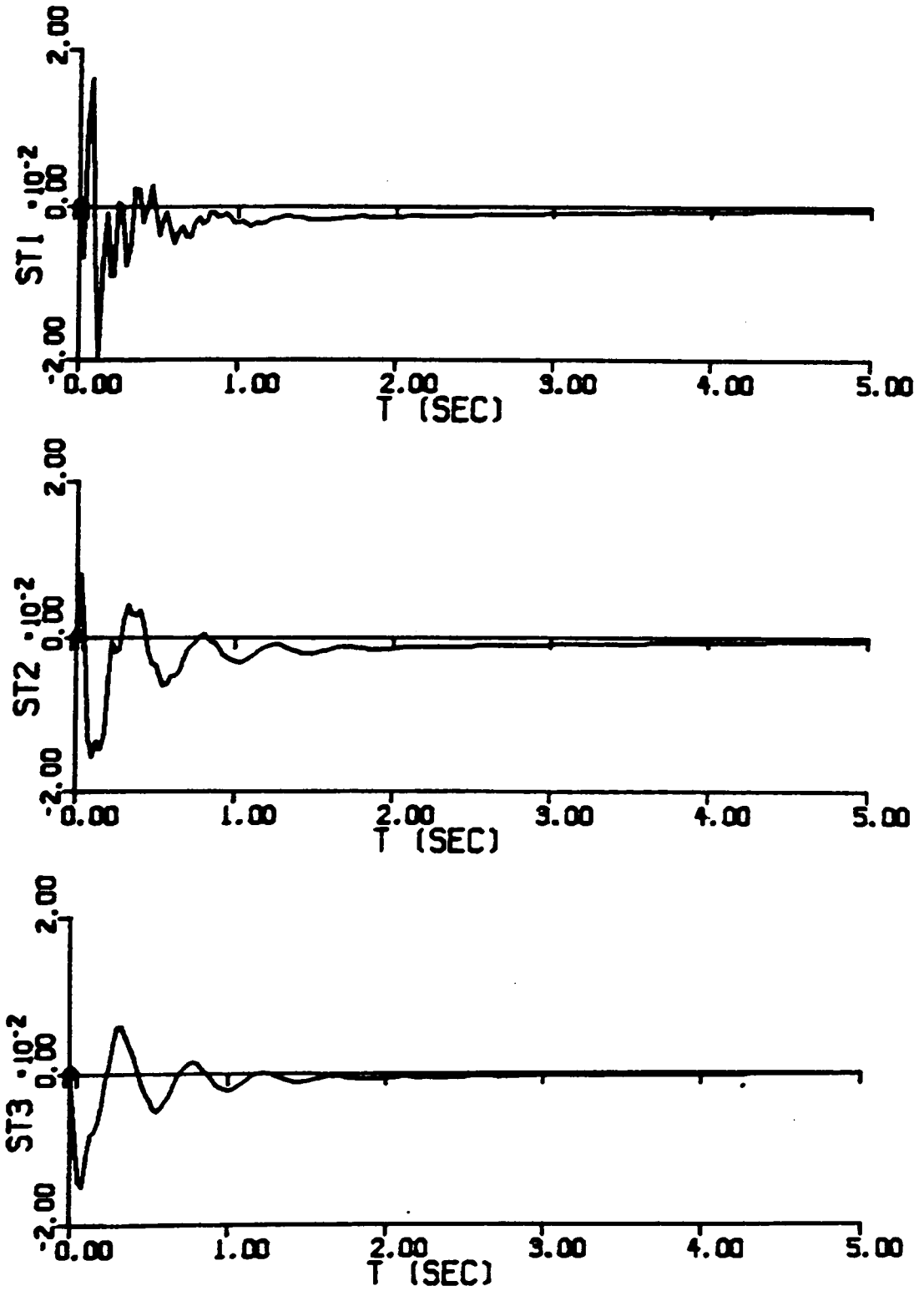

Fig. 7.14 Open Loop Response of Experimental System to an Impulse Force (units in volts)

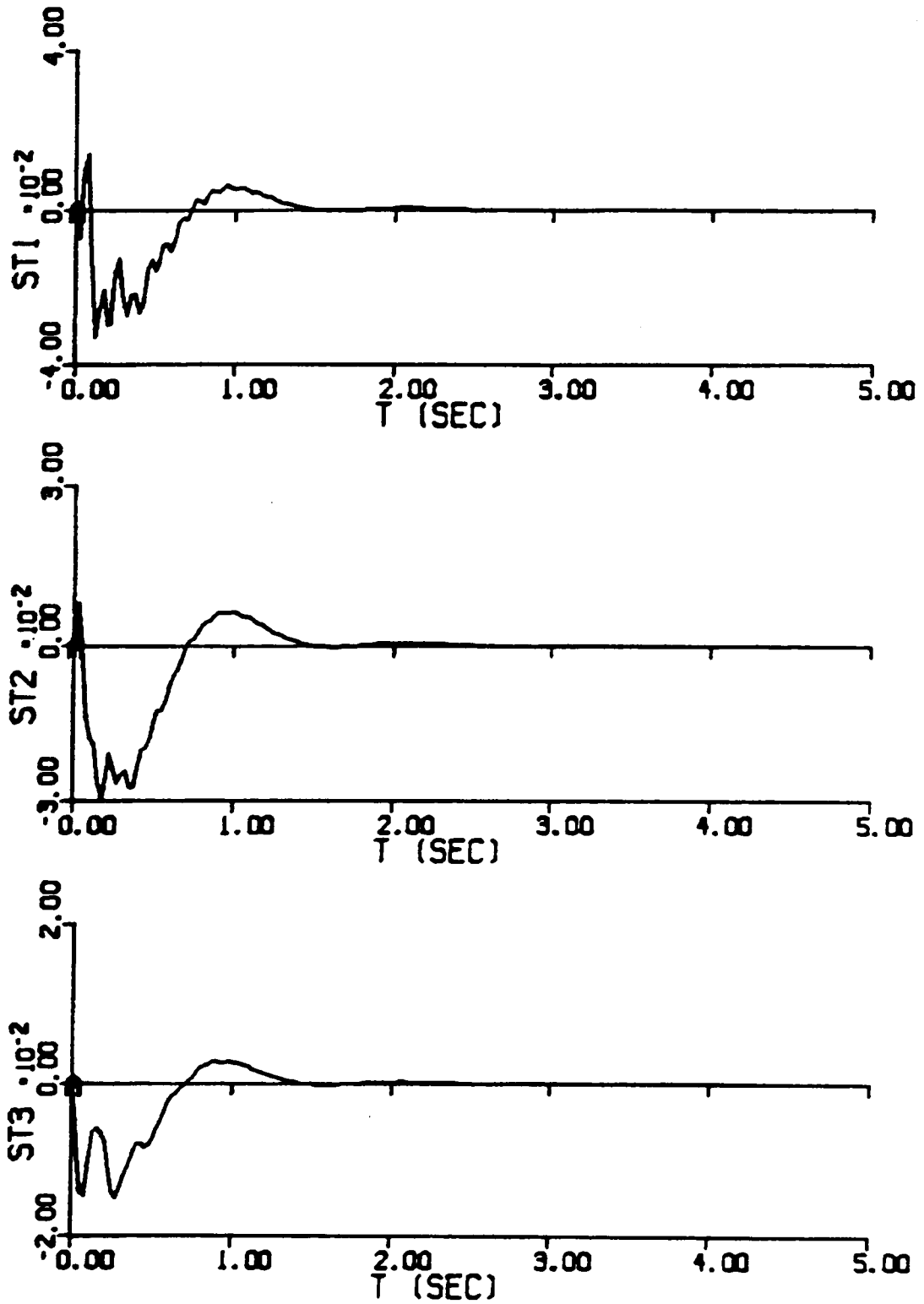

Fig. 7.15 Response to Impulse Force for Minimum Gain Norm Solution of Experimental Model (units in volts)

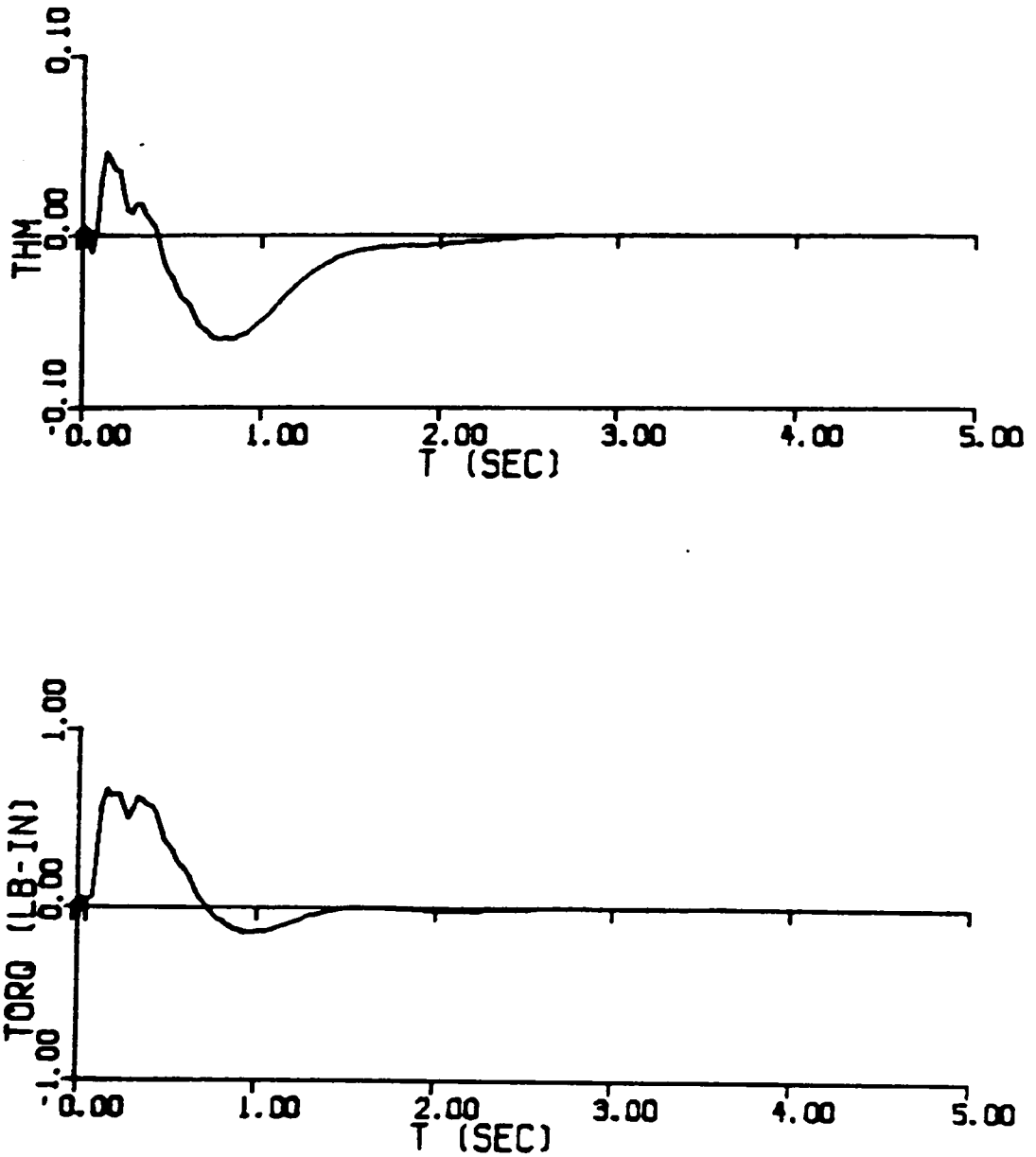

Fig. 7.16 Response to Impulse Force for Minimum Gain Norm Solution of Experimental Model (unspecified units in volts)

constraint, Eq. 7.6, is the same. However, note the dramatic difference in torque requirement for the same tasks. Clearly the system with back EMF requires more energy output than the system without.

The response of the closed-loop, minimum-sensitivity solution to the same impulse is shown in Fig. 7.17 and Fig. 7.18. As anticipated since eigenvalue positions were different, the two solutions for the experimental system do have qualitative differences. The only important difference, however, is in the 15% increase in torque requirements for the minimum sensitivity solution. This is still considerably less than the torque requirements of the example system shown in Fig. 7.9.

Similar results are visible in system response to the 45^{o} slewing maneuver. Simulation of the minimum gain norm solution is shown in Fig. 7.19 and 7.20; similation of minimum sensitivity norm solution is shown in Fig. 7.21 and Fig. 7.22. Comparison with each other and with the similar simulations for the example system lead to the same results written above.

For clarity, important results of this analytical study into these two systems and solutions are summarized below.

1. Minimum gain and minimum sensitivity solutions were generated for torque-controlled and voltage-controlled motor systems.
2. For all cases, eigenvalues were successfully positioned in accordance with the constraint Real $(\lambda_i) < -2.5$.
3. In general, system sensitivity appears to be exponentially related to eigenvalue constraint positions.

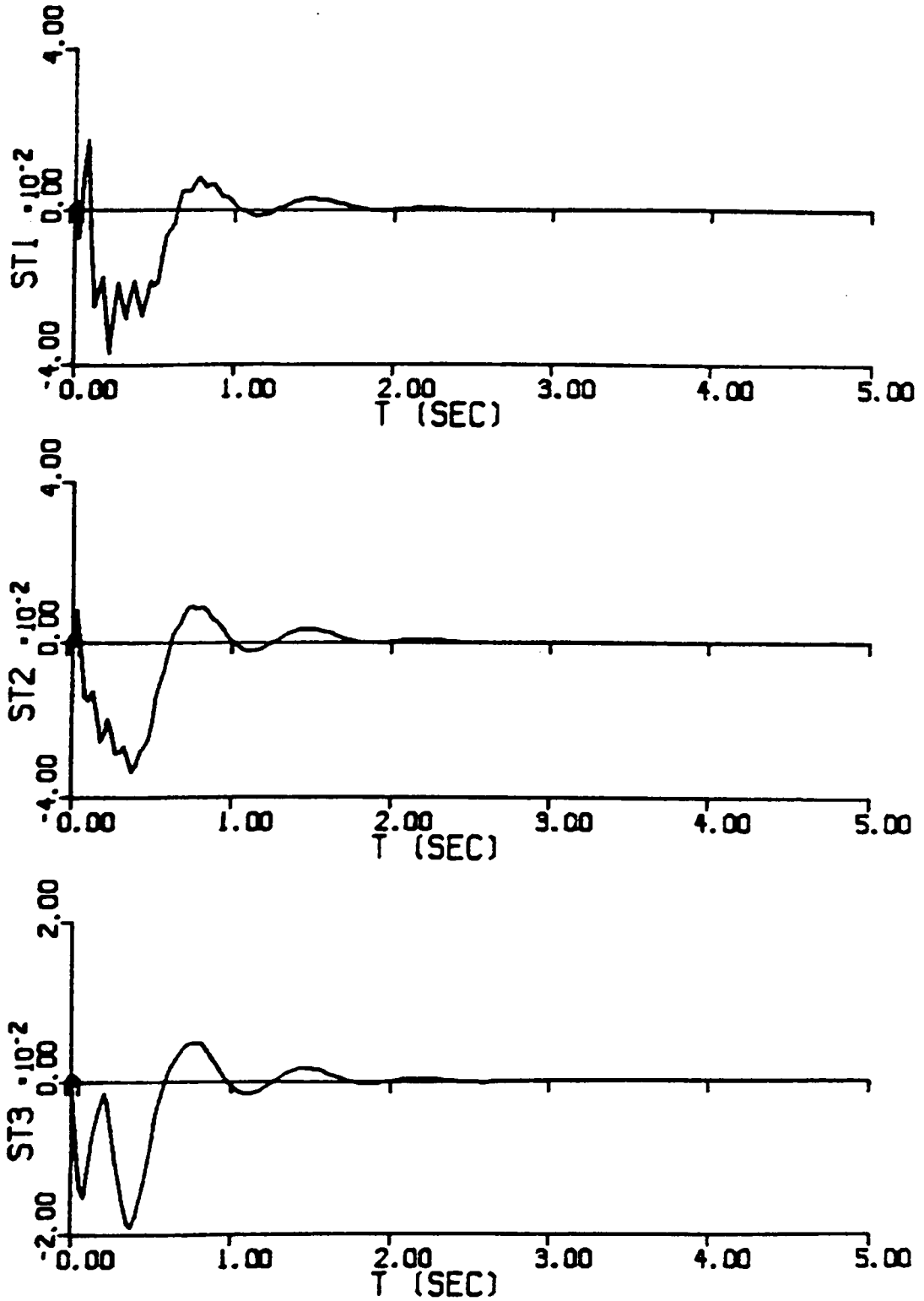

Fig. 7.17 Response to Impulse Force for Minimum Sensitivity Norm Solution of Experimental Model (units in volts)

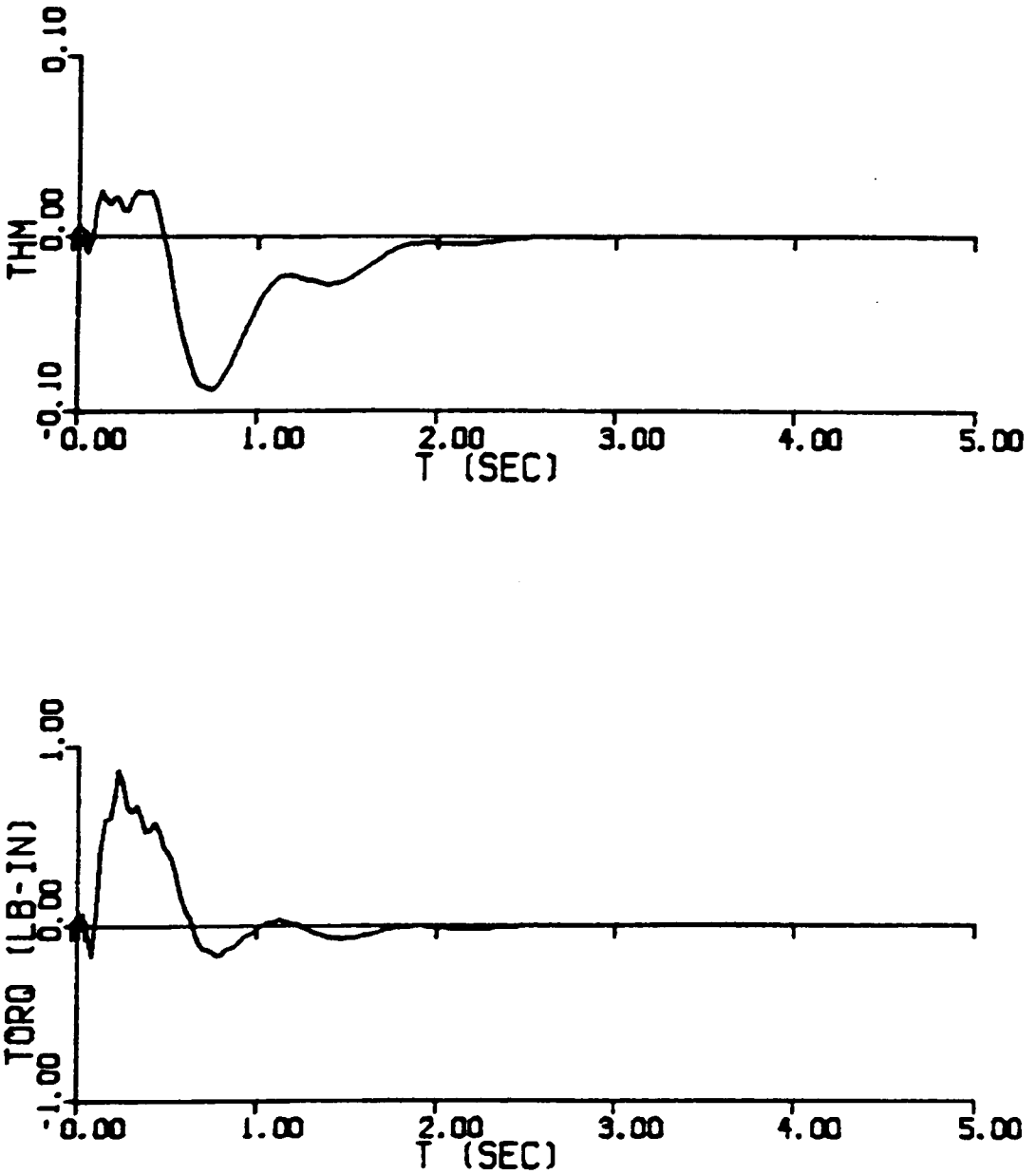

Fig. 7.18 Response to Impulse Force for Minimum Sensitivity Norm Solution of Experimental Model (unspecified units in volts)

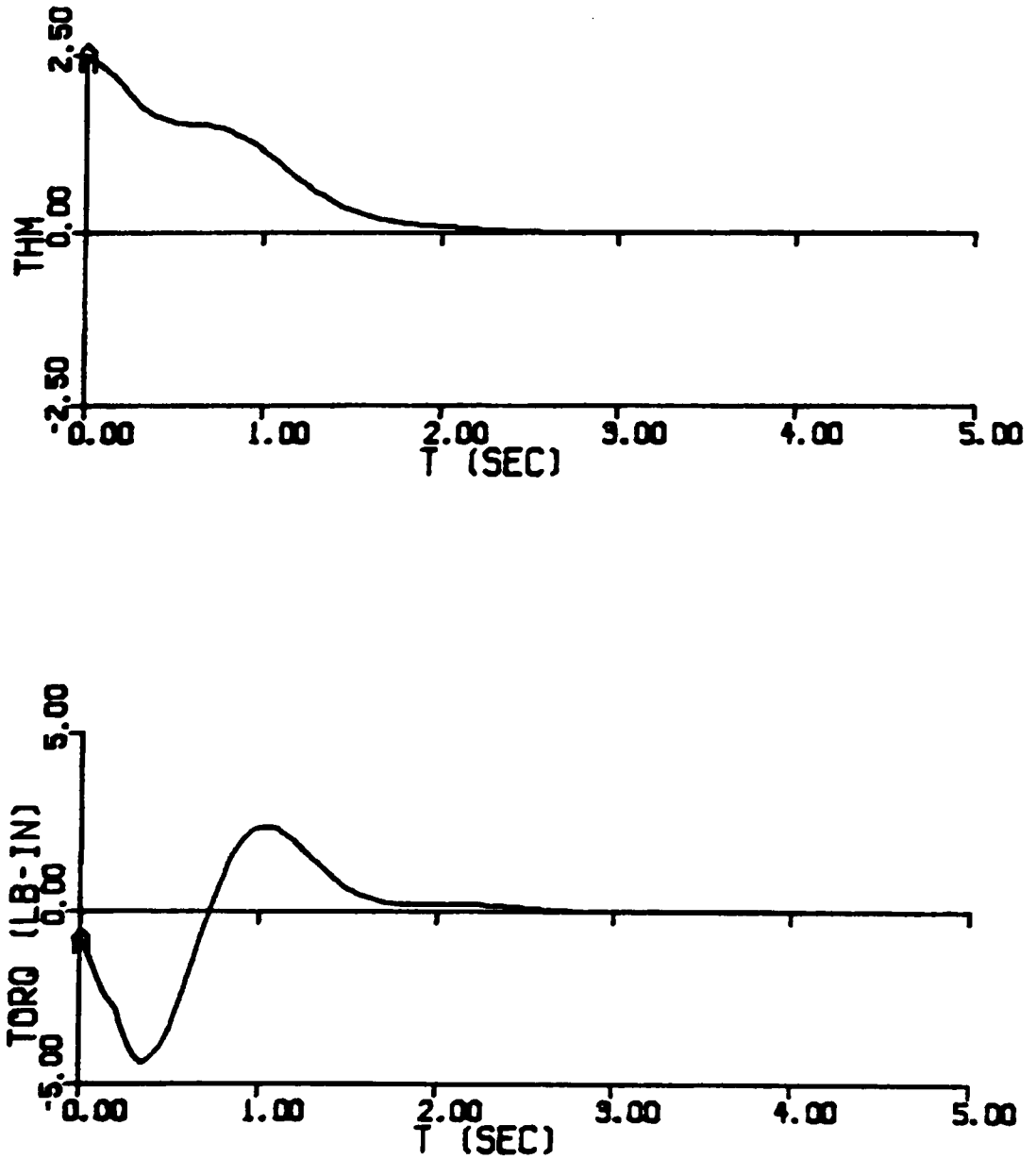

Fig. 7.19 Response to 45° Slewing Maneuver for Minimum Gain Norm Solution of Experimental Model (unspecified units in volts)

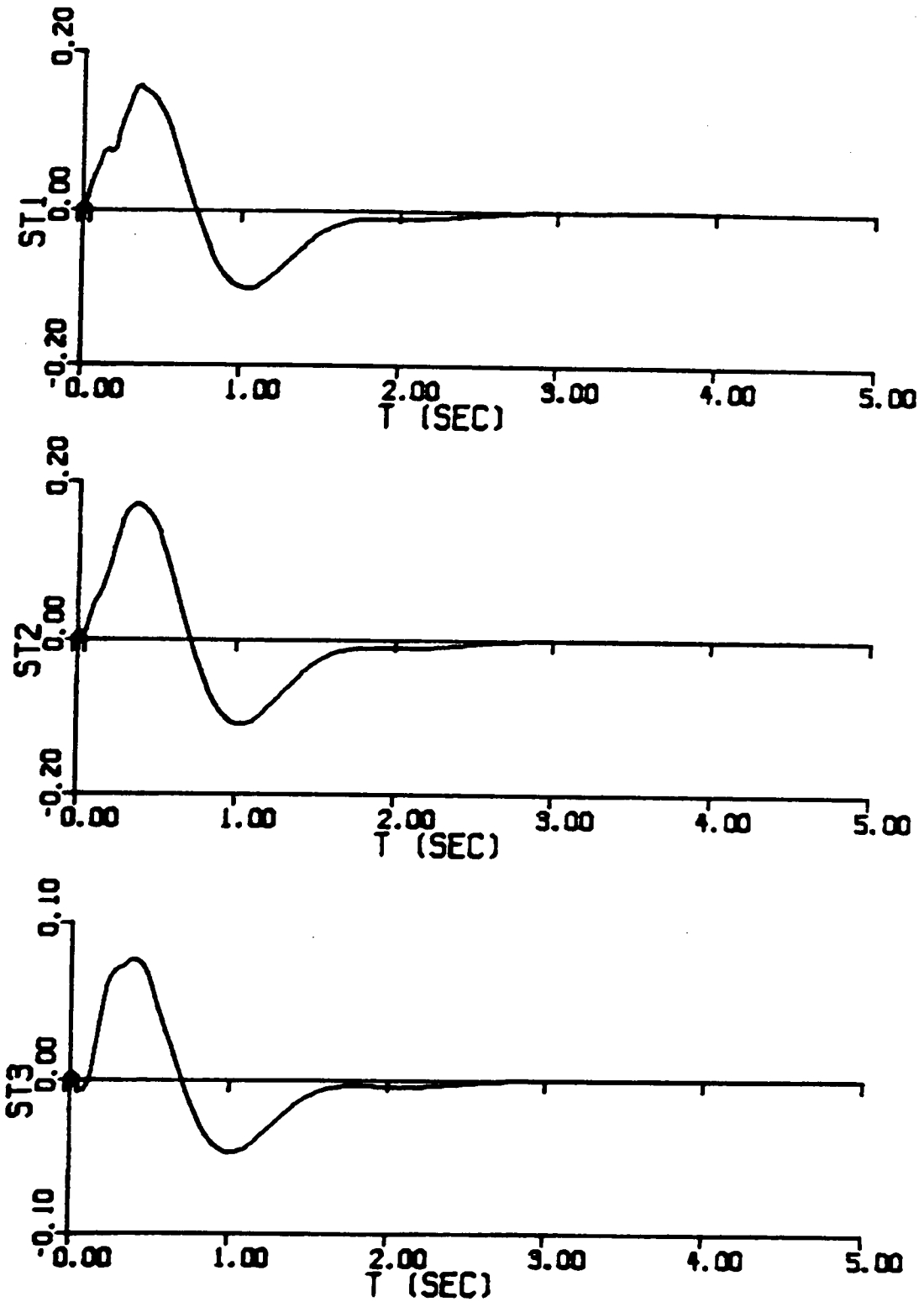

Fig. 7.20 Response to 45° Slewing Maneuver for Minimum Gain Norm Solution of Experimental Model (units in volts)

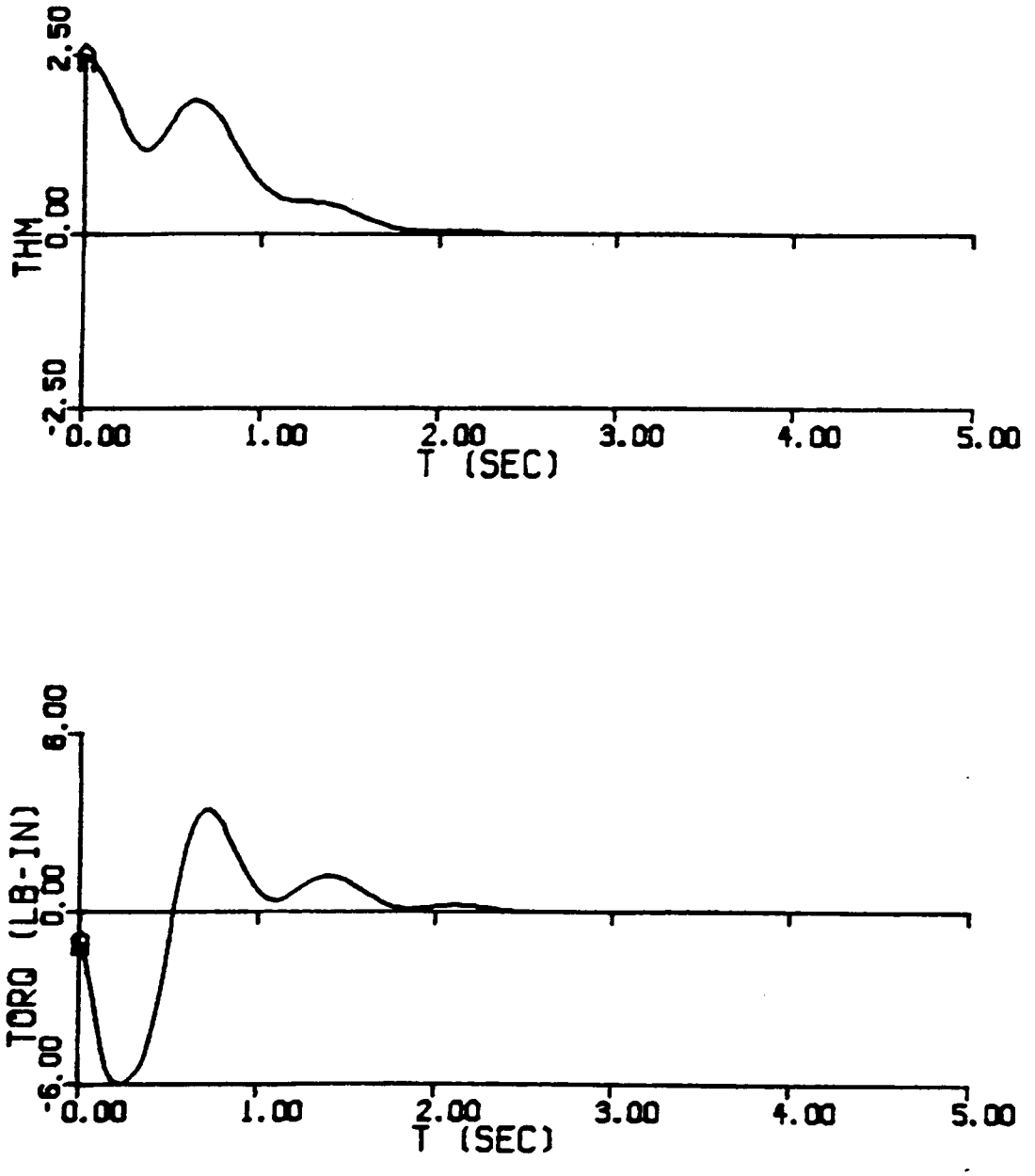

Fig. 7.21 Response to 45° Slewing Maneuver for Minimum Sensitivity Norm Solution of Experimental Model (unspecified units in volts)

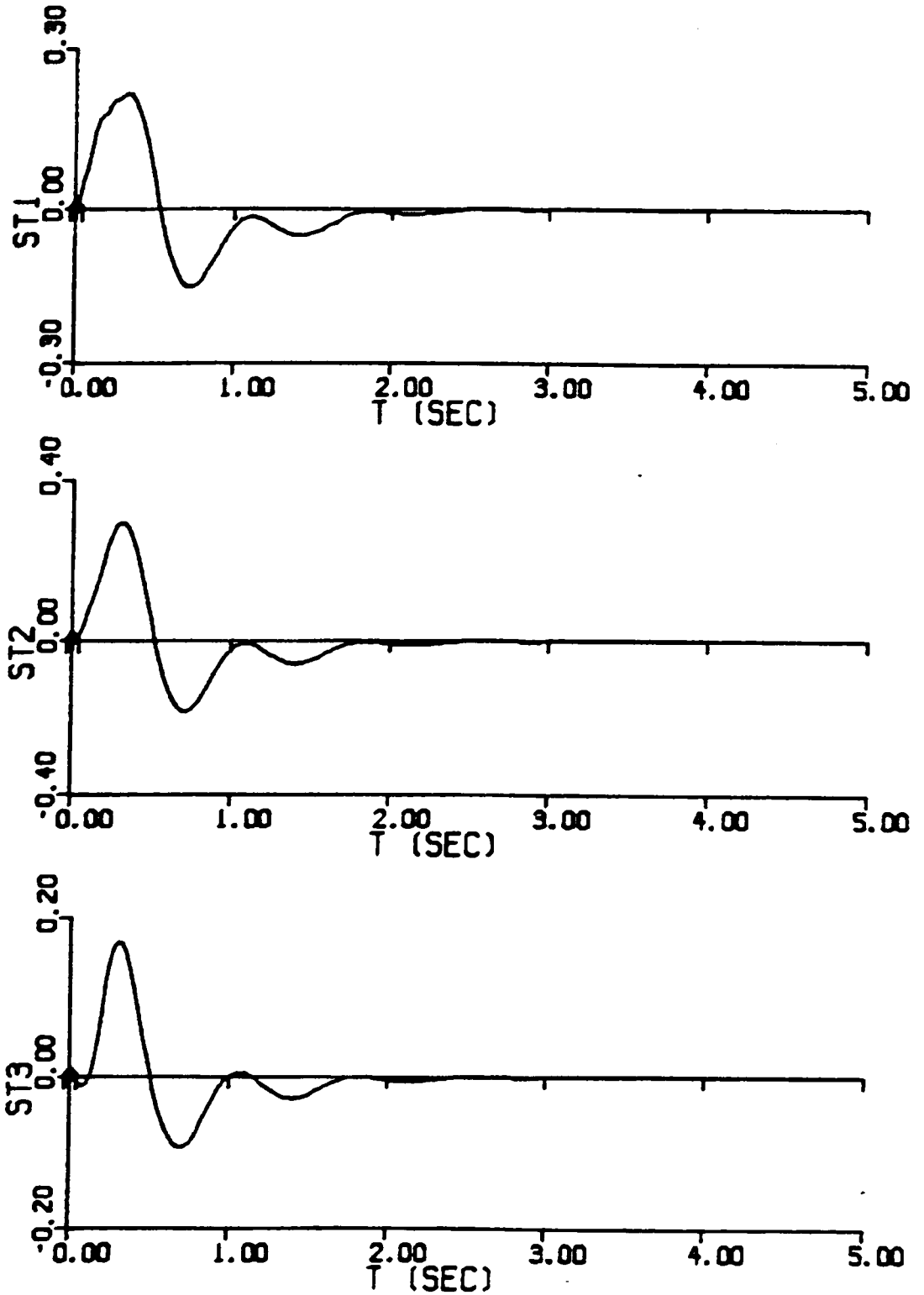

Fig. 7.22 Response to 45° Slewing Maneuver for Minimum Sensitivity Norm Solution of Experimental Model (units in volts)

4. With little other influence on system performance, the minimum sensitivity algorithm presented here has reduced net system sensitivity by ~70%.
5. Sensitivity of experimental system is considerably greater than example system.
6. Energy requirements of experimental system are considerably less than example system.

Chapter 8

EXPERIMENTAL RESULTS

In Chapter 6, the experimental model was "tuned" so that it more accurately represented actual hardware performance. Confidence in the model was attained through several comparison tests. With this confidence, the intentions here were to experimentally verify the analytical concepts developed in the last chapter; that is, compare minimum gain and minimum sensitivity solutions with each other and with the anticipated analytical results. However, there proved to be two unmodeled system characteristics which stood as obstacles in successful experimental implementation. Problems arose with the torque deadband in the motor (briefly mentioned in Ch. 2) and with closed-loop noise from the state estimators. These problems are clearly demonstrated with experimental data. Focused attempts to overcome these problems required new gain solution sets to be generated; all subsequent solutions are still generated with the minimum gain correction algorithm. Experimental data shows benefits and problems of each subsequent solution. Unfortunately, no solution could simultaneously overcome both obstacles; thus, desired system response was not experimentally achieved.

The first gain set experimentally implemented was the minimum gain norm solution given in Table 7-4. The eleven gains in this solution set were added one or several at a time. Here, the first feedback law implemented was for angular position. The feedback law looked like

$$V_a = - G_{sys} G_{th} \theta \qquad (8.1)$$

For this particular minimum gain norm solution, Eq. 8.1 looks like

$$V_a = -0.4271\ \theta \tag{8.2}$$

In Fig. 8.1, strip chart data is shown for system response to an initial angular displacement of $\pm 45^{o}$. Notice the in steady-state error in position in both tests. Clearly, this region of non-influence of the controller reflects the torque deadband in Chap. 2. It is important to note here that addition of other feedback components will not help this condition; all other gain components are independent and do not influence angular position. Therefore, from this simple preliminary test, it can be concluded that the minimum gain norm solution will not give the desired response.

When the full state feedback law is implemented, the second problem mentioned is clearly demonstrated. The beam vibrates with high frequency, low amplitude oscillations that are so severe that the beam gives off an audible hum. The source of this instability is traced back to closing the loop on the strain velocity estimators. This is clearly shown in Fig. 8.2. As seen, when these estimated signals are removed from the control law, the noise in the system drops off immediately. Note that the angular velocity estimator does not cause similar noise-related instabilities. This is most likely due to the difference in frequency content of position and strain measurements. Angular position measurement has a very low frequency content whereas beam vibrations and consequently strain measurements have a relatively higher frequency content. The estimator design presented in Chapter 2 apparently intro-

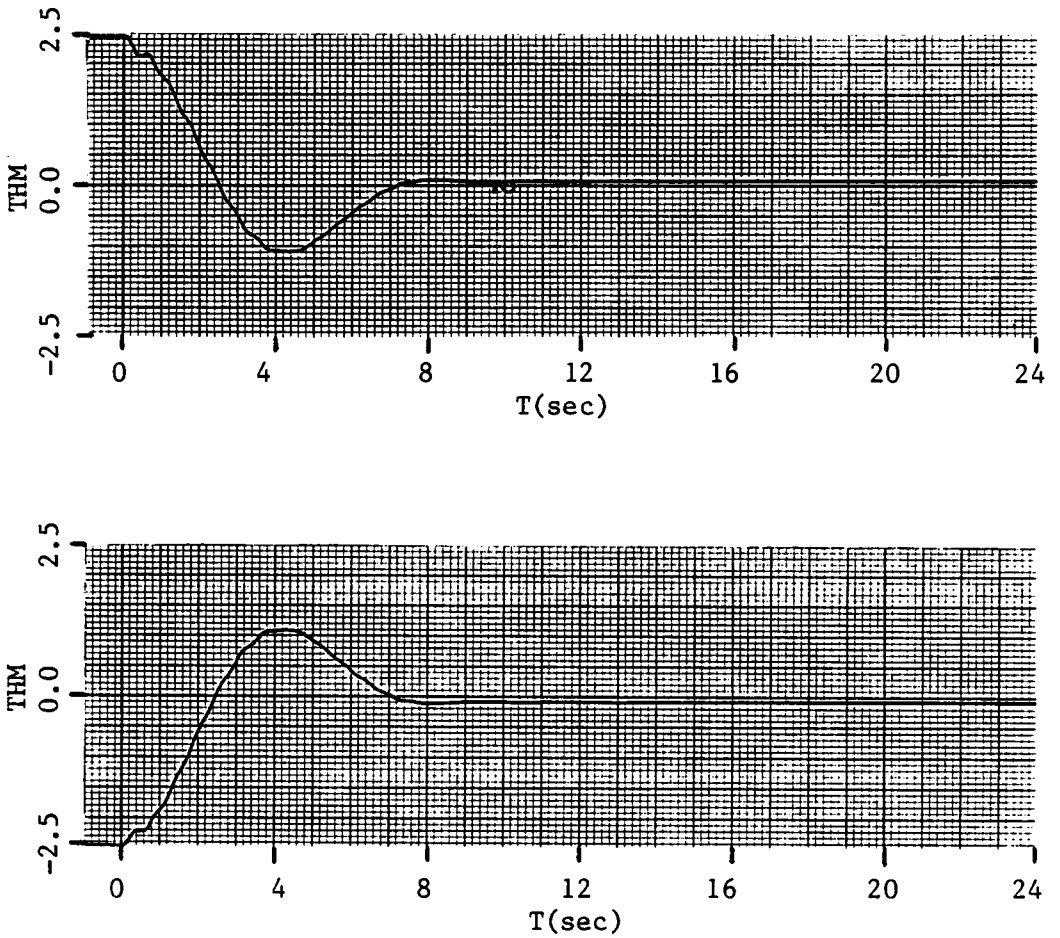

Fig. 8.1 Demonstration of Controller Deadband in Minimum Gain Norm Solution (units in volts)

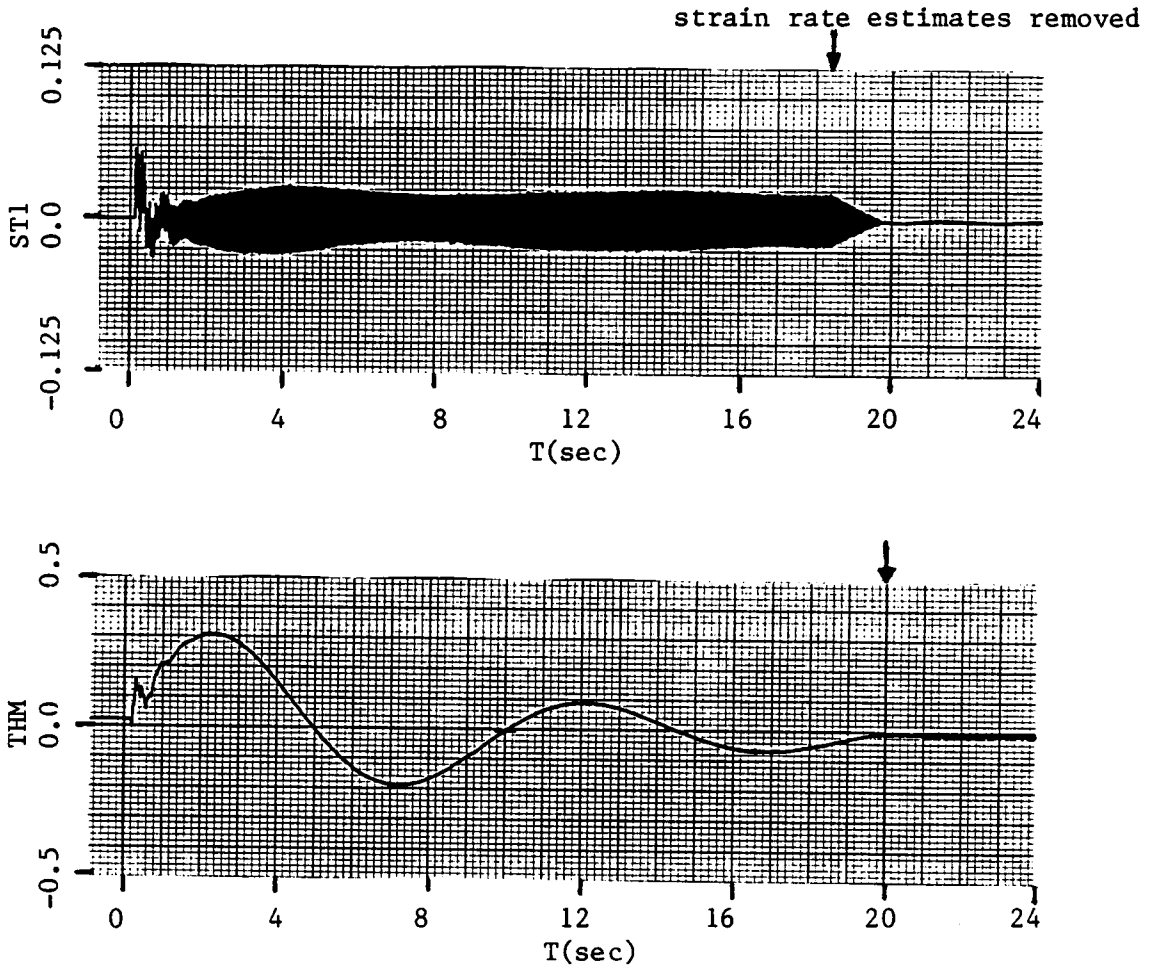

Fig. 8.2 Demonstration of Controller Instabilities due to Strain Rate Estimation in Min. Gain Norm Solution (units in volts)

duces too much noise into the estimated signal at high frequencies. When the feedback loop is closed around the estimators, this noise becomes a system input and drives the dynamics unstable. It should also be noted that the frequency content of the noise was approximately 60 Hz.

Clearly the original minimum gain norm solution gives unsatisfactory response. The minimum sensitivity norm solution will not offer any improvements either: θ feedback is still "weak" and the same estimators are still present. The three subsequent approaches presented here directly focus on these problems.

While the torque deadband cannot be eliminated, it might be possible to compensate for it or at least minimize its visible effects. Compensation techniques are being developed but no experimental testing has been done yet. The approach taken here is to minimize the visible effects of the torque deadband by increasing system gains.

Recall from Chapter 4 that the gain iteration algorithm is typically given very small initial (starting) gains. Since the algorithm meets constraints by solving a minimum gain correction norm, the final solution approximates a minimum gain norm solution. Experimentally, a minimum gain solution was found to be inadequate. A more robust (to torque deadband) gain set is calculated by simply using large initial gains in the algorithm. The resulting gain set is shown in Table 8.1. By comparing these gains to the gains in Table 7.4, it is clear that a more robust gain set has indeed been calculated. Note that the estimator poles were moved in to around -25 in an effort to decrease noise.

Table 8.1 "Robust" Gain Set for Experimental System

G_{sys}	2.496
G_{th}	0.7308
G_{ST1}	2.556
G_{ST2}	3.529
G_{ST3}	1.740
$G_{\dot{th}}$	5.684
$G_{\dot{ST2}}$	12.46
$G_{\dot{ST3}}$	3.809
G_{esth}	2.232
G_{est2}	2.123
G_{est3}	2.508

As before, a position feedback law is implemented first. For this system, the control law of Eq. 8.1 looks like

$$V_a = -1.824\ \theta \tag{8.3}$$

In Fig. 8.3, this system's response to a 45^o initial displacement is shown. As seen and as hoped, the response is considerably more energetic. Note that although the torque-deadband is still present, control-deadband has been reduced significantly by increasing system gains.

When the full feedback law is implemented, once again high frequency instabilities arise. As before, they are related to closing the feedback loop around the strain velocity estimates. The noise instability is shown growing from an at rest position in Fig. 8.4.

Clearly it is necessary to change the estimator structure or simply eliminate them from the control law. The latter is the next approach taken here; changing the estimator structure could result in the same or even new problems.

Recall from Chap. 4 that the iteration algorithm must have more gains to adjust than constraints to meet. With the strain velocity signals no longer available for feedback, the algorithm reaches its limit; there is one more gain than constraint. So while a minimum gain norm solution may still be calculated, it would now be impossible to introduce the performance index constraint.

The control law now feeds back all components of the measurement vector, $\underline{m}$ (Eq. 2.17) and an estimate of angular velocity. As mentioned before, the low frequency angular position measurements do not cause the

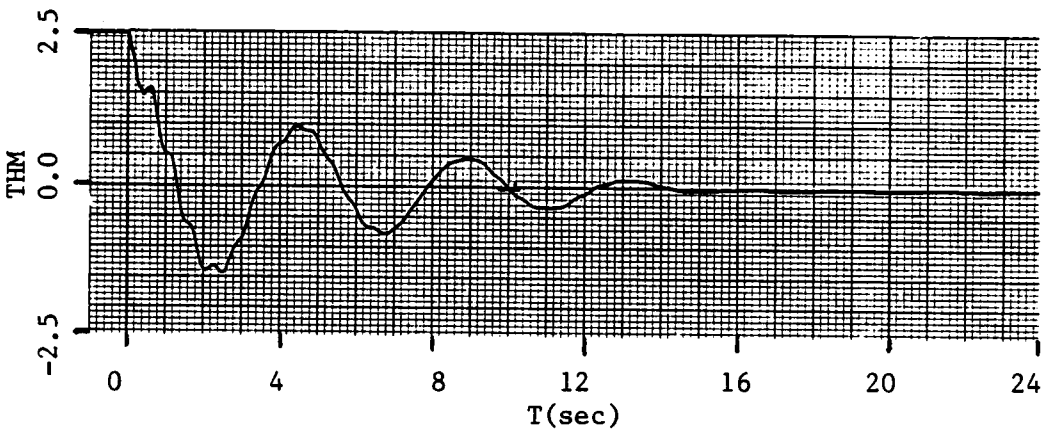

Fig. 8.3 Improved Response in Compensating for Torque Deadband with Robust Gain Set

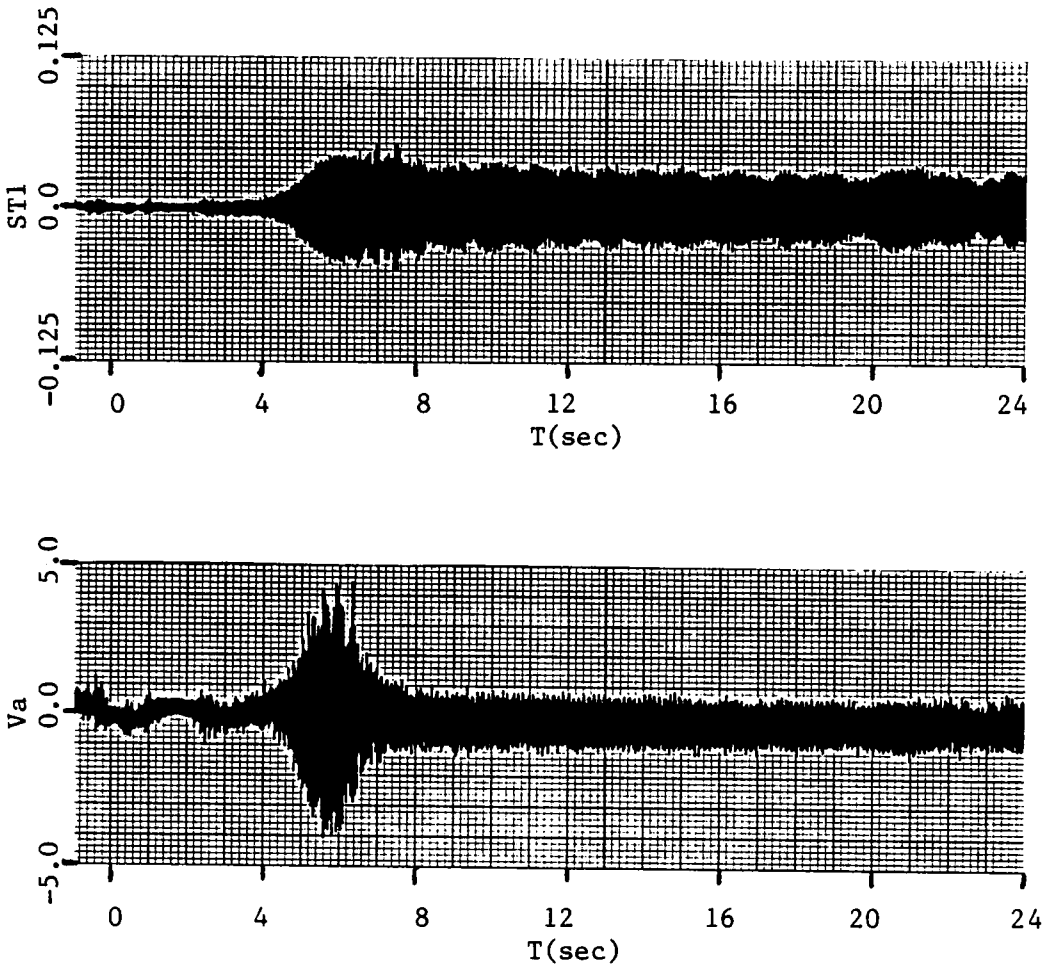

Fig. 8.4 Noise Instabilities due to Strain Rate Estimation Growing from Rest Position with Robust Gain Set

same problems that the strain measurements do in state estimation. Intuitively, good system response could be achieved with this feedback law if the gains could be made "robust" to the torque deadband. Unfortunately, the iteration algorithm could not successfully iterate from a robust initial gain set to a final gain set that met the constraints. In all attempts, the algorithm went unstable. There is no clear path for the algorithm to iterate along from the initial conditions to final desired gain set.

With a very small initial gain set, a minimum gain norm solution could be calculated. This gain set is shown below in Table 8.2. As anticipated though, this solution does not overcome the torque deadband problems seen before. For this gain set, the angular position feedback law of Eq. 8.1 looks like

$$V_a = -0.3133\ \theta \tag{8.4}$$

Full feedback implementation is shown in Fig. 8.5. While, instabilities have been eliminated, the response is clearly unsatisfactory.

As mentioned earlier, best results could be achieved with a robust set of gains in the partial feedback (no strain velocity estimates) control law just described. In all previous analytical and experimental applications of the iteration algorithm, it performed consistantly and reliably. However, it failed in its most promising application here. The difference between this application and all others is primarily in the gain/constraint relationship (mentioned before). Here, this relationship is as close as the algorithm can tolerate while in all other

Table 8.2 Minimum Gain Norm Solution with no Strain Velocity Estimation for Experimental System

G_{sys}	0.651
G_{th}	0.4813
G_{ST1}	7.979
G_{ST2}	30.12
G_{ST3}	21.20
$G_{\dot{th}}$	1.798
G_{esth}	3.389

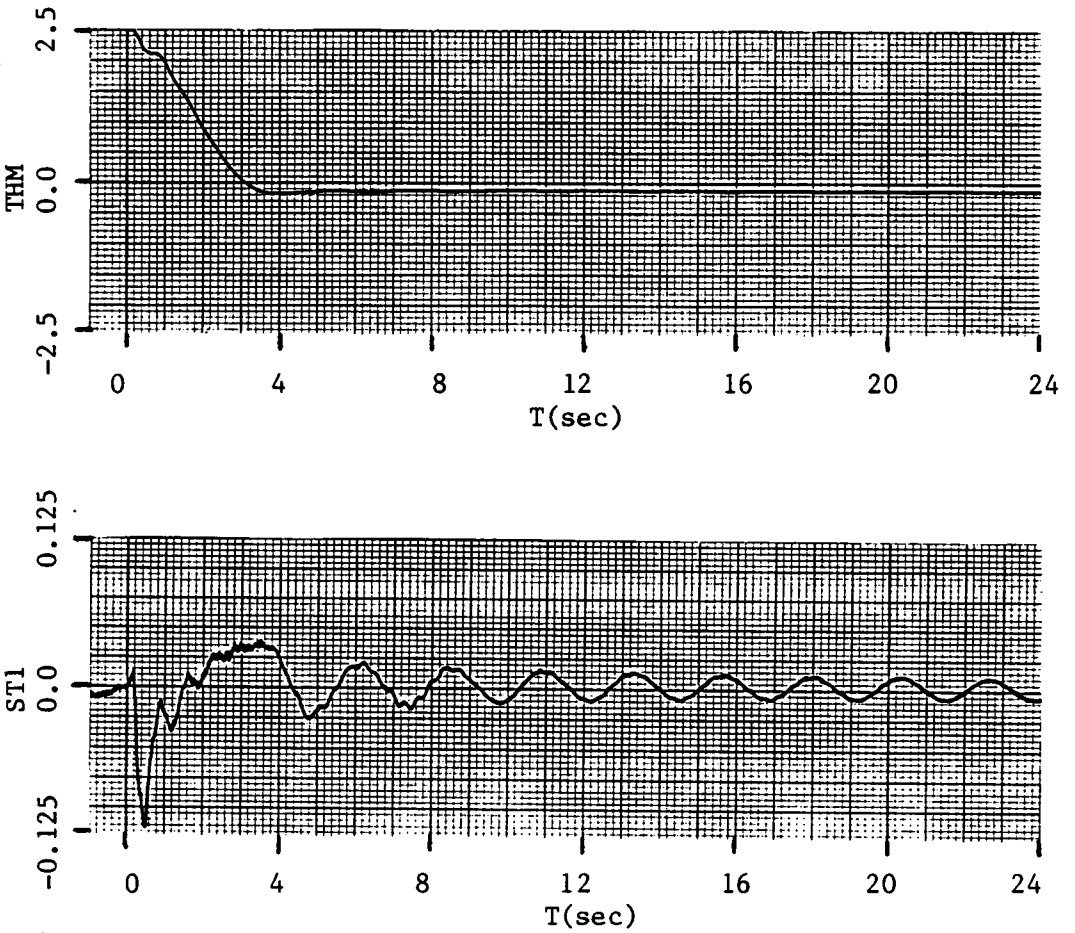

Fig. 8.5 Demonstration of non-robust Controller Design in Minimum Gain Norm Solution with no Strain Rate Estimation

applications there was considerably more "slack." Perhaps another algorithm (26) not dependent upon a gain/constraint relationship would be better suited to calculating gains in this partial output feedback application.

Summarizing the results of this section,

1. Attempts were made at experimentally verifying concepts developed in Chap. 7.
2. Chief obstacles incurred were controller deadband due to unmodeled torque deadband in motor and noise instabilities related to closing loop around state estimators.
3. Focused attempts were made at overcoming problems. While each problem could be dealt with separately, no solution could be generated that solved both simultaneously.
4. The best response from this system would be achieved with "robust" gains in a partial output (no strain estimators) feedback law.
5. A different gain selection algorithm might be better suited to solve for this particular solution.

Chapter 9

CONCLUSIONS AND RECOMMENDATIONS

The following is a summary of goals attained and conclusions reached in this thesis:

1. System response characteristics are highly sensitive to damping in the beam/motor system. Knowledge of system's damping characteristics is therefore critical.
2. A system model with improved accuracy was attained by including damping determined from experimental data.
3. Min. gain norm and minimum sensitivity norm solutions were generated for both torque-controlled and voltage-controlled motor systems. In all cases, all eigenvalues were forced to meet the constraint Real $(\lambda_i) \leq -2.5$.
4. Minimum sensitivity norm improves system response characteristics over min. gain norm solution in that it increases system's robustness to small gain perturbations by $\sim 70\%$ while maintaining similar energy (torque) requirements.
5. In general, system sensitivity appears to be exponentially related to the eigenvalue constraints considered in this thesis.
6. System with torque-controlled motor had about 5 times less torque requirements than with voltage-controlled motor.
7. However, the system with torque-controlled motor was also significantly more sensitive to small gain perturbations.
8. Successful experimental implementation of desired control objectives was not achieved. Chief obstacles were from a torque-deadband present in the motor and also from noise related unstabilities due to strain rate estimation.

9. Rate estimation of high frequency signals is unsuitable for stable and reliable feedback control of this flexible system.

With these conclusions in mind, the author makes the following brief recommendations for future research related to this system:

1. Torque deadband needs to be eliminated either by electrical compensation techniques or perhaps better yet with a new motor.
2. Strain rate estimation needs to be eliminated from the control law. This reduces the control law to partial output feedback. In this situation, other eigenvalue placement algorithms need to be investigated which are better suited for this application.
3. Improved techniques for identifying system damping need to be investigated.

These remarks conclude this thesis.

REFERENCES

1. Meirovitch, L. (ed.), Proceedings of the 1st VPI&SU/AIAA Symposium on Dynamics and Control of Large Flexible Spacecraft, Blacksburg, VA, June 1977.

2. Meirovitch, L. (ed.), Proceedings of the 2nd VPI&SU/AIAA Symposium on Dynamics and Control of Large Flexible Spacecraft, Blacksburg, VA, 1979.

3. Meirovitch, L. (ed.), 3rd VPI&SU/AIAA Symposium on Dynamics and Control of Large Flexible Spacecraft, Blacksburg, VA, June 1981.

4. Meirovitch, L. (ed.), 4th VPI&SU/AIAA Symposium on Dynamics and Control of Large Flexible Spacecraft, Blacksburg, VA, June 1983.

5. Meirovitch, L. (ed.), 5th VPI&SU/AIAA Symposium on Dynamics and Control of Large Flexible Spacecraft, Blacksburg, VA, June 1985.

6. Balas, M. J., "Trends in Large Space Structure Control Theory: Fondest Hopes, Wildest Dreams," IEEE Transactions on Automatic Control, Vol. AC-27, No. 3, pp. 522-535, June 1982.

7. Montgomery, R. C. and Taylor, L. W., "Results of Studies at Langley Research Center on the Control of Flexible Structures," Large Space Antenna Technology--1982, NASA Conference Publishment 2269-pt. 2, Hampton, VA, Dec. 1982.

8. Horner, G. C., "Optimum Damper Locations for a Free-Free Beam," Large Space Systems Technology - 1980, NASA Conference Publication 2168, pt. 2, Hampton, VA, Nov. 1980.

9. Hallauer, W. L., Jr., Skidmore, G. R., and Gehling, R. N., "Modal-Space Active Damping of a Plane Grid: Experiment and Theory," Journal of Guidance, Control and Dynamics, Vol. 8, No. 4, May-June 1985, pp. 366-373.

10. Conault, C., "Discovery Will Erect 102 A Structure," Aviation Week and Space Technology, Vol. 120, 18 June 1984, pp. 57-60.

11. Schaechter, D. B. and Eldred, D. B., "Experimental Demonstration of the Control of Flexible Structures," Journal of Guidance, Control and Dynamics, Vol. 7, No. 5, Sept.-Oct. 1984, pp. 527-534.

12. Mills, R. A., "Active Vibration Control of a Cantilevered Beam: A Study of Actuators," presented at 34th Congress of the International Astronautical Federation, Budapest, Hungary, Oct. 10-15, 1983.

13. Alberts, T. A., Hastings, G. G., Book, W. J., and Dickerson, S. L., "Experiments in Optimal Control of a Flexible Arm with Passive Damping," presented at 5th VPI&SU/AIAA Symposium on Dynamics and Control of Large Flexible Space Structures, Blacksburg, VA, June 1985.

14. Robertshaw, H. H., "Analog Position Control of a Flexible Beam via Root Torque Actuation," report to NASA Structural Dynamics Branch, August 1984, Hampton, VA.

15. Balas, M. J., "Direct Output Feedback Control of Large Space Structures," Journal of the Astronautical Sciences, Vol. 27, No. 2, April-June 1979, pp. 157-180.

16. Bodden, D. S. and Junkins, J. L., "Eigenvalue Optimization Algorithms for Structural/Controller Design Iterations," presented at 1984 American Controls Conference, June 6-8, 1984, San Diego, CA.

17. Junkins, J. L., Bodden, D. S., and Turner, J. D., "A Unified Approach to Structure and Control System Design Iterations," presented to Fourth International Conference on Applied Numerical Modeling, Dec. 27-29, 1984, Tainan, Taiwan.

18. Rew, D. W., and Junkins, J. L., "In Search of the Optimal Quadratic Regulator," presented at 5th VPI&SU/AIAA Symposium Dynamics and Control of Large Flexible Space Structures, Blacksburg, VA, June 1985.

19. Lim, B. L. and Junkins, J. L., "Minimum Sensitivity Eigenvalue Placement via Sequential Linear Programming," Proceedings of the Mountain Lake Dynamics and Control Institute, Mountain Lake, VA, June 9-11, 1985.

20. Meirovitch, L., Methods of Analytical Dynamics, McGraw-Hill, New York, NY, 1970.

21. Mounfield, W. P., Adaptive Positioning Control by Signal Synthesis, M.S. Thesis, Dept. of Mech. Engr., VPI&SU, Blacksburg, VA, December 1980.

22. Bodden, D. S. Structure/Controller Design Interations for Feedback Control of Flexible Structures, M.S. Thesis, Dept. of Eng. Sci. & Mech., VPI&SU, Blacksburg, VA, August 1984.

23. Bodden, D. S., "Fortran Code for Structure/Controller Design Iterations for Feedback Control of Flexible Structures," VPI&SU Report No. VPI-E-84-28, Blacksburg, VA, August 1984.

24. Plant, R. H. and Huseyin, K., "Derivatives of Eigenvalues and Eigenvectors in Non-Self-Adjoint Systems," AIAA Journal, Vol. 11, No. 2, pp. 250-251, Feb. 1973.

25. Thomson, W. T., Theory of Vibration with Applications, Prentice-Hall, Inc., Englewood Cliffs, NJ, 1981.

26. Horta, L. G., Juang, J-N, and Junkins, J. L., "A Sequential Linear Optimization Approach for Controller Design," Proceedings of AIAA Guidance Navigation and Control Conference, Snowmass, CO, August 1985, pp. 725-731.

APPENDIX A

SYSTEM MODELING DETAILS

A.1 Shape Functions Chosen for System Model

The shape functions, $\phi(x)$ in Eq. 2.1 are the first three mode shapes of a cantilevered beam. Figure A.1 shows the forces and moments acting on an element on a cantilevered beam in bending (25). V and M are shear and bending moments, respectively, and p(x) is the loading per unit length of the beam. Summing forces and moments

$$\Sigma F_x = 0 \tag{A.1-1}$$

$$+\uparrow \Sigma F_y = p(x)dx - dV = 0 \tag{A.1-2}$$

$$+\circlearrowleft \Sigma M_{\substack{\text{right}\\ \text{side}}} = M + dM - M - Vdx - \tfrac{1}{2} p(x)dx^2 = 0 \tag{A.1-3}$$

In the limit Eqs. A.1-2 and A.1-3 become

$$\frac{dV}{dx} = p(x) \tag{A.1-4}$$

$$\frac{dM}{dx} = V \tag{A.1-5}$$

substituting (A.1-5) into A.1-4) yields

$$\frac{d^2M}{dx^2} = \frac{dV}{dx}\, p(x) \tag{A.1-6}$$

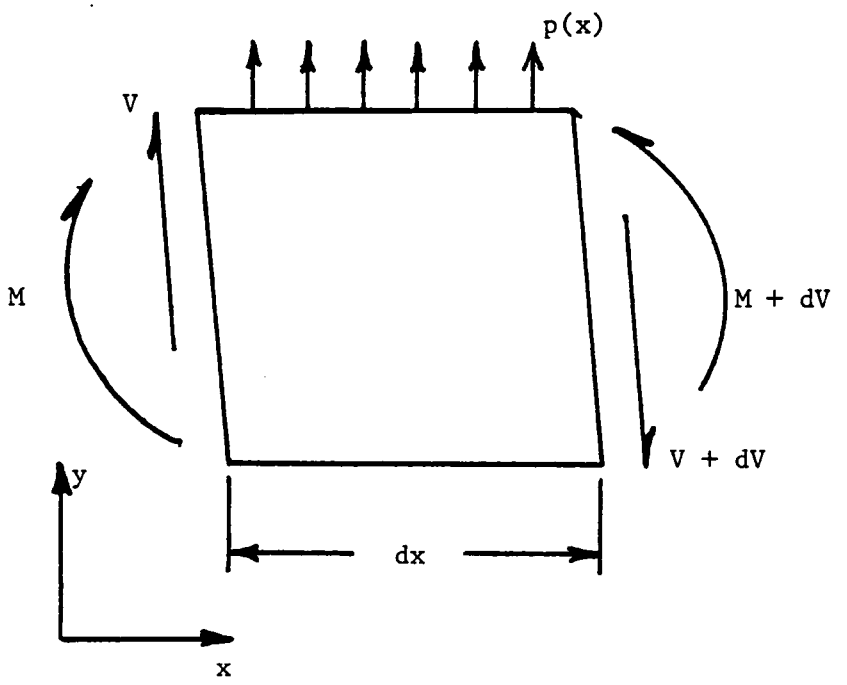

Fig. A.1 Forces and Moments Acting on an Element of a Beam in Bending

Substituting for M in Eq. (A.1-6) with the relation

$$M = EI \frac{d^2y}{dx^2} \tag{A.1-7}$$

gives

$$\frac{d^2}{dx^2}\left(EI \frac{d^2y}{dx^2}\right) = p(x) \tag{A.1-8}$$

For a beam vibrating about its static equilibrium position, p(x) is equal to the inertia load of its mass and acceleration (25). So, assuming harmonic oscillations

$$p(x) = \rho\omega^2 y(x) \tag{A.1-9}$$

where ρ is mass per unit length. Assuming a constant EI for the beam, Eq. A.1-8 is now written as

$$\frac{d^4y}{dx^2} - \beta^4 y = 0 \tag{A.1-10}$$

where $\beta = \frac{\ell\omega^2}{EI}$.

Assuming an exponential solution and applying Euler's Equations, the general form of the solution to A.1-10 is

$$y(x) = A \cosh \beta x + B \sinh \beta x + C \cos\beta x + D\sin\beta x \tag{A.1-11}$$

For a cantilevered beam, the boundary conditions are

$$
\begin{aligned}
x = 0 : \quad & y = 0 \\
& \frac{dy}{dx} = 0 \\
x = L : \quad & M = 0 \text{ or } \frac{d^2y}{dx^2} = 0 \\
& V = 0 \text{ or } \frac{d^3y}{dx^3} = 0
\end{aligned}
\qquad \text{(A.1-12)}
$$

In solving (A.1-10) subject to (A.1-12), an intermediate equation in β arises

$$\cosh\beta\ell \cos\beta\ell + 1 = 0 \qquad \text{(A.1-13)}$$

Solutions for β in this equation are determined by iteration and correspond to each mode of vibration. This leads to expressing the solution of A.1-10 subject to A.1-12 as the infinite series

$$y(x) = \sum_{i=1}^{n} (\cosh\beta_i x - \cos\beta_i x) + A_i(\sinh\beta_i x + \sin\beta_i x) \qquad \text{(A.1-14)}$$

where

$$A_i = - \frac{\sinh(\beta_i \ell) + \sin(\beta_i \ell)}{\cosh(\beta_i \ell) + \cos(\beta_i \ell)} .$$

For the first three modes

$$\beta_1 = \frac{1.875}{\ell} , \quad \beta_2 = \frac{4.694}{\ell} , \quad \beta_3 = \frac{7.855}{\ell} \qquad \text{(A.1-15)}$$

The first three mode shapes expressed in A.1-14 and A.1-15 are shown in Fig. A.2.

Recalling the relation in A.1-10 $\beta^4 = \frac{\ell\omega^2}{EI}$, the natural frequencies of vibration can be solved for as

$$\omega_{n_i} = (\beta_i \ell)^2 \sqrt{\frac{EI}{\rho \ell^4}} \qquad \text{(A.1-16)}$$

The natural frequencies of the beam used in this then are

$\omega_1 = 0.53$ hz $\qquad \omega_2 = 3.61$ hz $\qquad \omega_3 = 10.1$ hz .

A.2 Linearization

The "full blown" nonlinear equations resulting from solution of Lagranges Equations are

$$m(\frac{L^3}{3} + \beta_1 q_1^2 + \beta_2 q_2^2 + \beta_3 q_3^2)\ddot{\theta} + m(\alpha_1 \ddot{q}_1 + \alpha_2 \ddot{q}_2 + \alpha_3 \ddot{q}_3) + (2m\beta_1 \dot{q}_1 + 2m\beta_2 \dot{q}_2 + 2m\beta_3 \dot{q}_3)\dot{\theta}\, T_a(t) \qquad \text{(A.2-1)}$$

$$m(\beta_1 \ddot{q}_1 + a_1 \ddot{\theta}) + m\beta_1 q_1 \dot{\theta}^2 + \tfrac{1}{2} EI\, \gamma_1 q_1 = 0 \qquad \text{(A.2-2)}$$

$$m(\beta_2 \ddot{q}_2 + \alpha_2 \ddot{\theta}) + m\beta_2 q_2 \dot{\theta}^2 + \tfrac{1}{2} EI\, \gamma_2 q_2 = 0 \qquad \text{(A.2-3)}$$

$$m(\beta_3 \ddot{q}_3 + \alpha_3 \ddot{\theta}) + m\beta_3 q_3 \dot{\theta}^2 + \tfrac{1}{2} EI \gamma_3 q_3 = 0 \qquad \text{(A.2-4)}$$

The variables β_i , α_i and γ_i result from substitution of the Ritz Approximation Eq. 2.1 into the potential and kinetic energy equations 2.6 and 2.7. They are defined as

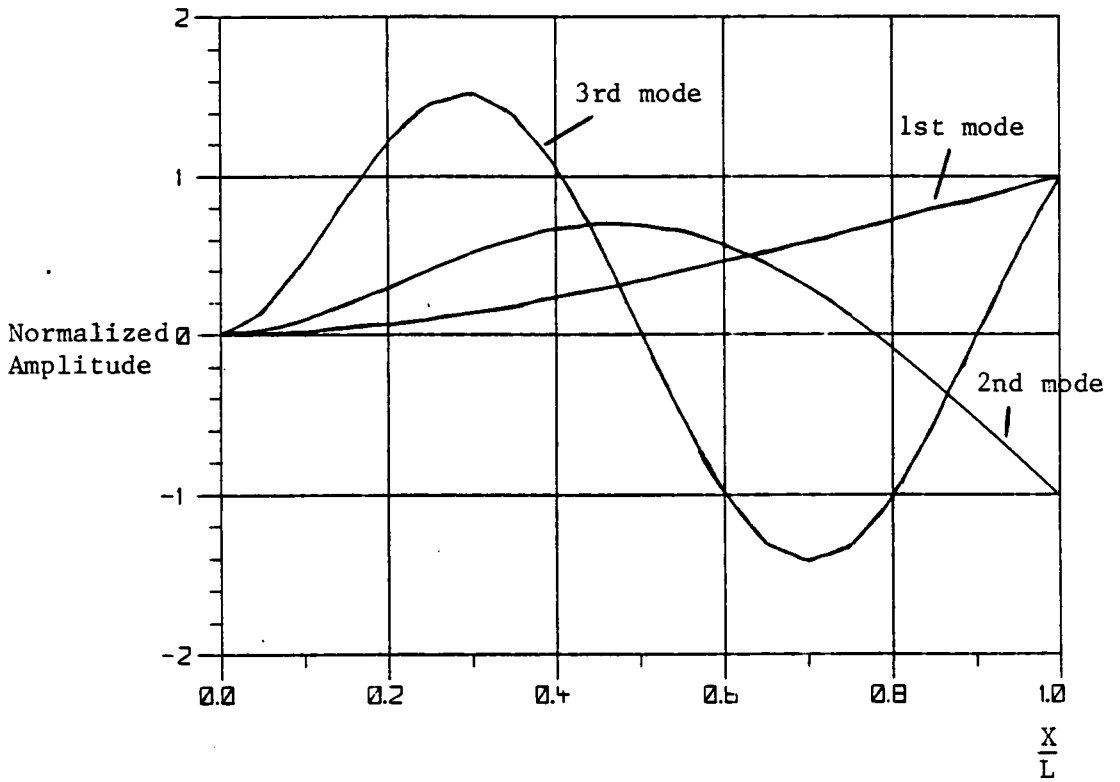

Fig. A.2 1st Three Mode Shapes of Cantilevered Beam in Bending

$$\beta_i = \int_0^L \phi_i^2 \, dx \tag{A.2-5}$$

$$\alpha_i = \int_0^L x \, \phi_i \, dx \tag{A.2-6}$$

$$\gamma_i = \int_0^L (\phi_i'')^2 \, dx \tag{A.2-7}$$

These integrals were evaluated for the chosen mode shapes with the help of the symbolic manipulation language MACSYMA as

$$\beta_1 = 1.855\ell \quad , \quad \beta_2 = 0.964\ell \quad , \quad \beta_3 = 1.0016\ell$$

$$\alpha_1 = -0.77\ell^2 \quad , \quad \alpha_2 = -0.089\ell^2 \quad , \quad \alpha_3 = -0.0325\ell^2$$

$$\gamma_1 = I\frac{22.936}{\ell^3} \quad , \quad \gamma_2 = I\frac{468.04}{\ell^3} \quad , \quad \alpha_3 = I\frac{3812.8}{\ell^3}$$

Equations A.3-1 thru A.3-4 are linearized by assuming only small perturbations exist (hopefully achieved through the control algorithm...) about the equilibrium points

$$q_i = \dot{q}_i = 0 \tag{A.2-8}$$

Thus making all higher order terms involving these variables negligible. The resulting coupled linear equations are

$$m\left(\frac{\ell^3}{3}\ddot{\theta} + \alpha_1\ddot{q}_1 + \alpha_2\ddot{q}_2 + \alpha_3\ddot{q}_3\right) = T_a(t) \qquad \text{(A.2-9)}$$

$$m(\beta_1\ddot{q}_1 + \alpha_1\ddot{\theta}) + \tfrac{1}{2}EI\,\gamma_1 q_1 = 0 \qquad \text{(A.2-10)}$$

$$m(\beta_2\ddot{q}_2 + \alpha_2\ddot{\theta}) + \tfrac{1}{2}EI\,\gamma_2 q_2 = 0 \qquad \text{(A.2-11)}$$

$$m(\beta_3\ddot{q}_3) + \alpha_3\ddot{\theta}) + \tfrac{1}{2}EI\,\gamma_3 q_3 = 0 \qquad \text{(A.2-12)}$$

Eq. A.3-6) through A.3-9) can be condensed into the matrix representation

$$\underline{M}\,\ddot{\underline{q}} + \underline{C}\,\dot{\underline{q}} + \underline{K}\,\underline{q} = \underline{B}\,T_a \qquad \text{(A.2-13)}$$

where

$$q = \begin{bmatrix} \theta \\ q_1 \\ q_2 \\ q_3 \end{bmatrix}$$

$$\underline{M} = \begin{bmatrix} \frac{m\ell^3}{3} & m\alpha_1 & m\alpha_2 & m\alpha_3 \\ m\alpha_1 & m\beta_1 & 0 & 0 \\ m\alpha_2 & 0 & m\beta_2 & 0 \\ m\alpha_3 & 0 & 0 & m\beta_3 \end{bmatrix}$$

$$\underline{K} = \begin{bmatrix} 0 & 0 & 0 & 0 \\ 0 & \frac{1}{2} EI\gamma_1 & 0 & 0 \\ 0 & 0 & \frac{1}{2} EI\gamma_2 & 0 \\ 0 & 0 & 0 & \frac{1}{2} EI\gamma_3 \end{bmatrix}$$

$$\underline{C} = \begin{bmatrix} C_1 & 0 & 0 & 0 \\ 0 & 0 & 0 & 0 \\ 0 & 0 & 0 & 0 \\ 0 & 0 & 0 & 0 \end{bmatrix}$$

and

$$B = \begin{bmatrix} B_1 \\ 0 \\ 0 \\ 0 \end{bmatrix} .$$

APPENDIX B

SYSTEM DAMPING CALCULATIONS

B.1 Beam Damping

The clamped-free response to an initial first mode deflection is shown for ST2 in Fig. B.1. The ratio of successive amplitudes of oscillation is

$$\frac{A_0}{A_1} = 1.066 \tag{B.1-1}$$

The damping ratio in the beam's response is determined from the logarithmic decrement equation (25):

$$\xi = \frac{\ell_n \frac{A_0}{A_1}}{\sqrt{4\pi^2 + \left(\ell_n \frac{A_0}{A_1}\right)^2}} \tag{B.1-2}$$

This was calculated to be

$$\xi = 0.0103 \tag{B.1-3}$$

Using equivalent mass and stiffness terms in Eq. 3.1 for the first mode

$$\begin{aligned} m_1 &= 0.0057 \ \frac{\text{lb} \cdot \text{sec}^2}{\text{in}} \\ k_1 &= 0.0640 \ \text{lb/in} \end{aligned} \tag{B.1-4}$$

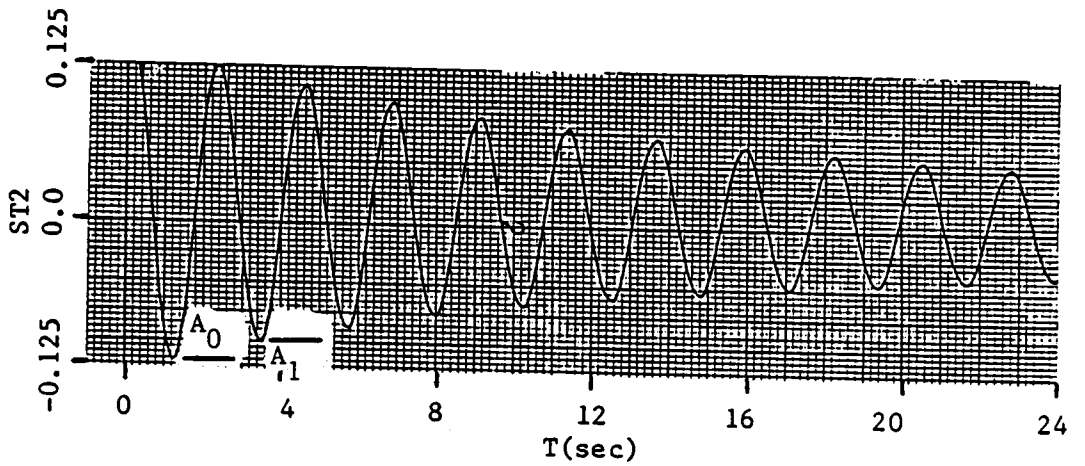

Fig. B.1 Cantilevered Beam's Response to First Mode Deflection

An approximate equivalent damping term can be calculated from

$$D_{eq} = 2\xi\sqrt{KM} \qquad \text{(B.1-5)}$$

The was calculated to be

$$D_{eq} = 0.00039 \frac{lb \cdot sec}{in} \qquad \text{(B.1-6)}$$

This is the equivalent damping in the first mode of vibration, the damping in the second and third modes are simply approximated with the relationship of Eq. 6.1, $D_{eq} \alpha \frac{1}{w}$. When these values were tested in simulations, the responses were not damping out fast enough compared to the experimental data. These values of damping were usually iterated upon until the best matchup was obtained. The final values were

$$D_{eq} = 0.0005 \frac{lb \cdot sec}{in}$$

$$D_{q2} = 0.00008 \frac{lb \cdot sec}{in}$$

$$D_{q3} = 0.00003 \frac{lb \cdot sec}{in}$$

The simulation results for the system with these damping values are shown in Chapter 6 in Fig. 6.2 and 6.3.

B.2 Beam/Motor System Damping

Calculations are similar here to Appendix B.1. The complete beam/motor system is given an initial angular displacement. By implementing a feedback law of position control above, the beam will oscillate about its equilibrium. This response is shown in Fig. B.2. The ratio of successive amplitudes is

$$\frac{A_0}{A_1} = 2.154 \qquad \text{(B.2-1)}$$

which from Eq. B.1-2 gives a damping ratio of

$$\xi = 0.113 \qquad \text{(B.2-2)}$$

For this system, approximate damping is given by

$$D_{eq} = 2\xi \sqrt{KJ} \qquad \text{(B.2-3)}$$

The equivalent stiffness of this system is given by

$$K_{eq} = G_{th}\, G_{pot}\, G_A\, K_T \qquad \text{(B.2-4)}$$

where G_{th} = gain on angular position feedback

G_{pot} = gain of angular position potentiometer

G_A = amplifier gain (amps/volt)

K_T = torque constant of motor

The values of K and I are

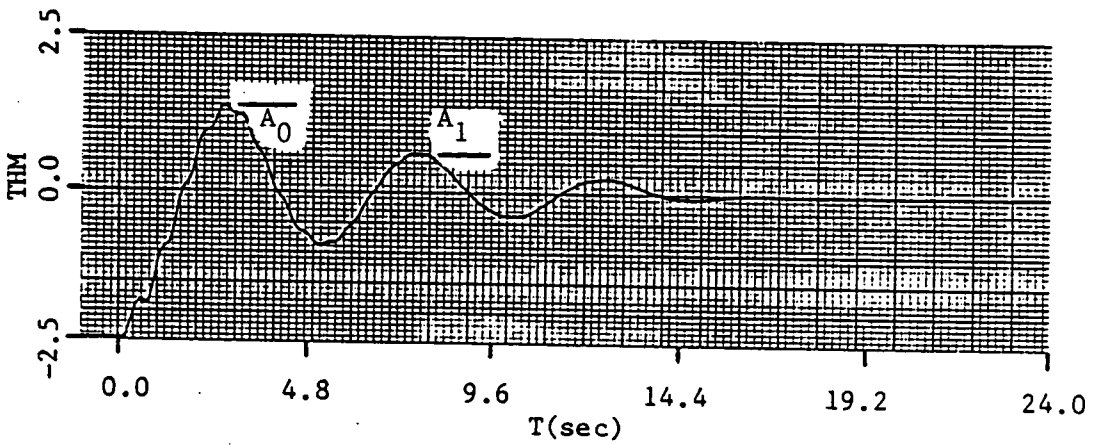

Fig. B.2 Angular Response of Beam/Motor System with Position Feedback to an Initial 45° Displacement.

$$J = 2.027 \text{ lb}\cdot\text{in}\cdot\text{sec}^2$$
$$K = 4.369 \text{ lb/in} \qquad \text{(B.2-5)}$$

From this

$$D_{th} = 0.72 \text{ lb}\cdot\text{in}\cdot\text{sec} \qquad \text{(B.2-6)}$$

When this approximate angular damping term is included in the model, good, improved simulations are achieved. This is demonstrated in Ch. 6 with Fig. 6.4 through Fig. 6.11.

The vita has been removed from the scanned document

Theoretical and Experimental Study into the Dynamics and Control of a Flexible Beam with a DC-Servo Motor Actuator

by

John M. Juston

ABSTRACT

Position and vibration control of a flexible beam is studied analytically and in the laboratory. Two different motor types are compared as actuators throughout the thesis: a standard voltage controlled motor and a torque controlled motor. The experimental beam is controlled with a dc-servo motor at its base and is instrumented with strain gages and a potentiometer. The control law is a form of linear, direct-output feedback. State estimators augment the control law to provide rate information that is not available from the instrumentation. Accurate modeling of the system's inherent damping characteristics is achieved by analyzing experimental data. Gains were iterated yielding minimum-gain norm and minimum-sensitivity norm solutions to meet imposed eigenvalue placement constraints. Results for the two solutions and the two systems are compared and contrasted. Experimental verification of analytical results is hampered by unmodelled system non-linearities. Several attempts at bypassing these obstacles are shown. Finally, conclusions and recommendations are made.